July 2019

ASYMPTOTIC AND NUMERICAL ANALYSIS OF COHERENT STRUCTURES IN NONLINEAR SCHRODINGER-TYPE EQUATIONS

Cory Ward

ASYMPTOTIC AND NUMERICAL ANALYSIS OF COHERENT STRUCTURES IN NONLINEAR SCHRÖDINGER-TYPE EQUATIONS

A Dissertation Presented

by

CORY WARD

Submitted to the Graduate School of the
University of Massachusetts Amherst in partial fulfillment
of the requirements for the degree of

DOCTOR OF PHILOSOPHY

May 2019

Department of Mathematics and Statistics

ASYMPTOTIC AND NUMERICAL ANALYSIS OF COHERENT STRUCTURES IN NONLINEAR SCHRÖDINGER-TYPE EQUATIONS

A Dissertation Presented

by

CORY WARD

Approved as to style and content by:

Panos G. Kevrekidis, Chair

Nathaniel Whitaker, Member

Hans Johnston, Member

Dimitris Maroudas, Member

Nathaniel Whitaker, Department Head
Department of Mathematics and Statistics

ACKNOWLEDGMENTS

First and foremost, I would like to thank my advisors Nate Whitaker and Panos Kevrekidis for their abundance of patience and support throughout the last few years – as teachers you've been insightful, as collaborators you've been generous, and as people you've been great friends. Thanks so much for helping me along the way!

I would also like to thank Hans Johnston for many discussions over the years about not only math but life too – thanks for the advice!

Let me also thank my collaborators, Yannis Mylonas, Lijuan Guo, Dimitri Frantzeskakis, Vassilis Rothos, and Yannis Kevrekidis, for which this thesis could never have been written without. Many thanks to Dimitrios Maroudas for bravely agreeing to be apart of my committee before this thesis was written.

A special thanks to Ilona Trousdale and Jake Lagerstrom for always answering my questions even when it wasn't their job. I would also like to thank the math department, and UMass generally, for fostering such a wonderful environment to learn in.

Many thanks to my wonderful family Mandy, Luke, Kerry, Janelle, and Cinda for always supporting me in whatever I did.

My gratitude also goes out to Terry Jones for many insightful math discussions over the years.

And finally I'd like to thank my loving wife Brittany who has been a constant source of affection and understanding – without a doubt, you are the best thing in my life.

ABSTRACT

ASYMPTOTIC AND NUMERICAL ANALYSIS OF COHERENT STRUCTURES IN NONLINEAR SCHRÖDINGER-TYPE EQUATIONS

MAY 2019

CORY WARD

B.Sc., TEXAS A& M UNIVERSITY COMMERCE

M.Sc., UNIVERSITY OF MASSACHUSETTS AMHERST

Ph.D., UNIVERSITY OF MASSACHUSETTS AMHERST

Directed by: Professor Panos G. Kevrekidis and Professor Nathaniel Whitaker

This dissertation concerns itself with coherent structures found in nonlinear Schrödinger-type equations and can be roughly split into three parts.

In the first part we study a deformation of the defocusing nonlinear Schrodinger (NLS) equation, the defocusing Camassa-Holm NLS (CH-NLS) equation in both one and two space dimensions. We use asymptotic multiscale expansion methods to reduce this model to a Boussinesq-like equation, which is then subsequently used to obtain approximate solitary wave solutions for both the 1D and 2D CH-NLS equations. We then use direct numerical simulations to investigate the validity of these approximate solutions, their evolution, and their head-on collisions. Using a similar methodology, we also explore a deformation of the derivative nonlinear Schrodinger (DNLS) equation, the Camassa-Holm DNLS (CH-DNLS) equation, in one space dimension.

The second part of this thesis involves the construction of numerical methods for identifying steady states of nonlinear wave equations as fixed points. We first introduce two modifications of the so-called accelerated imaginary-time evolution method (AITEM). In our first modification, time integration of the underlying gradient flow is done using exponential time differencing instead of using more standard methods. In the second modification, we present a generalization of the gradient flow model, motivated by the work of Nesterov. Finally, we apply these techniques to the so-called Squared Operator Method, enabling convergence to excited states.

The third part consists of the construction of both numerical and analytical methods for finding rogue waves in nonlinear Scrödinger-type equations. First, by identifying rogue wave solutions as fixed points in space-time, we modify a spectrally accurate Newton conjugate gradient method to obtain such solutions for not only the NLS equation but also for equations with a different nonlinearity. We propose a methodology for obtaining rogue wave solutions analytically by considering them as self-similar solutions on a background. Using a number of known equations as case examples, we successfully recover several rogue wave solutions analytically, making this one of the few methods which does not invoke integrability directly.

TABLE OF CONTENTS

Page

ACKNOWLEDGMENTS . . . . . **iv**

ABSTRACT . . . . . **v**

LIST OF FIGURES . . . . . **x**

CHAPTER

1. INTRODUCTION **1**

1.1 Deformations of Nonlinear Schrödinger-Type Equations 1
1.2 A Toolkit For Steady States of Nonlinear Wave Equations: Continuous Time Nesterov and Exponential Time Differencing Schemes 4
1.3 Evaluating the Robustness of Rogue Waves Under Perturbations 6
1.4 Rogue Waves as Self-Similar Solutions on a Background: A Direct Calculation 8

2. THE CAMASSA-HOLM NONLINEAR SCHRÖDINGER EQUATION IN ONE SPACE DIMENSION **9**

2.1 Model and continuous-wave solution 9
2.2 Asymptotic expansions and solitons 11

2.2.1 The Boussinesq equation 11
2.2.2 The KdV equation 12
2.2.3 Dark and antidark solitons of the CH-NLS equation 14

2.3 Numerical Exploration 15

2.3.1 Numerical methods 16
2.3.2 Results of direct simulations 17

3. THE CAMASSA-HOLM NONLINEAR SCHRÖDINGER EQUATION IN TWO SPACE DIMENSIONS **24**

3.1 Model and its analytical consideration 24

3.1.1 Presentation of the model and some of its properties 24
3.1.2 Multiscale expansions and reduced models 26

3.2 Asymptotic Solutions and Numerical Exploration 30

3.2.1 Line Solitons 30
3.2.2 Lump solitons 34

4. THE CAMASSA-HOLM DERIVATIVE NONLINEAR SCHRÖDINGER EQUATION 41

4.1 Model and Its stability 41
4.2 Reductive derivation of MKdV equation from CH-DNLS equation 42
4.3 Reductive Derivation of KdV Equation from CH-DNLS Equation 45
4.4 Numerically Obtained Solutions 47

5. A TOOLKIT FOR STEADY STATES OF NONLINEAR WAVE EQUATIONS: CONTINUOUS TIME NESTEROV AND EXPONENTIAL TIME DIFFERENCING SCHEMES 53

5.1 Earlier Methods for Calculating Ground States 53

5.1.1 AITEM 53
5.1.2 Spectral Renormalization 55

5.2 Proposed Twists 56

5.2.1 Exponential Time Differencing 57
5.2.2 Continuous Time Nesterov 58
5.2.3 Accelerated Continuous Time Nesterov 60

5.3 Computational Results 62

5.3.1 Ground States in 1D 62
5.3.2 Ground States in 2D 65
5.3.3 Excited States in 1D 66
5.3.4 Excited States in 2D 71

5.4 Implementation Details 75

5.4.1 Renormalized Methods 75
5.4.2 Matlab Code 76

6. EVALUATING THE ROBUSTNESS OF ROGUE WAVES UNDER PERTURBATIONS 78

6.1 Benchmarks & Results 78
6.2 Implementation Details 85

6.2.1 Methods 85
6.2.2 Newton-CG code for the NLS Peregrine Soliton 87

7. ROGUE WAVES AS SELF-SIMILAR SOLUTIONS ON A BACKGROUND: A DIRECT CALCULATION 89

7.1 Self-Similar Calculation for the NLS case 89
7.2 Going Beyond NLS: Other Models 93

7.2.1 Hirota Equation 93
7.2.2 Davey-Stewartson I 93
7.2.3 Zakharov Equation 94

8. CONCLUSIONS 96

8.1 The Camassa-Holm Nonlinear Schrödinger Equation in One Space Dimension 96
8.2 The Camassa-Holm Nonlinear Schrödinger Equation in Two Space Dimensions 97
8.3 The Camassa-Holm Derivative Nonlinear Schrödinger Equation 98
8.4 A Toolkit For Steady States of Nonlinear Wave Equations: Continuous Time Nesterov and Exponential Time Differencing Schemes 99
8.5 Evaluating the Robustness of Rogue Waves Under Perturbations 101
8.6 Rogue Waves as Self-Similar Solutions on a Background: A Direct Calculation 102

BIBLIOGRAPHY 104

LIST OF FIGURES

Figure **Page**

2.1 (a) Log-log plot of the L^2 error between the predicted solution (2.24) and the numerical solution as a function of ϵ. All other parameter values fixed at $u_0 = 1$, $a = 0.5$, $\beta = 0.1$; in this case, parameter $p = 1$, i.e., $p \in (1/2, 2)$, which means that the soliton is antidark (cf. text). (b) Contour plot showing the evolution of the density of the corresponding antidark soliton, for $\epsilon = 0.04$. (c) Same as (b) but for the difference between the densities of the analytical and the numerical solution. It can be observed that the error becomes larger as time increases; this is especially so at the "wings" (rather than the core) of the soliton. 18

2.2 (a) Same as Fig. 2.1(a), but for a dark soliton, for $u_0 = 1$, $a = 0.8$, $\beta = 0.1$, $\epsilon = 0.04$; note that, here, $p = 2.56 > 2$ and thus the soliton is indeed of the dark type (cf. text). (b) Same as Fig. 2.1(b), but for the dark soliton of panel (a). Again, the error becomes larger as time increases, especially at the "wings" of the soliton. 20

2.3 Panels (a) and (b) are the corresponding large ϵ results of Figs. 2.1(a) and 2.2(a), respectively. Parameter values are the same as in Figs. 2.1(a) and 2.2(a) except that $\epsilon = 1$. 20

2.4 Collisions of various dark and anti-dark solitons shown via contour plots of there respective amplitudes. The intial condition used for each was Eq. (2.31) with the given parameter values – except (e) in which a gallilean boost was applied. 21

3.1 Top panels: Contour plots showing the evolution of the density of one line dark soliton of relatively large amplitude, with $\epsilon = 0.1$, at $t = 0$ [panel (a)] and $t = 100$ [panel (b)]. It is observed that the soliton splits into two waves, a dark and an anti-dark, and also emits radiation. Bottom panels: Collision between two line dark solitons. Panel (c) shows the initial condition, at $t = 0$, and panel (d) shows the outcome of the head-on collision, at $t = 100$. Here, the leftmost soliton appears as the rightmost one, and vice versa. Parameter values: $a = 1$, $\gamma = 1.3$, and $\beta = 1$. 32

3.2 Relative elasticity of dark line soliton collisions. The dashed lines represent the maximum and minimum values of the amplitude (vertical axis), for each value of epsilon shown (horizontal axis), that occurs for the evolution of a single dark line soliton (as in Fig. 3.1(a),(b)). The solid lines represent the maximum and minimum amplitude, for each value of epsilon, that occur for the collision of two dark line solitons (as in Fig. 3.1(c),(d)). Note that although a collision takes places, the relative amplitudes of the line solitons is very similar to that as if the collision never took place; stated differently, the two line solitons interact very weakly despite the large amplitudes. Note that the value of the amplitude given in the plot was taken at $t = 100$ with the same parameter values as in Fig. 3.1. 33

3.3 Top panels: Contour plots showing the evolution of the density of one anti-dark lump soliton of relatively small amplitude, with $\epsilon = 0.01$, at $t = 0$ [panel (a)] and $t = 100$ [panel (b)]. It is observed that the lump evolves undistorted and no emission of radiation is observed. Parameter values: $a = \frac{1}{2}$, $\gamma = 1$, $\beta = 0.8$. Bottom panels: Collision between two dark lumps. Panel (c) shows the initial condition, at $t = 0$, and panel (d) shows the outcome of the head-on collision, at $t = 100$. Here, the leftmost lump appears as the rightmost one, and vice versa; again, the radiation is barely discernible at $t = 100$. Parameter values: $a = \frac{1}{2}$, $\epsilon = 0.005$, $\gamma = 1$, $\beta = 0.85$. 34

3.4 Large-amplitude anti-dark lump solitons. Top panels show the evolution of this waveform for $a = \frac{1}{2}$, $\epsilon = 0.01$, $\gamma = 1$, and $\beta = 3$; it is observed that this structure evolves into a bent shape. Bottom panels depict the collision between two identical anti-dark lumps, for $a = 0.6$, $\epsilon = 0.08$, $\gamma = 0$, and $\beta = \frac{1}{2}$; the collision appears to be almost elastic although radiation develops in each lump after it. 37

3.5 Similar to Fig. 3.4, but for large-amplitude dark lump solitons. The observed behavior is similar to that of the anti-dark lump case. For the top panels, the parameter values are $a = 1$, $\epsilon = 0.01$, $\gamma = 1$, and $\beta = 1.8$, while for the bottom panels $a = 1$, $\epsilon = 0.08$, $\gamma = 0$, and $\beta = \frac{1}{2}$. 38

3.6 Top panels: collision between large-amplitude dark line and lump solitons; parameters used: $a = 1$, $\epsilon = 0.08$, $\gamma_{\text{Line}} = 1.5$, $\beta_{\text{Line}} = 1$, $\gamma_{\text{Lump}} = 0$, and $\beta_{\text{Lump}} = \frac{1}{2}$. Bottom panels: collisions between large-amplitude anti-dark line and lump solitons; parameters used: $a = 0.6$, $\epsilon = 0.08$, $\gamma_{\text{Line}} = 1.5$, $\beta_{\text{Line}} = 1$, $\gamma_{\text{Lump}} = 0$, and $\beta_{\text{Lump}} = \frac{1}{2}$. 38

3.7 Evolution of Gaussian-like pulses; the top panels depict the case of an extremely elongated (in the y-direction) such pulse, the middle panels show the case of a slightly elongated Gaussian, while the bottom panels depict the evolution of a completely symmetric such pulse. For detailed initial condition parameters, see the text. 40

4.1 Small Amplitude Solitons. Note that the speed of the KdV and MKdV solitons are nearly identitical to what the asympototic expansion predicts. Parameter values used: (a) $\epsilon = 0.005$, $a = 0.5$, $b = -1$, $q_0 = 1$ (b) $\epsilon = 0.005$, $a = 0.5$, $b = 1$, $q_0 = 1$ (c) $\epsilon = 0.01$, $a = 0.5$, $\lambda = 1$, $q_0 = 1$ (d) $\epsilon = 0.01$, $a = 0.5$, $\lambda = 1$, $q_0 = 0.5$. 48

4.2 Large Amplitude Solitons. We see a similar qualitative behavior as in the small amplitude case, except now with some small radiation (as the solution initially "adapts"). Parameter values used: (a) $\epsilon = 0.02$, $a = 1$, $b = -1$, $q_0 = 1$ (b) $\epsilon = 0.02$, $a = 1$, $b = 1$, $q_0 = 1$ (c) $\epsilon = 0.5$, $a = 0.5$, $\lambda = 1$, $q_0 = 1$ (d) $\epsilon = 0.2$, $a = 0.5$, $\lambda = 1$, $q_0 = 0.5$. 49

4.3 Large Amplitude Collisions. (a) $\epsilon_{\text{KdV}} = 0.1$, $\lambda = 1$, $\epsilon_{\text{MKdV}} = 0.07$, $b = -1$, $a = 1$, $q_0 = 1$ (b) $\epsilon_{\text{KdV}} = 0.03$, $\lambda = 1$, $\epsilon_{\text{MKdV}} = 0.07$, $b = 1$, $a = 1$, $q_0 = 1$. We can see that the antidark KdV-antidark MKdV, as well as the antidark KdV-dark MKdV collisions are nearly elastic for the considered parameters and initial conditions. 51

5.1 Evolution of the error, defined as the L^2 norm of the difference between successive iterates, as a function of the iteration index for different potentials $V(x)$, when seeking the ground state of the 1D NLS equation. The right set of tables indicates the values of the parameters selected and the corresponding number of iterations needed to reach the prescribed tolerance of 10^{-10}. 64

5.2 Similar to Fig. 5.1, but now for a double well potential. Only the ETDV is able to converge to the asymmetric ground state of this potential. 66

5.3 Corresponding steady states of the potentials analyzed in the previous two figures. Notice the $x \neq 0$ centering of cases (d) and (g). 67

5.4 Two prototypical case examples in 2D. The top set of panels (a)-(c) displays the evolution of the error over the number of iterations, the parameters (and convergence iteration number) of the different methods, and the profile of the resulting solution for a parabolic trap in a defocusing 2D NLS with a Gaussian initial guess. Panels (d)-(f) report in similar format but now for a focusing 2D NLS with a periodic potential. 69

5.5 Left panel: The bifurcation diagram of the first five excited states of the defocusing 1D NLS with parabolic trap. Right panel: Number of iterations needed to go from each point on the relevant branch to the next. 71

5.6 Panel (a) illustrates the different branches identified in the two-dimensional bifurcation diagram of the elliptic NLS problem with the parabolic trap. The bottom panel shows the number of iterations needed for the ASCTN scheme to converge from one solution (member of a branch) to the next (member of the branch). 72

5.7 Typical examples of the different branches of solutions, not only the ground state one (Br1), but also excited ones such as the planar dark soliton (Br2), the single charge vortex (Br3) and so on that one can converge to using the SCTN method. 74

6.1 Comparison of the Peregrine soliton (a) with the numerical solution (c). Time slice at $t = 0$ of the exact solution (b) and numerical solution (d). Excellent agreement is seen between the two solutions. 79

6.2 Comparison of an exact cnoidal rogue wave in (a) with the numerical solution (c). Slice at $t = 0$ of the exact solution (b) and numerical solution (d). Again, we see very good agreement between the two solutions. 80

6.3 (a) Contour plot of the Peregrine soliton. (b) Corresponding solution obtained numerically. (c) Contour plot of the perturbative solution Eq. (6.2), while (d) is the corresponding numerical solution. Although it is weak, there is a discernible asymmetry in panels (c) and (d) (as compared with (a) and (b)) caused by the TOD term. Here we have set $\epsilon = 0.02$. We have also included the vertical red bar in (c) and (d) so as to highlight the slight rotation (in comparison to the $\epsilon = 0$ case where the peak and dips of the PS are are aligned). 81

6.4 Family of solutions with $\epsilon = 0$ for different values of p around the integrable limit of $p = 1$. The profiles confirm the persistence of the rogue wave. 82

6.5 Direct numerical simulation results confirming that evolution through the ETDRK4 method yields excellent agreement with the Newton-CG findings. The error is measured via the L^∞ norm (in space) of the difference at each point in time between the time-evolved (ETDRK4) and the Newton-CG solution. Here $\epsilon = 0$. 83

6.6 Same as Fig. 6.4 but now for the family of rogue waves on top of the cnoidal background with $\epsilon = 0$. 84

6.7 Persistence of rogue waves for both $p \neq 1$ and $\epsilon \neq 0$ through the family of solutions with $\epsilon = 0.02$. 86

8.1 Schematic showing the relationships of the various methods appearing in Chapter 5. Here FD denotes the finite difference discretization of time used to obtain the specific schemes AITEM and ACTN. Finally, the question mark represents a possible (not obtained here) scheme in which the time discretization of CTN is done via exponential time-differencing methods. 99

CHAPTER 1

INTRODUCTION

1.1 Deformations of Nonlinear Schrödinger-Type Equations

The Camassa-Holm (CH) equation [1] is a completely integrable nonlinear dispersive partial differential equation (PDE), which has attracted much interest due to its soliton solutions, its applications to shallow water waves [2, 3], and its interesting mathematical features, such as the long-time asymptotics [4], and inverse scattering [5]. It is worthwhile to note that the applications of the model are not exhausted in the theme of water waves, but rather have been extended and useful to areas such as acoustic scattering [6], as well as axial deformation waves arising in hyperelastic rods [7, 8], among others.

On the other hand, the nonlinear Schrödinger (NLS) equation [9–13] is a principal completely integrable nonlinear dispersive PDE, which has played a fundamental role in shaping our understanding in a diverse array of systems. These range from atomic physics [14,15] and nonlinear optics [11,16,17], to plasmas [18], deep water waves [11,19], and rogue waves [20].

In a similar direction, the derivative NLS (DNLS) equation has also attracted considerable attention both from a theoretical point of view and with respect to physical applications. In plasma physics it has long been known that the DNLS equation governs the evolution of small but finite amplitude Alfvén waves propagating quasi-parallel to the magnetic field [21, 22]. This equation is also used to describe large-amplitude magnetohydrodynamic (MHD) waves in plasmas [23]. Under special conditions, bright solitons, dark solitons, anti-dark solitons, breather solutions, as well as rogue waves have been obtained in Refs. [24, 25].

In an intriguing recent development, the work of [26] proposed a novel deformation of the NLS, as a member of a series of deformations of integrable equations. The corresponding deformation of the famous Korteweg-de Vries (KdV) equation produced the CH equation, hence it is of particular interest to study the relevant deformation of the NLS equation, i.e., the CH-NLS equation. In Ref. [27] the focusing CH-NLS system was studied both analytically and numerically, and its bright soliton solutions and their dynamics and interactions were explored; note, however, that in [27] no definitive conclusion about the complete integrability of the CH-NLS equation was reported. Likewise, in [28] the authors deformed the DNLS equation, using similar techniques to [26], obtaining the so-called CH-DNLS equation. Here, however, even less is known than with the CH-NLS.

In Chapters 2 and 3 we explore the defocusing variant of the CH-NLS equation and study its dark soliton solutions. Given the lack of information regarding the integrability of this model or the existence of exact analytical dark soliton solutions, we resort to asymptotic multiscale expansion techniques [29]. Such techniques have been used to demonstrate that several completely integrable systems can be reduced to other integrable models [30]. Importantly, these techniques have also been extended to the case of nonintegrable systems: in such cases, solutions of the reduced models can be used to construct approximate solutions of the original models. For instance, variants of the defocusing NLS equation have been reduced to the KdV equation, allowing a description of shallow dark solitons in terms of KdV solitons (see, e.g., the reviews [31,32] and references therein). This approach also allowed for the prediction of the existence of a structure known as *antidark soliton*, namely a dark soliton with reverse-sign amplitude, having the form of a hump (instead of a dip) on top of the continuous-wave (cw) background density [33–37]. Note that relevant studies employing multiscale expansion methods and predicting the occurrence of antidark solitons were recently extended to settings involving nonlocal nonlinearities [38–40].

A brief description of our findings, as well as the outline of the presentation, is as follows. In Chapter 2, we consider the $(1+1)$-dimensional defocusing CH-NLS equation.

More specifically, in Section 2.1, we present the model and briefly revisit its modulational stability analysis [27]. In Section 2.2, we use multiscale expansion methods to derive asymptotic reductions of the 1D defocusing CH-NLS equation. At an intermediate stage of the asymptotic analysis, we obtain a Boussinesq-type equation; next, we consider the far-field of the Boussinesq equation, and derive two KdV equations for right- and left-going waves. We then employ the KdV soliton to construct approximate soliton solutions of the original CH-NLS equation; we show that these soliton solutions are either of the dark or of the antidark type, depending on the sign of a characteristic parameter. In Section 2.3, we present the results of our numerical computations. We calculate the error between the asymptotic solutions and the numerical solutions, and then we focus on the numerical study of the dynamics and head-on collisions of the dark and antidark solitons. We find that such collisions are quasi-elastic for solitons of sufficiently small amplitude. We also show that collisions between different soliton types, i.e., between dark and antidark solitons, are also possible and discuss the special conditions under which these can be realized.

Chapter 3 is devoted to the $(2+1)$-dimensional defocusing CH-NLS equation. Here, we will adopt multiscale expansion methods to reduce the model to a KP equation; this allows us to construct approximate soliton solutions, having the form of line solitons or lumps, being of the dark or anti-dark type. In Section 3.1, we present the model, and study both the linear and the nonlinear regime. We present results of multiscale expansion methods that are used for the derivation of asymptotic reductions of the CH-NLS equation. In particular, at an intermediate stage of the asymptotic analysis, we obtain a 2D Boussinesq-type equation, and also obtain its far-field, namely a pair of KP equations (that are either of the KP-I or KP-II type) for right- and left-going waves. In Section 3.2, we use solutions of the KP-I and KP-II models to construct approximate soliton solutions of the original CH-NLS equation; the derived solutions have the form of dark or anti-dark line solitons and lumps. We also present results of direct numerical simulations concerning the dynamics and interactions between the various approximate soliton solutions.

Finally, Chapter 4 is devoted to the $(1+1)$-dimensional CH-DNLS equation. Here, we employ asymptotic multiscale expansion techniques to derive the modified KdV (MKdV) and KdV equations from the CH-DNLS equation. This allows us to construct approximate solutions of this model in the form of dark and anti-dark solitons. In Section 4.1, we present the model and examine the modulational stability of its homogeneous equilibria. In Sections 4.2 and 4.3, we use two different types of multiscale expansion methods in order to derive MKdV and KdV equations, respectively. We then use their explicit solutions to construct two types of approximate soliton solutions of the original CH-DNLS equation, namely dark and anti-dark solitons. In Section 4.4, direct numerical simulations illustrate the validity of the approximate solutions and demonstrate their dynamical evolution as well as their nearly elastic collisions for the perturbatively constructed small amplitude solutions considered.

1.2 A Toolkit For Steady States of Nonlinear Wave Equations: Continuous Time Nesterov and Exponential Time Differencing Schemes

In models stemming from nonlinear optics and atomic physics, it is customary to seek a Hamiltonian description of the dynamics, e.g., for the envelope of optical pulses or for the wavefunction of quantum systems that follows a Schrödinger type partial differential equation. If, in addition, nonlinear effects are contributing, e.g., either because of the so-called Kerr effect in optics [16, 17] or because of the mean-field interaction of bosonic atoms [14, 15, 41–43], then the prototypical model becomes the nonlinear Schrödinger (NLS) equation. The NLS [9, 10, 12, 13, 44] is a dispersive nonlinear partial differential equation (PDE) that has been essential in understanding some of the most groundbreaking results in the physics of such systems. Additional areas of application include, but are not limited to Langmuir waves in plasmas [45,46], deep water and freak/rogue waves, [20,47], as well as more broadly in fluid mechanics [18].

In its canonical form, the equation reads:

$$i\partial_t u = -\tfrac{1}{2}\nabla^2 u + g|u|^2 u, \tag{1.1}$$

where u is the complex field and g is a constant. Physically, u may represent the envelope of the electric field in optics, the amplitude of water waves or the wavefunction of a Bose-Einstein condensate (BEC), and is the main object whose spatio-temporal evolution we are interested in probing. Very commonly in the above areas, we are interested in identifying standing wave solutions of Eq. (1.1) in the form: $u(x,t) = \psi(x)e^{-i\mu t}$ which, in turn, leads to the time-independent form of the equation:

$$\nabla^2\psi - V(x)\psi + \sigma|\psi|^2\psi + \mu\psi = 0. \tag{1.2}$$

The parameter μ is associated to the frequency of the solution and is referred to as the propagation constant in optics or the chemical potential in atomic BECs. This steady state problem constitutes a subject of wide exploration, to which a broad and diverse number of studies has been devoted. Both the ground and the excited states in this elliptic, nonlinear PDE problem are of interest. It should be noted that given the importance of the subject entire books have been dedicated to the analysis of associated numerical methods [48].

In Chapter 5, our aim is to add some useful twists to this extensive literature, based on recent computational developments in other areas (including the time stepping of ordinary and partial differential equations, and the development of schemes relevant for the iterative convergence of functional extremization). Our main contribution is to propose iterative schemes, based on the continuous time variant of Nesterov's method [49–51], for finding stationary states of Eq. (1.2). The structure of our presentation is as follows. We start by presenting in Section 5.1 some of the most popular methods that do *not* resort to the use of the Jacobian (i.e., Newton-type methods); the latter, and accelerated variants thereof, merit their own independent examination that is deferred to a future stage. Then, we present in Section 5.2 our proposed "twists" based on the above recent computational developments and their implementation in Eq. (1.2). In Section 5.3 we compare the results of the newly

proposed variants with the more standard methods. In Section 5.4 we discuss how to renormalize any numerical method in detail and present an example Matlab code illustrating the effectiveness of one of our methods.

1.3 Evaluating the Robustness of Rogue Waves Under Perturbations

Over the past decade there has been a tremendous explosion of interest towards the study of phenomena associated with extreme wave events, the so-called rogue or freak waves. This has largely been triggered by the experimental realization (and associated control) of such waveform manifestations in a diverse array of experiments that range from nonlinear optics [52–57] to hydrodynamics [58–60] and from plasmas [61] to superfluid helium [62] and to parametrically driven capillary waves [63]. The relevant advances have, by now, been discussed in numerous books on the subject [64–67] and have, in turn, triggered considerable progress towards the theoretical study of such waves, which are now contained to a large extent in a number of reviews [68–71].

Much of the relevant theoretical activity has revolved around the feature that in integrable models, such as the nonlinear Schrödinger (NLS) equation, the machinery of the inverse scattering transform (IST) can be utilized to obtain some prototypical waveforms that are natural candidates as rogue wave structures. Typical examples include the Peregrine soliton (PS) [72], the Kuznetsov [73], Ma [74] (KM) soliton, and the Akhmediev breather (AB) [75], among others (see also the work of Dysthe and Trulsen [76]). Among them, perhaps the most well-known entity is the Peregrine soliton which is algebraically localized in both space and time; the PS, KM and AB are essentially members of a parametric family of solutions where variation of a suitable parameter moves between a spatially periodic solution (AB), a localized one in both space and time (PS), and a periodic in time solution (KM).

However, a key lingering question is whether departure from integrability allows for the persistence of such rogue waves. To the best of our understanding the attempts to address

this issue have been quite limited. For instance, in a special case example the work of [77] illustrated that under some realistic perturbations (such as third order dispersion or self-steepening terms), a leading order perturbed variant of the PS would persist. Similarly, a perturbed inverse scattering approach has been used to consider the KM solution under dispersive and dissipative perturbations [78]. Other authors have attempted to argue on the basis of more general grounds [79], such as the proximity of these solutions to chaotic states, that they may persist. Nevertheless, it is clear that these approaches each have limitations.

It thus remains a rather open question whether rogue wave structures *persist* in the presence of "generic" perturbations and how their profile may be modified as a result of these perturbations. The unavailability of the integrable machinery of the IST which has been used for the vast majority of results on the subject [68–70] renders this question even more important; as an aside, we note here an effort to approach rogue waves from a self-similar perspective that does not require the IST toolbox [80]). It is also important to indicate that in most cases that we are familiar with the integrable models like the NLS are, at best, an idealized approximation of the true physical system. Hence, if these solutions are to be relevant in realistic settings, their persistence needs to be ensured. To address this question, numerical techniques appear to be well suited; they are not limited in any way by integrability considerations (on the contrary, they can use the integrable limit as a useful starting point towards exploring continuations to non-integrable variants). Furthermore, they can provide a result accurate to the prescribed numerical tolerance (and hence are not bound to "leading order" type considerations). However, there is a nontrivial obstacle; the most appropriate way to find localized solutions in these classes of models is via fixed point iterations [be they Newton-type schemes, spectral renormalization schemes, or imaginary time variants [48]]. Nevertheless, this class of methodologies cannot be applied here, as the solution is not stationary in time. Hence, if we are seeking a PS (a solution that "appears out of nowhere and disappears without a trace" [81]), the proper way to think of the solution

is as a localized one, a *two-dimensional homoclinic orbit* (i.e., asymptoting to the same stationary state), in space and time.

Thus, in Chapter 6, we propose to consider time as a *spatial variable* and develop an iterative scheme that identifies a localized solution in the $(x,t)-$plane. In Section 6.1 we present the details of the method along with examples (as well as benchmarks) of interest. In Section 6.2 we discuss the numerical method in detail and present an example Matlab code illustrating it effectiveness.

1.4 Rogue Waves as Self-Similar Solutions on a Background: A Direct Calculation

Here, we would like to take a different path in the vein of offering a different kind of theoretical (but possibly also computational) tool towards the identification of rogue wave structures. We are motivated by two facts: on the one hand, the availability of analytical techniques for finding rogue waves is largely limited to methods stemming from inverse scattering transform (IST) and integrable systems. As an aside, an interesting analytical method for identifying exact solutions, including rational ones, of the NLS can be found in [82, 83]; see [71] for a review involving also such solutions in other integrable models. Nevertheless, in many of the realistic non-integrable systems where such extreme waves appear the IST formulation is not available or applicable. Moreover, from a structural perspective, rogue waves are self-similar in their functional form, even though, contrary to what is the case for other such solutions [12], they do not blow up in finite time.

In light of these developments, in Chapter 7 we offer an unprecedented approach on the basis of self-similarity to capture such solutions. In Section 7.1 we present our new perspective on rogue waves by implementing it on the NLS equation in full detail. In Section 7.2 we present other rogue wave solutions, in various equations, which our method can potentially be used to obtain.

CHAPTER 2

THE CAMASSA-HOLM NONLINEAR SCHRÖDINGER EQUATION IN ONE SPACE DIMENSION

2.1 Model and continuous-wave solution

As indicated above, our aim is to study the CH-NLS equation. This model was derived in [26, 27] when developing a theory of a deformation of hierarchies of integrable systems. In fact, the CH-NLS equation is the deformation of the NLS equation, in the same sense as the CH equation is the deformation of the KdV equation. In its standard dimensionless form, the CH-NLS equation reads:

$$im_t + u_{xx} + 2\sigma m(|u|^2 - a^2|u_x|^2) = 0, \qquad m = u - a^2 u_{xx}, \tag{2.1}$$

where subscripts denote partial derivatives, $u(x,t)$ is a complex field, $\sigma = \pm 1$ pertains, respectively, to focusing or defocusing nonlinearity, while a is a constant arising within the Helmholtz operator. Obviously, for $a = 0$ the above model reduces to the standard, completely integrable NLS equation. In terms of the complex field u, the CH-NLS equation can be expressed as:

$$iu_t + u_{xx} + 2\sigma u|u|^2 - ia^2 u_{xxt} - 2\sigma a^2 u|u_x|^2 - 2\sigma a^2 u_{xx}|u|^2 + 2\sigma a^4 u_{xx}|u_x|^2 = 0. \tag{2.2}$$

To start our analysis, we use the Madelung transformation $u(x,t) = u_0\rho(x,t)\exp[i\phi(x,t)]$, decomposing the complex field $u(x,t)$ into its density $\rho(x,t)$ and phase $\phi(x,t)$; here, u_0

is an arbitrary complex constant. The resulting system of PDEs for $\rho(x,t)$ and $\phi(x,t)$ possesses the exact (uniform) steady-state solution:

$$\rho = 1, \qquad \phi = 2\sigma|u_0|^2 t, \tag{2.3}$$

corresponding to the continuous-wave (cw): $u = u_0 \exp(2i\sigma|u_0|^2 t)$. The stability of the cw solution (studied also in [27]) can be investigated as follows. Let

$$\rho = 1 + \tilde{\rho}, \qquad \phi = 2\sigma|u_0|^2 t + \tilde{\phi}, \tag{2.4}$$

where small perturbations $\tilde{\rho}$, $\tilde{\phi}$ are assumed to be $\propto \exp(ikx - i\omega t)$, while k and ω denote the wavenumber and frequency. Substituting Eqs. (2.4) into the equations for $\rho(x,t)$ and $\phi(x,t)$, we find that the latter obey the dispersion relation:

$$\omega^2 = \frac{k^2(-4\sigma|u_0|^2 + k^2)}{(1 + a^2k^2)^2}. \tag{2.5}$$

It is observed that in the case of the defocusing nonlinearity, i.e., for $\sigma = -1$, the cw solution is always modulationally stable, i.e., $\omega \in \mathbb{R}\ \forall k \in \mathbb{R}$. On the other hand, for a focusing nonlinearity, $\sigma = +1$, the cw solution is unstable for $k^2 < 4|u_0|^2$: in this case, perturbations grow exponentially, with the instability growth rate given by $\mathrm{Im}(k)$. Note that, for $a = 0$, Eq. (2.5) reduces to the well-known [16, 17] result for the modulational (in)stability of the NLS equation: $\omega^2 = k^2(-4\sigma|u_0|^2 + k^2)$. Thus, as was also found in [27], the interval of modulationally unstable wavenumbers is shared between NLS and CH-NLS and, in both cases, the defocusing realm of $\sigma = -1$ is modulationally stable.

Below we consider the defocusing nonlinearity case and seek nonlinear excitations – i.e., dark or antidark solitons – which propagate on top of the (stable in this case) cw background. Notice that, for $\sigma = -1$, the long-wavelength limit ($k \to 0$) of Eq. (2.5) provides

the so-called "speed of sound", $\omega/k \equiv C = \pm 2u_0$ (with the sign $\pm$ denoting the propagation direction), namely the velocity of small-amplitude linear excitations propagating on top of the cw background.

2.2 Asymptotic expansions and solitons

2.2.1 The Boussinesq equation

We start our perturbation theory considerations by noting that the dispersion relation (2.5) is similar to the one of the Boussinesq equation, i.e., $\omega^2 \sim k^2C^2 + k^4$, (for $a^2k^2 \ll 1$). This suggests the potential asymptotic reduction of the density and phase equations to a Boussinesq-like equation. Indeed, let us seek solutions in the form of the following asymptotic expansions:

$$\phi = -2|u_0|^2 t + \sqrt{\epsilon}\Phi, \qquad \rho = 1 + \epsilon\rho_1 + \epsilon^2\rho_2 + \cdots, \tag{2.6}$$

where $0 < \epsilon \ll 1$ is a formal small parameter, while the unknown real functions Φ and ρ_j ($j = 1, 2, \ldots$) are assumed to depend on the slow variables X and T defined as:

$$X = \sqrt{\epsilon}x, \qquad T = \sqrt{\epsilon}t. \tag{2.7}$$

Substituting Eqs. (2.6) into the equations for $\rho(x,t)$ and $\phi(x,t)$ and using the variables in Eq. (2.7), we obtain the following results. First, the equation for the phase leads, at orders $\mathcal{O}(\epsilon^{3/2})$ and $\mathcal{O}(\epsilon^{5/2})$, to the following equations:

$$\Phi_T + C^2\rho_1 = 0, \tag{2.8}$$

$$a^2\Phi_{XXT} - 2|u_0|^2(2\rho_2 + 3\rho_1^2 - a^2\Phi_X^2) + \rho_{1XX} - \rho_1\Phi_T - \Phi_X^2 = 0. \tag{2.9}$$

Second, the equation for the density leads at orders $\mathcal{O}(\epsilon)$ and $\mathcal{O}(\epsilon^2)$ to the equations:

$$\Phi_{XX} + \rho_{1T} = 0, \tag{2.10}$$

$$\rho_{2T} + 2a^2\Phi_X\Phi_{XT} + a^2C^2\Phi_{XX}\rho_1 + a^2\Phi_T\Phi_{XX} - a^2\rho_{1XXT} \\ +2\Phi_X\rho_{1X} + \Phi_{XX}\rho_1 = 0. \tag{2.11}$$

It is now possible to eliminate the functions ρ_1 and ρ_2 from the system of Eqs. (2.8)-(2.11), and derive the following equation for $\Phi(X,T)$:

$$\Phi_{TT} - C^2\Phi_{XX} + \epsilon\Big\{2a^2\Phi_{XXTT} - 4\Phi_X\Phi_{XT}(1-3a^2|u_0|^2) \\ -2\Phi_T\Phi_{XX} - \Phi_{XXXX}\Big\} = \mathcal{O}(\epsilon^2). \tag{2.12}$$

At the leading-order, Eq. (2.12) is a second-order linear wave equation, while at order $\mathcal{O}(\epsilon)$ incorporates fourth-order dispersion and quadratic nonlinear terms, resembling the Boussinesq and the Benney-Luke [84] equations. These models have been used to describe bidirectional shallow water waves in the framework of small-amplitude and long-wavelength approximations; see, e.g., the expositions of [11, 19]. They were also used in other contexts including ion-acoustic waves in plasmas [18, 85], mechanical lattices and electrical transmission lines [86].

It is worth mentioning that an analysis similar to that presented above can also be performed in two-dimensional (2D) settings: indeed, 2D Boussinesq equations were derived from 2D NLS equations with either a local [87] or a nonlocal [39, 40] defocusing nonlinearity. Such studies are also relevant to investigations concerning the transverse instability of planar dark solitons [88].

2.2.2 The KdV equation

Next, using a multiscale expansion method similar to the one employed in the water wave problem [11], we will now derive from the Boussinesq equation a pair of KdV equations for right- and left-going waves. These models will be obtained under the additional

assumption of unidirectional propagation. We thus seek solutions of Eq. (2.12) in the form of the asymptotic expansion:

$$\Phi = \Phi_0 + \epsilon\Phi_1 + \cdots , \tag{2.13}$$

where the unknown functions Φ_j ($j = 1, 2, \ldots$) depend on the variables:

$$\chi = X - CT, \qquad \tilde{\chi} = X + CT, \qquad \mathcal{T} = \epsilon T, \tag{2.14}$$

(recall that $C^2 = 4|u_0|^2$). Substituting Eq. (2.13) into Eq. (2.12), and using Eq. (2.14), we obtain the following results. First, at the leading order, $\mathcal{O}(1)$, we obtain the wave equation:

$$-4C^2\Phi_{0\chi\tilde{\chi}} = 0, \tag{2.15}$$

which implies that Φ_0 can be expressed as a superposition of a right-going wave, $\Phi_0^{(R)}$, depending on χ, and a left-going wave, $\Phi_0^{(L)}$, depending on $\tilde{\chi}$, namely:

$$\Phi_0 = \Phi_0^{(R)} + \Phi_0^{(L)}. \tag{2.16}$$

Second, at $\mathcal{O}(\epsilon)$, we obtain:

$$\begin{aligned} 4C^2\Phi_{1\chi\tilde{\chi}} = C(3a^2C^2 - 2)(\Phi_{0\chi}^{(R)}\Phi_{0\tilde{\chi}\tilde{\chi}}^{(L)} - \Phi_{0\tilde{\chi}}^{(L)}\Phi_{0\chi\chi}^{(R)}) \\ + \Big[2C\Phi_{0\mathcal{T}}^{(L)} - \frac{3C}{2}(2 - a^2C^2)\Phi_{0\tilde{\chi}}^{(L)2} - (1 - 2a^2C^2)\Phi_{0\tilde{\chi}\tilde{\chi}\tilde{\chi}}^{(L)}\Big]_{\tilde{\chi}} \\ - \Big[2C\Phi_{0\mathcal{T}}^{(R)} - \frac{3C}{2}(2 - a^2C^2)\Phi_{0\chi}^{(R)2} + (1 - 2a^2C^2)\Phi_{0\chi\chi\chi}^{(R)}\Big]_{\chi}. \end{aligned} \tag{2.17}$$

It is now observed that when integrating Eq. (2.17) with respect to χ or $\tilde{\chi}$ secular terms arise from the square brackets in the right-hand side of this equation, which are functions of χ or $\tilde{\chi}$, not both. Hence, we set the secular terms to zero so as to avoid secular growth, and obtain two uncoupled nonlinear evolution equations for $\Phi_0^{(R)}$ and $\Phi_0^{(L)}$.

Next, employing Eq. (2.8), it is straightforward to find that the amplitude ρ_1 can also be decomposed to a left- and a right-going wave, i.e., $\rho_1 = \rho_1^{(R)} + \rho_1^{(L)}$, with

$$\Phi_{0\chi}^{(R)} = C\rho_1^{(R)}, \quad \Phi_{0\tilde{\chi}}^{(L)} = -C\rho_1^{(L)}. \tag{2.18}$$

To this end, using the above equations for $\Phi_0^{(R)}$ and $\Phi_0^{(L)}$ yields the following equations for $\rho_1^{(R)}$ and $\rho_1^{(L)}$:

$$2C\rho_{1\mathcal{T}}^{(R)} - 3C^2(2 - a^2C^2)\rho_1^{(R)}\rho_{1\chi}^{(R)} + (1 - 2a^2C^2)\rho_{1\chi\chi\chi}^{(R)} = 0, \tag{2.19}$$

$$2C\rho_{1\mathcal{T}}^{(L)} + 3C^2(2 - a^2C^2)\rho_1^{(L)}\rho_{1\tilde{\chi}}^{(L)} - (1 - 2a^2C^2)\rho_{1\tilde{\chi}\tilde{\chi}\tilde{\chi}}^{(L)} = 0. \tag{2.20}$$

The above equations are two KdV equations for left- and right-going waves. Pertinent KdV soliton solutions will be used below for the construction of approximate soliton solutions of the CH-NLS equation.

2.2.3 Dark and antidark solitons of the CH-NLS equation

To proceed further, we focus on the right-going wave and introduce the transformations:

$$\hat{\mathcal{T}} = \Big(\frac{1 - 2a^2C^2}{2C}\Big)\mathcal{T}, \qquad \rho_1^{(R)} = \frac{2}{C^2}\left(\frac{1 - 2a^2C^2}{2 - a^2C^2}\right)U, \tag{2.21}$$

to express the KdV Eq. (2.19) in its standard form:

$$U_{\hat{\mathcal{T}}} - 6UU_\chi + U_{\chi\chi\chi} = 0. \tag{2.22}$$

The above equation possesses the commonly known (see, e.g., [11]) soliton solution:

$$U = -\frac{1}{2}\beta\,\mathrm{sech}^2\Big[\frac{\sqrt{\beta}}{2}(\chi - \beta\hat{\mathcal{T}} + \chi_0)\Big] \tag{2.23}$$

where arbitrary constants $\beta > 0$ and χ_0 set, respectively, the amplitude (as well as the width and velocity) and the initial position of the soliton. Using this solution and reverting

transformations back to the original variables, we find the following approximate [valid up to order $\mathcal{O}(\epsilon)$] solution of Eq. (2.1):

$$u \approx u_0\Big[1 - \frac{\epsilon\beta}{C^2} q\,\mathrm{sech}^2(\xi)\Big]\exp\Big[-2i|u_0|^2 t - i\frac{\sqrt{\epsilon\beta}}{C} q\tanh(\xi)\Big], \tag{2.24}$$

$$\xi = \frac{1}{2}\sqrt{\epsilon\beta}\left[x - \left(C + \frac{\epsilon\beta(1-2a^2C^2)}{2C}\right)t + x_0\right], \tag{2.25}$$

where the parameter q is given by:

$$q = \frac{1-2a^2C^2}{2-a^2C^2}, \tag{2.26}$$

and we have implicitly assumed that $C = 2u_0$. The corresponding solution of Eq. (2.20) (the left-moving soliton) is given by the same set of equations, but for $C = -2u_0$.

At this point, it is important to mention that the approximate soliton solution (2.26) of the CH-NLS equation describes two types of solitons: for $q > 0$ the solitons are dark (density dips on top of the cw background of amplitude u_0), while for $q < 0$ the solitons are antidark (density humps on top of the cw background). The sign of parameter q depends on the range of values of a single quantity $p \equiv a^2C^2 = 4a^2|u_0|^2$: indeed, if $1/2 < p < 2$ the solitons are antidark, else they are dark. For a similar scenario, but in a different class of defocusing NLS models, see [33–37], as well as [38–40] for recent work on nonlocal media.

2.3 Numerical Exploration

In this section we investigate the accuracy of our analytical predictions against direct numerical simulations performed by using the Exponential Time-Differencing 4th-order Runge-Kutta (ETDRK4) scheme of [89, 90]. However, before proceeding further, it is relevant to discuss at first the specific methodology used.

2.3.1 Numerical methods

First, we introduce the transformation $u(x,t) = u_0 \exp\left(-2i|u_0|^2 t\right) \psi(x,t)$, and rewrite the CH-NLS equation as:

$$i\hat{m}_t + \psi_{xx} - 2|u_0|^2 \hat{m}(|\psi|^2 - a^2|\psi_x|^2 - 1) = 0, \tag{2.27}$$

where $\hat{m} = \psi - a^2\psi_{xx}$. As is also the case with the defocusing NLS, this has the advantage of removing the time-dependent phase factor from subsequent calculations (and hence also from the boundary conditions). It is then clear that the approximate soliton solution of Eq. (2.27) [cf. Eq. (2.24)] is given by

$$\psi \approx \Big[1 - \frac{\epsilon\beta}{C^2} q \,\mathrm{sech}^2(\xi)\Big] \exp\Big[-i\frac{\sqrt{\epsilon\beta}}{C} q \tanh(\xi)\Big]. \tag{2.28}$$

While one can use inhomogeneous Dirichlet or homogeneous Neumann boundary conditions to tackle this problem, here we follow a different path. Due to our interest towards a spectral implementation of ETDRK4, we seek to realize periodic boundary conditions. To reconcile that with the nature of our dark soliton solutions, we solve the initial value problem (IVP) of Eq. (2.27) with an initial condition $\psi(x,0) = \psi_0$ on the truncated spatial domain $[-L, L]$, with the initial condition

$$\psi(x,0) = \psi_0 \exp\left[-\left(\frac{x}{L^*}\right)^{\gamma}\right]. \tag{2.29}$$

Here, L^*, with $0 < L^* < L$, is the (sufficiently large) width of the background pulse, while the particular value of the exponent $\gamma \gg 1$ is not especially important; here we use $\gamma = 34$. Notice that for $x/L^* \ll 1$ the initial condition reduces to ψ_0 and thus the dynamics of the original IVP (on a smaller interval) can be obtained. Indeed, we have ensured that this is the case by considering different values of L^* and L and checking that the dynamics do not change. For the figures shown below, we have used $L = 2500$ and $L^* = 1500$.

For all simulations below involving a single soliton (cf. Figs. 2.1-2.3), for ψ_0 we use:

$$\psi_0 = \left[1 - \frac{\epsilon\beta}{C^2} q \,\mathrm{sech}^2(\xi_0)\right] \exp\left[-i\frac{\sqrt{\epsilon\beta}}{C} q \tanh(\xi_0)\right], \tag{2.30}$$

where $\xi_0 = \frac{1}{2}\sqrt{\epsilon\beta}(x+100)$, $C = 2u_0$ and q as defined in Eq. (2.26). On the other hand, for simulations involving two solitons (cf. Fig. 2.4 except for panel 2.4(e) which will be explained below), we use for ψ_0 the product:

$$\begin{aligned} \psi_0 &= \left[1 - \frac{\epsilon\beta}{C_+^2} q_1 \mathrm{sech}^2(\xi_+)\right] \exp\left[-i\frac{\sqrt{\epsilon\beta}}{C_+} q_1 \tanh(\xi_+)\right] \\ &\times \left[1 - \frac{\epsilon\beta}{C_-^2} q_2 \,\mathrm{sech}^2(\xi_-)\right] \exp\left[-i\frac{\sqrt{\epsilon\beta}}{C_-} q_2 \tanh(\xi_-)\right], \end{aligned} \tag{2.31}$$

where $\xi_\pm = \frac{1}{2}\sqrt{\epsilon\beta}(x \pm 200)$, $C_\pm = \pm 2u_0$, and $q_{1,2} = (1 - 2a_{1,2}^2 C^2)/(2 - a_{1,2}^2 C^2)$.

At this point we should also note the following: In the single-soliton simulations, the same value of a is used both for the PDE and the initial condition. On the other hand, for the two-soliton simulations, a_1 and a_2 appearing through $q_{1,2}$ in Eq. (2.31) are treated as independent parameters, not related to parameter a involved in the CH-NLS equation. Thus, in the two-soliton collision case, we fix the value of a in Eq. (2.27), as well as all other parameter values (along with a_1 and a_2) involved in the initial condition of Eq. (2.31), and integrate numerically Eq. (2.27) via the ETDRK4 integrator. The rationale of this towards considering different collision scenarios is discussed below.

2.3.2 Results of direct simulations

First, our aim is to explore the validity of our asymptotic, small-amplitude soliton solution and its proximity to a true solution of the CH-NLS model. We thus fix all parameters in Eq. (2.28) except for ϵ, which we allow to vary. We then calculate the L^2 norm of the difference between the asymptotic solution and the numerical solution on the space-time domain $[-300, 300] \times [0, 100]$.

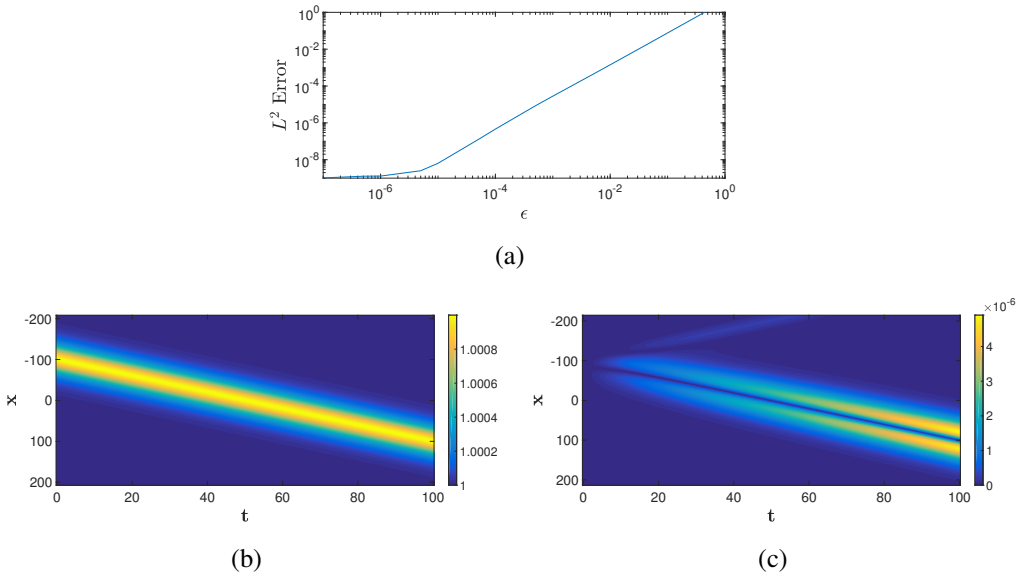

(a)

(b)

(c)

Figure 2.1: (a) Log-log plot of the L^2 error between the predicted solution (2.24) and the numerical solution as a function of ϵ. All other parameter values fixed at $u_0 = 1$, $a = 0.5$, $\beta = 0.1$; in this case, parameter $p = 1$, i.e., $p \in (1/2, 2)$, which means that the soliton is antidark (cf. text). (b) Contour plot showing the evolution of the density of the corresponding antidark soliton, for $\epsilon = 0.04$. (c) Same as (b) but for the difference between the densities of the analytical and the numerical solution. It can be observed that the error becomes larger as time increases; this is especially so at the "wings" (rather than the core) of the soliton.

Figure 2.1(a) shows a log-log plot of the norm as a function of ϵ; parameter values can be found in the caption, and correspond to an antidark soliton. As expected, the analytical and numerical solutions agree very well for sufficiently small ϵ (the error is at the order of numerical precision), but start to show differences once ϵ increases.

The progressively increasing difference usually assumes the form of emerging linear radiative wavepackets. It may also have the more dramatic effect of splitting into a left-moving soliton and a right-moving soliton. Figure 2.1(b) shows a contour plot depicting the evolution of the density of the asymptotic antidark soliton solution, when ϵ is small. On the other hand, Fig. 2.1(c) shows a contour plot of the difference between the absolute value of the amplitudes of the numerical solution and the asymptotic solution. Similar results have also been obtained for the case of dark solitons. In particular, Fig. 2.2(a) shows a contour plot depicting the evolution of the density of a dark soliton for $\epsilon = 0.04$, while Fig. 2.2(b) compares the asymptotic and numerical solutions.

To test how the asymptotic analysis and the validity of the approximate soliton solutions fail, we have also examined the case where ϵ is quite large. Results of simulations for anti-dark and dark solitons are respectively illustrated in Figs. 2.3(a) and 2.3(b), in the case of $\epsilon = 1$; other parameter values are as in Figs. 2.1 and 2.2. It is observed that the antidark soliton of Fig. 2.3(a) agrees very well with the corresponding asymptotic solution (as the error in Fig. 2.1(a) suggests). This clearly showcases the fact that the relevant parameter controlling the amplitude of the solitary wave is $\epsilon\beta q/C^2 = -0.025$ in this case, hence the analytical approximation is still very accurate. On the other hand, the dark soliton in Fig. 2.3(b) initially splits into a small-amplitude left-moving soliton (with no radiation) and into a right-moving one (with much radiation). We remark that Fig. 2.3(b) is fairly generic among the large ϵ solutions.

Next, in Fig. 2.4, we show numerical results for soliton collisions. In particular, Figs. 2.4(a) and 2.4(b) depict, respectively, the collisions between two identical dark and two identical antidark solitons of opposite speeds, for $\epsilon = 0.1$. As a contrast to Figs. 2.4(a) and 2.4(b)

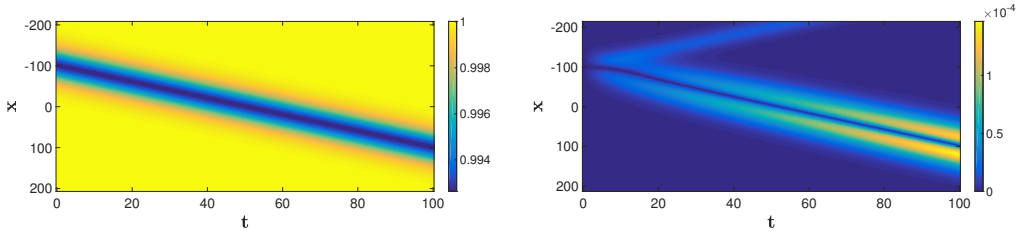

(a) (b)

Figure 2.2: (a) Same as Fig. 2.1(a), but for a dark soliton, for $u_0 = 1$, $a = 0.8$, $\beta = 0.1$, $\epsilon = 0.04$; note that, here, $p = 2.56 > 2$ and thus the soliton is indeed of the dark type (cf. text). (b) Same as Fig. 2.1(b), but for the dark soliton of panel (a). Again, the error becomes larger as time increases, especially at the "wings" of the soliton.

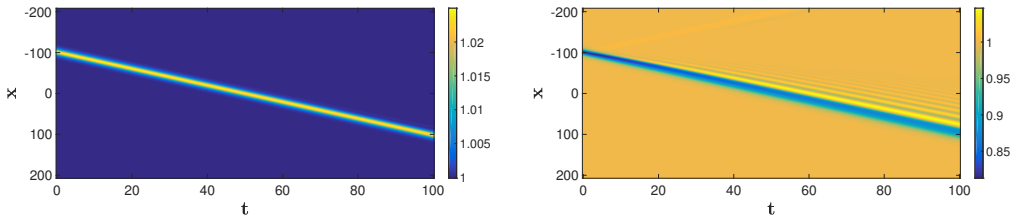

(a) (b)

Figure 2.3: Panels (a) and (b) are the corresponding large ϵ results of Figs. 2.1(a) and 2.2(a), respectively. Parameter values are the same as in Figs. 2.1(a) and 2.2(a) except that $\epsilon = 1$.

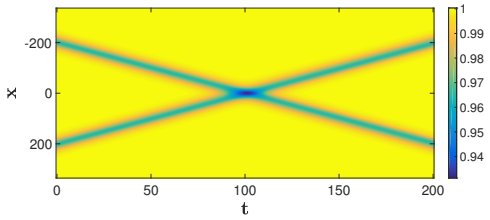

(a) $a = a_1 = a_2 = 0.75$, $b = 0.1$, $\epsilon = 0.1$, $u_0 = 1$

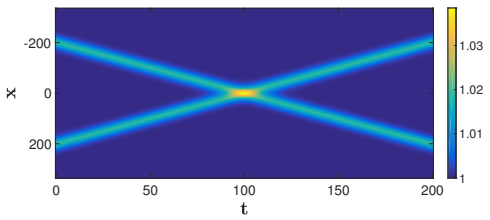

(b) $a = a_1 = a_2 = 0.65$, $b = 0.1$, $\epsilon = 0.1$, $u_0 = 1$

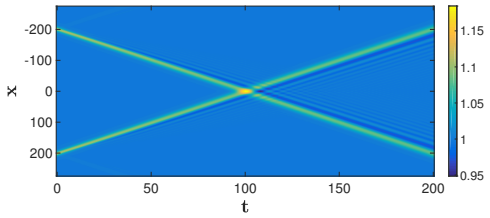

(c) $a = a_1 = a_2 = 0.62$, $b = 0.1$, $\epsilon = 1$, $u_0 = 1$

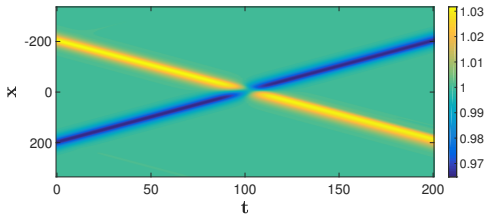

(d) $a = 0.75$, $a_1 = 0.67$, $a_2 = 0.75$, $b = 0.1$, $\epsilon = 0.1$, $u_0 = 1$

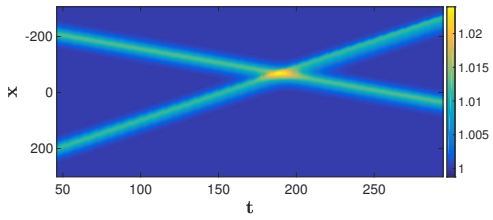

(e) $a = a_1 = a_2 = 0.62$, $b = 0.1$, $\epsilon = 0.1$, $u_0 = 1$, $\nu = -0.7$

Figure 2.4: Collisions of various dark and anti-dark solitons shown via contour plots of there respective amplitudes. The intial condition used for each was Eq. (2.31) with the given parameter values – except (e) in which a gallilean boost was applied.

where a relatively small value of ϵ was used, Fig. 2.4(c) shows the collision of two antidark solitons for $\epsilon = 1$. It is worth noting that although emission of radiation is much stronger in this case, the solitons practically remain unscathed after their head-on collision. Here it should be mentioned that the initial condition for all the above three scenarios was Eq. (2.31) with corresponding parameters found in the figure captions; particularly, in all cases, we used $a = a_1 = a_2$.

As a final addition, we consider two special situations not predicted by the asymptotic analysis but found, rather, by purely numerical means. Let us first recall [cf. Eq. (2.26)] that antidark solitons exist when $1/2 < p \equiv a^2C^2 < 2$ and dark solitons otherwise. The asymptotic solution then implies that dark and antidark solitons should not coexist on the same range of a values. Nevertheless, for values around the critical point $p = 2$, one might expect that dark (or antidark) solitons may retain their form for relatively long times even if, technically speaking, they are not supported in the domain $p < 2$ (or $p > 2$). We have found that this is indeed the case: as shown in Fig. 2.4(d), a collision of an antidark soliton and a dark soliton, obtained for $a_1 = 0.67$, $a_2 = 0.75$ and $a = 0.75$, is possible. It is observed that the antidark soliton appears to keep its form over the integration time (though it may very well decay over a sufficiently long –considerably longer than the horizon of the present dynamical considerations– period).

The second situation deals with the fact that all previous solitons have had nearly the same speed. This is no accident as the soliton velocity v is given by [cf. Eq. (2.25)]:

$$v = C + \frac{\epsilon\beta(1 - 2\alpha^2C^2)}{2C}. \tag{2.32}$$

Notice that when ϵ and β are small enough the velocity of the soliton approaches the speed of sound, i.e., $v \approx C = \pm 2|u_0|$. For instance, in the previous examples, we have used $u_0 = 1$ which makes the predicted soliton velocity $v \approx 2$ (as can also readily be observed in the figures). This fact implies that a collision between solitons of different speeds would not be possible because the solitons live on top of the same background.

Nevertheless, although the CH-NLS equation is not Galilean invariant, it is conceivable (at least for small enough a) that a Galilean boost should increase the velocity of individual solitons. Indeed, Fig. 2.4(e) shows the asymmetric collision of two dark solitons obtained by using the product of Eq. (2.31) and $\exp(i\nu x)$ as ψ_0 [note that the initial soliton positions are $x_0 = -250$ (left soliton) and $x_0 = 290$ (right soliton)]. Although not shown, the initial profile splits into a left-moving wave and right-moving wave, except that the boost causes the left-moving wave to travel much faster, enabling a collision with unequal speeds. We then observe that solitons of different speeds can coexist and that their collisions are also nearly elastic in the small (solitary wave) amplitude regime considered.

CHAPTER 3

THE CAMASSA-HOLM NONLINEAR SCHRÖDINGER EQUATION IN TWO SPACE DIMENSIONS

3.1 Model and its analytical consideration

3.1.1 Presentation of the model and some of its properties

As indicated above, our aim is to study the 2D CH-NLS equation, which is a generalization of the 1D model derived in [26, 27], when developing a theory of a deformation of hierarchies of integrable systems. The 2D CH-NLS equation is expressed as follows:

$$im_t + \Delta u + 2\sigma m(|u|^2 - a^2|\boldsymbol{\nabla} u|^2) = 0, \quad m = u - a^2\Delta u, \tag{3.1}$$

where $u(x, y, t)$ and $m(x, y, t)$ are complex fields, $\Delta = \partial_x^2 + \partial_y^2$ is the Laplacian in 2D, and $\boldsymbol{\nabla} = (\partial_x, \partial_y)$ is the gradient operator. In addition, $\sigma = \pm 1$ pertains, respectively, to focusing or defocusing nonlinearity, while the constant a arises within the Helmholtz operator; note that for $a = 0$ the above model reduces to the standard, 2D NLS equation, i.e., this parameter measures the "size" of the departure from the original NLS limit.

In terms of the complex field u, the CH-NLS equation can be expressed as:

$$iu_t + \Delta u + 2\sigma u|u|^2 - ia^2\Delta u_t - 2\sigma a^2 u|\boldsymbol{\nabla} u|^2 - 2\sigma a^2\Delta u|u|^2 + 2\sigma a^4\Delta u|\boldsymbol{\nabla} u|^2 = 0. \tag{3.2}$$

The simplest nontrivial solution of Eq. (3.2) is the continuous-wave (cw):

$$u = u_0 \exp(2i\sigma|u_0|^2 t), \tag{3.3}$$

where u_0 is an arbitrary complex constant. Since below we will seek nonlinear excitations (e.g., solitary waves) which propagate on top of this cw background, it is relevant to investigate if this solution is subject to modulational instability (MI): naturally, nonlinear excitations corresponding to an unstable background will be less physically relevant. The stability of the cw solution (3.3) can be investigated upon using the ansatz $u = u_0(1+\tilde{u})\exp(2i\sigma|u_0|^2 t + i\theta)$, where the small perturbations $\tilde{u}$ and θ are assumed to be $\propto \exp(i\boldsymbol{k}\cdot\boldsymbol{r} - i\omega t)$, with $\boldsymbol{r} = (x, y)$, while $\boldsymbol{k} = (k_x, k_y)$ and ω denote the perturbation wave-vector and frequency, respectively. Then, it can readily be found that ω and $k \equiv |\boldsymbol{k}|$ obey the following the dispersion relation:

$$\omega^2 = \frac{k^2(-4\sigma|u_0|^2 + k^2)}{(1+a^2k^2)^2}. \tag{3.4}$$

It is observed that in the case of the defocusing nonlinearity, i.e., for $\sigma = -1$, the cw solution is always modulationally stable, i.e., $\omega \in \mathbb{R}\ \forall k \in \mathbb{R}$. On the other hand, for a focusing nonlinearity, $\sigma = +1$, the cw solution is unstable for $k^2 < 4|u_0|^2$: in this case, perturbations grow exponentially, with the instability growth rate given by $\mathrm{Im}(k)$. Note that, for $a = 0$, and in the 1D case (e.g., $k_y = 0$), Eq. (3.4) reduces to the well-known [17] result for the modulational (in)stability of the NLS equation: $\omega^2 = k^2(-4\sigma|u_0|^2 + k^2)$. Clearly (and as was also found in the 1D case [27,91]), the MI band is shared between NLS and CH-NLS and, in both cases, the cw (3.3) is modulationally stable in the defocusing realm of $\sigma = -1$. For this case, it is also relevant to mention that the long-wavelength limit ($k \to 0$) of Eq. (3.4) provides the (squared) "sound velocity",

$$C^2 = 4|u_0|^2, \tag{3.5}$$

namely the velocity of small-amplitude linear excitations propagating on top of the cw background.

An important aside regarding Eq. (3.1) concerns its potential conservation laws. First of all, it has been verified (both analytically and numerically) that the mass

$$M = \int_{\mathbb{R}^2} |m|^2 dxdy \tag{3.6}$$

remains a conserved quantity. On the other hand, in the 1D context, the Hamiltonian of the system is a momentum-like quantity of the form:

$$P_{1D} = \frac{i}{2} \int_{\mathbb{R}} (\bar{m} u_x - m \bar{u}_x)\, dx \tag{3.7}$$

(where overbar denotes complex conjugation), while the Hamiltonian structure is non-canonical as discussed, e.g., in [27]. A natural generalization of this momentum in 2D (by analogy also with the standard NLS problem) is of the form:

$$P_{2D} = \frac{i}{2} \int_{\mathbb{R}^2} (\bar{m} \boldsymbol{\nabla} u - m \boldsymbol{\nabla} \bar{u})\, dxdy. \tag{3.8}$$

It appears to be an intriguing problem in its own right to explore whether this quantity is conserved and whether the generalization of the non-canonical Hamiltonian formulation in the higher dimensional case can be done.

3.1.2 Multiscale expansions and reduced models

We now consider small-amplitude slowly-varying modulations of the cw solution, and look for solutions of Eq. (3.2) in the form of the following asymptotic expansions:

$$u = u_0 \rho \exp\left[-2i|u_0|^2 t + i\epsilon^{1/2} \Phi(X, Y, T)\right], \tag{3.9}$$

$$\rho = 1 + \sum_{j=1}^{\infty} \epsilon^j \rho_j(X, Y, T), \tag{3.10}$$

where the phase Φ and densities ρ_j are unknown real functions of the slow variables

$$X = \epsilon^{1/2} x, \quad Y = \epsilon^{1/2} y, \quad T = \epsilon^{1/2} t, \tag{3.11}$$

while $0 < \epsilon \ll 1$ is a formal small parameter. Substituting the expansions (3.9)-(3.10) into Eq. (3.2), and separating real and imaginary parts, we obtain the following results. First, the real part of Eq. (3.2) leads, at orders $\mathcal{O}(\epsilon)$ and $\mathcal{O}(\epsilon^2)$, to the following equations:

$$\Phi_T + C^2\rho_1 = 0, \tag{3.12}$$

$$a^2\tilde{\Delta}\Phi_T - 2|u_0|^2(2\rho_2 + 3\rho_1^2 - a^2|\tilde{\boldsymbol{\nabla}}\Phi|^2) + \tilde{\Delta}\rho_1 - \rho_1\Phi_T - |\tilde{\boldsymbol{\nabla}}\Phi|^2 = 0, \tag{3.13}$$

where $\tilde{\Delta} \equiv \partial_X^2 + \partial_Y^2$ and $\tilde{\boldsymbol{\nabla}} \equiv (\partial_X, \partial_Y)$. Second, the imaginary part of Eq. (3.2), at orders $\mathcal{O}(\epsilon^{3/2})$ and $\mathcal{O}(\epsilon^{5/2})$ yields:

$$\rho_{1T} + \tilde{\Delta}\Phi = 0, \tag{3.14}$$

$$\rho_{2T} + (1 + a^2C^2)\rho_1\tilde{\Delta}\Phi + a^2\Phi_T\tilde{\Delta}\Phi - a^2\tilde{\Delta}\rho_{1T} + 2\tilde{\nabla}\Phi \cdot (a^2\tilde{\boldsymbol{\nabla}}\Phi_T + \tilde{\nabla}\rho_1) = 0. \tag{3.15}$$

Then, eliminating the functions ρ_1 and ρ_2 from the system of Eqs. (3.12)-(3.15), we derive the following equation for $\Phi(X, Y, T)$:

$$\Phi_{TT} - C^2\tilde{\Delta}\Phi + \epsilon\Big\{2a^2\tilde{\Delta}\Phi_{TT} - 4(1 - 3a^2|u_0|^2)(\tilde{\boldsymbol{\nabla}}\Phi_T \cdot \tilde{\boldsymbol{\nabla}}\Phi) \\ -2\Phi_T\tilde{\Delta}\Phi - \tilde{\Delta}^2\Phi)\Big\} = \mathcal{O}(\epsilon^2). \tag{3.16}$$

At the leading-order, Eq. (3.16) is a second-order linear wave equation, while at order $\mathcal{O}(\epsilon)$ it incorporates fourth-order dispersion and quadratic nonlinear terms, similar to the Boussinesq and the Benney-Luke [84] equations. These models have originally been used to describe bidirectional shallow water waves [11], but also ion-acoustic waves in plasmas [18], as well as mechanical lattices and electrical transmission lines [86]. Note that the

present analysis generalizes the results of [91] (where the 1D case was studied) to the 2D setting; in that regard, it is worth mentioning that similar 2D Boussinesq equations were derived from 2D NLS equations with either a local [87,88] or a nonlocal [92,93] defocusing nonlinearity.

Next, using a multiscale expansion method similar to the one employed in the water wave problem [11], we will derive the far-field of the Boussinesq equation, namely a pair of two KP equations for right- and left-going waves. These models will be obtained under the additional assumption of unidirectional propagation. We thus seek solutions of Eq. (3.16) in the form of the asymptotic expansion:

$$\Phi = \Phi_0 + \epsilon\Phi_1 + \cdots , \tag{3.17}$$

where the unknown functions Φ_j ($j = 1, 2, \ldots$) depend on the variables:

$$\chi = X - CT, \qquad \tilde{\chi} = X + CT, \qquad \mathcal{Y} = \sqrt{\epsilon}Y, \qquad \mathcal{T} = \epsilon T, \tag{3.18}$$

Substituting Eq. (3.17) into Eq. (3.16), and using Eq. (3.18), we obtain the following results. First, at the leading order, $\mathcal{O}(1)$, we obtain the wave equation:

$$-4C^2\Phi_{0\chi\tilde{\chi}} = 0, \tag{3.19}$$

which implies that Φ_0 can be expressed as a superposition of a right-going wave, $\Phi_0^{(R)}$, depending on χ, and a left-going wave, $\Phi_0^{(L)}$, depending on $\tilde{\chi}$, namely:

$$\Phi_0 = \Phi_0^{(R)} + \Phi_0^{(L)}. \tag{3.20}$$

Second, at $\mathcal{O}(\epsilon)$, we obtain the equation:

$$4C^2\Phi_{1\chi\tilde{\chi}} = C(3a^2C^2-2)(\Phi^{(R)}_{0\chi}\Phi^{(L)}_{0\tilde{\chi}\tilde{\chi}} - \Phi^{(L)}_{0\tilde{\chi}}\Phi^{(R)}_{0\chi\chi})$$
$$+\left\{\left[2C\Phi^{(L)}_{0\mathcal{T}} - \frac{3C}{2}(2-a^2C^2)\Phi^{(L)2}_{0\tilde{\chi}} - (1-2a^2C^2)\Phi^{(L)}_{0\tilde{\chi}\tilde{\chi}\tilde{\chi}}\right]_{\tilde{\chi}} - C^2\Phi^{(L)}_{0\mathcal{Y}\mathcal{Y}}\right\}$$
$$-\left\{\left[2C\Phi^{(R)}_{0\mathcal{T}} - \frac{3C}{2}(2-a^2C^2)\Phi^{(R)2}_{0\chi} + (1-2a^2C^2)\Phi^{(R)}_{0\chi\chi\chi}\right]_{\chi} + C^2\Phi^{(R)}_{0\mathcal{Y}\mathcal{Y}}\right\}. \quad (3.21)$$

When integrating Eq. (3.21) with respect to χ or $\tilde{\chi}$, it is observed that secular terms arise from the curly brackets in the right-hand side of this equation, which are functions of χ or $\tilde{\chi}$ alone, not both. Hence, these secular terms are set to zero, which leads to two uncoupled nonlinear evolution equations for $\Phi^{(R)}_0$ and $\Phi^{(L)}_0$. Next, employing Eq. (3.12), it is found that the amplitude ρ_1 can also be decomposed to a left- and a right-going wave, i.e., $\rho_1 = \rho^{(R)}_1 + \rho^{(L)}_1$, with

$$\Phi^{(R)}_{0\chi} = C\rho^{(R)}_1, \quad \Phi^{(L)}_{0\tilde{\chi}} = -C\rho^{(L)}_1. \quad (3.22)$$

Using these and the above equations for $\Phi^{(R)}_0$ and $\Phi^{(L)}_0$ yields the following equations for $\rho^{(R)}_1$ and $\rho^{(L)}_1$:

$$\left[2C\rho^{(R)}_{1\mathcal{T}} - 3C^2(2-a^2C^2)\rho^{(R)}_1\rho^{(R)}_{1\chi} + (1-2a^2C^2)\rho^{(R)}_{1\chi\chi\chi}\right]_{\chi} + C^2\rho^{(R)}_{1\mathcal{Y}\mathcal{Y}} = 0, \quad (3.23)$$

$$\left[2C\rho^{(L)}_{1\mathcal{T}} + 3C^2(2-a^2C^2)\rho^{(L)}_1\rho^{(L)}_{1\tilde{\chi}} - (1-2a^2C^2)\rho^{(L)}_{1\tilde{\chi}\tilde{\chi}\tilde{\chi}}\right]_{\tilde{\chi}} - C^2\rho^{(L)}_{1\mathcal{Y}\mathcal{Y}} = 0. \quad (3.24)$$

The result of this analysis is the emergence of two KP equations for left- and right-going waves. Without loss of generality, below we focus on the right-going wave. To proceed further, and express the KP of Eq. (3.23) in its standard form, we introduce the rescaling:

$$\hat{\mathcal{Y}} = \sqrt{\frac{3|1-2a^2C^2|}{C^2}}\mathcal{Y}, \qquad \hat{\mathcal{T}} = \Big(\frac{1-2a^2C^2}{2C}\Big)\mathcal{T}, \qquad \rho^{(R)}_1 = qU, \quad (3.25)$$

where the parameter q is given by:

$$q = \frac{2}{C^2}\left(\frac{1-2a^2C^2}{a^2C^2-2}\right). \tag{3.26}$$

Then, Eq. (3.23) is reduced to the form:

$$\left(U_{\hat{\tau}} + 6UU_{\chi} + U_{\chi\chi\chi}\right)_{\chi} + 3\delta U_{\hat{y}\hat{y}} = 0, \tag{3.27}$$

where $\delta = -\mathrm{sgn}(1-2a^2C^2) = \pm 1$. The case $\delta = -1$, or $1-2a^2C^2 > 0$, corresponds to the KP-I equation, which models waves in liquid thin films with large surface tension. On the other hand, $\delta = 1$, or $1-2a^2C^2 < 0$, corresponds to the KP-II equation, arising in the description of shallow water waves characterized by small surface tension (see, e.g., [11]).

3.2 Asymptotic Solutions and Numerical Exploration

Below, soliton solutions of the KP-I and KP-II models will be used for the construction of approximate soliton solutions of the original 2D CH-NLS equation. Furthermore, the dynamics of these structures will be studied by means of direct numerical simulations in the framework of the CH-NLS. For this numerical exploration presented below, we note the following. For the numerical integration of the original 2D CH-NLS, we use the Exponential Time-Differencing 4th-order Runge-Kutta (ETDRK4) scheme of [89, 90]; for details related to implementation, cf. [91]. The parameters used in the simulations can be found in the individual figure captions. If a figure shows a collision between two solitons, and only one set of parameters is given, then that set was used for both solitons. Lastly, the background amplitude has been set to unity for all simulations.

3.2.1 Line Solitons

We start with the case of line soliton solutions, which are supported by both KP-I and KP-II equations, given their quasi-1D nature, [cf. Eq. (3.27)] and are of the form [9, 11]:

$$U = \frac{1}{2}\gamma^2 \,\mathrm{sech}^2\Big[\frac{\gamma}{2}(\chi - \beta\hat{\mathcal{Y}} - \frac{\eta}{\gamma}\hat{\mathcal{T}} + \chi_0)\Big], \tag{3.28}$$

where η, γ and β are constants with $\eta = \gamma^2 + 3\delta\gamma\beta^2$, and $\delta = \pm 1$ for KP-I or KP-II, respectively. The solution (3.28) is characterized by the parameter γ associated with the soliton amplitude and the soliton direction β in the xy-plane, with $\beta = \tan(\gamma)$. Using Eq. (3.28), and reverting transformations back to the original variables, we find the following approximate (valid up to order $O(\epsilon)$) solution of the CH-NLS, Eq. (3.1):

$$u \approx u_0\Big[1 + \frac{\epsilon\gamma^2 q}{2}\,\mathrm{sech}^2(\xi)\Big]\exp\Big[-2i|u_0|^2 t + i\sqrt{\epsilon}C\gamma q\tanh(\xi)\Big], \tag{3.29}$$

where

$$\xi = \frac{\sqrt{\epsilon}\gamma}{2}\left[x - \sqrt{\epsilon}\beta\sqrt{\frac{3|1-2a^2C^2|}{C^2}}y - \left(C + \frac{\epsilon\eta(1-2a^2C^2)}{2\gamma C}\right)t + x_0\right]. \tag{3.30}$$

Here, it is important to mention that the approximate soliton solution (3.29) describes two types of solitons: if $q > 0$ the solitons are dark, having the form of density dips on top of the cw background of amplitude u_0; if $q < 0$, the solitons are anti-dark, having the form of density humps on top of the cw background. The sign of parameter q depends on the range of values of a single parameter $p \equiv a^2C^2 = 4a^2|u_0|^2$: indeed, if $1/2 < p < 2$ the solitons are antidark, else they are dark.

Using direct numerical simulations (results not shown here) we have found that for sufficiently small ϵ, of the order $\mathcal{O}(10^{-2})$, solitons of both types do exist and propagate undistorted, without emitting significant radiation. On the other hand, solitons of relatively large amplitudes feature a different behavior, because – as expected – the results of the asymptotic analysis become less accurate. Indeed, this is shown in Fig. 3.1, where the evolution of a dark line soliton [cf. initial condition, at $t = 0$, in panel (a)] is depicted. As is observed in panel (b), the dark soliton "ejects" an anti-dark line soliton, and a radiation tail forms. Nevertheless, it should be pointed out that even for such relatively large amplitudes,

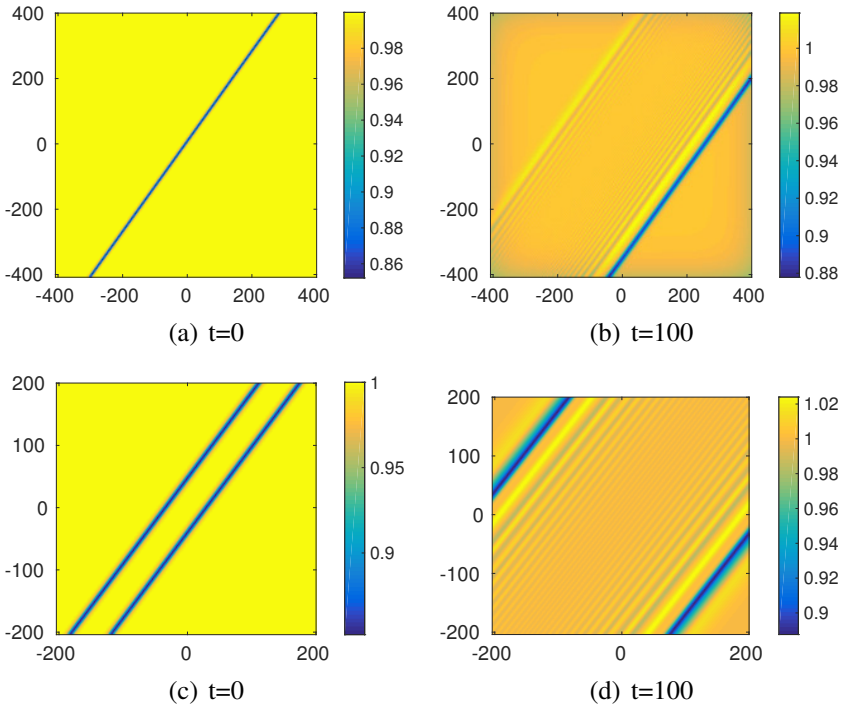

Figure 3.1: Top panels: Contour plots showing the evolution of the density of one line dark soliton of relatively large amplitude, with $\epsilon = 0.1$, at $t = 0$ [panel (a)] and $t = 100$ [panel (b)]. It is observed that the soliton splits into two waves, a dark and an anti-dark, and also emits radiation. Bottom panels: Collision between two line dark solitons. Panel (c) shows the initial condition, at $t = 0$, and panel (d) shows the outcome of the head-on collision, at $t = 100$. Here, the leftmost soliton appears as the rightmost one, and vice versa. Parameter values: $a = 1$, $\gamma = 1.3$, and $\beta = 1$.

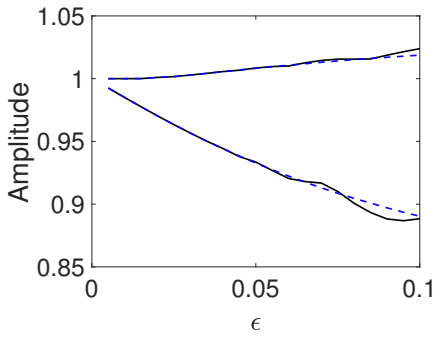

(a)

Figure 3.2: Relative elasticity of dark line soliton collisions. The dashed lines represent the maximum and minimum values of the amplitude (vertical axis), for each value of epsilon shown (horizontal axis), that occurs for the evolution of a single dark line soliton (as in Fig. 3.1(a),(b)). The solid lines represent the maximum and minimum amplitude, for each value of epsilon, that occur for the collision of two dark line solitons (as in Fig. 3.1(c),(d)). Note that although a collision takes places, the relative amplitudes of the line solitons is very similar to that as if the collision never took place; stated differently, the two line solitons interact very weakly despite the large amplitudes. Note that the value of the amplitude given in the plot was taken at $t = 100$ with the same parameter values as in Fig. 3.1.

the approximate soliton solutions are supported by the system and can even undergo almost elastic collisions with each other. An example pertaining to the case of a pair of dark line solitons is shown in panels (c) and (d) of Fig. 3.1. Here, the collision is deemed as almost elastic, in the sense that the observed dynamics for each soliton is identical to the one depicted in panel (b), i.e., the ejection of the anti-dark soliton and the emission of radiation would occur even if each of the solitons evolved by itself (i.e., in the absence of the other one).

In Fig. 3.2, we explore further the relative elasticity of the collisions for different parameter values. In particular, in the figure we show a typical (for different values of a and C) result representing the elasticity of the collisions as a function of ϵ, i.e., the parameter characterizing the amplitude of the solitary wave. More specifically, we compare the amplitude of the solitonic depression (and that of the background) for a single soliton (dashed line) and for two solitons (solid line) as a result of their collision. It can be seen that in the case of two solitons the amplitudes remain identical to that of one soliton (implying

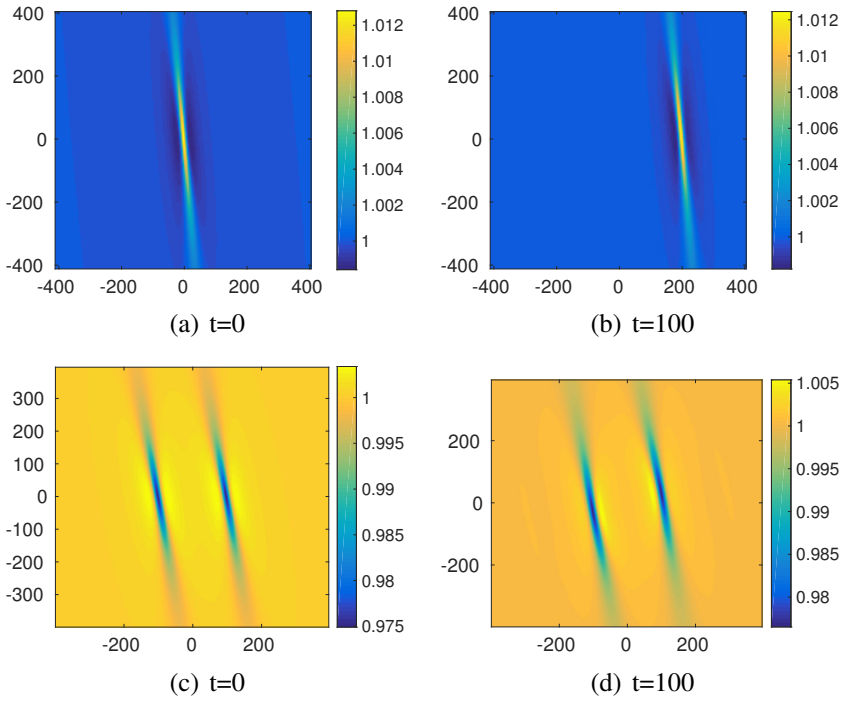

Figure 3.3: Top panels: Contour plots showing the evolution of the density of one anti-dark lump soliton of relatively small amplitude, with $\epsilon = 0.01$, at $t = 0$ [panel (a)] and $t = 100$ [panel (b)]. It is observed that the lump evolves undistorted and no emission of radiation is observed. Parameter values: $a = \frac{1}{2}$, $\gamma = 1$, $\beta = 0.8$. Bottom panels: Collision between two dark lumps. Panel (c) shows the initial condition, at $t = 0$, and panel (d) shows the outcome of the head-on collision, at $t = 100$. Here, the leftmost lump appears as the rightmost one, and vice versa; again, the radiation is barely discernible at $t = 100$. Parameter values: $a = \frac{1}{2}$, $\epsilon = 0.005$, $\gamma = 1$, $\beta = 0.85$.

that the collisions are essentially elastic) for values of ϵ up to around 0.07. For higher ϵ values it is clear that the amplitude of the background increases further, while the solitonic depression is also modified as a result of the collision. These features are a byproduct of the partial inelasticity of the associated collisions. We have found this result to be similar to other cases of a and C, providing in this way a rough guideline about the deviation of soliton collisions from elasticity.

3.2.2 Lump solitons

Next, we consider lump solitons, which are weakly localized (exponentially decaying) two-dimensional soliton solutions of the KP-I equation. The lump soliton is of the form:

$$U = 4\frac{-\Big[\chi+\gamma\hat{\mathcal{Y}}+3(\gamma^2-\beta^2)\hat{\mathcal{T}}\Big]^2+\beta^2(\hat{\mathcal{Y}}+6\gamma\hat{\mathcal{T}})^2+1/\beta^2}{\Big\{\Big[\chi+\gamma\hat{\mathcal{Y}}+3(\gamma^2-\beta^2)\hat{\mathcal{T}}\Big]^2+\beta^2(\hat{\mathcal{Y}}+6\gamma\hat{\mathcal{T}})^2+1/\beta^2\Big\}^2}, \tag{3.31}$$

where γ and β are real parameters. As in the case of the line soliton, we use this solution and revert transformations back to the original variables, and find the following approximate (valid up to order $O(\epsilon)$) solution of Eq. (3.1):

$$u \approx u_0(1+\epsilon q w_1)\exp[-2i|u_0|^2 t + i\sqrt{\epsilon}Cqw_2], \tag{3.32}$$

where

$$\begin{aligned} w_1 &= 4\frac{z_- + \frac{1}{\sqrt{\epsilon}\beta^2}}{\sqrt{\epsilon}\Big[z_+ + \frac{1}{\sqrt{\epsilon}\beta^2}\Big]^2}, \\ w_2 &= 4\frac{z_0}{\epsilon^{3/2}\beta^2\Big(6\gamma\sqrt{\epsilon}\frac{1-2a^2C^2}{2C}t + \sqrt{\frac{3|1-2a^2C^2|}{C^2}}y\Big)^2 + z_0 + \frac{1}{\sqrt{\epsilon}\beta^2}}, \end{aligned} \tag{3.33}$$

and

$$\begin{aligned} z_\pm = \; & \pm \Big[x+\gamma\sqrt{\frac{3\epsilon|1-2a^2C^2|}{C^2}}y - \Big(C - \frac{3\epsilon(\gamma^2-\beta^2)(1-2a^2C^2)}{2C}\Big)t\Big]^2 \\ & + \beta^2\Big[\sqrt{\frac{3\epsilon|1-2a^2C^2|}{C^2}}y + \frac{6\epsilon\gamma(1-2a^2C^2)}{2C}t\Big]^2 \end{aligned} \tag{3.34}$$

In the case of small-amplitude lumps, e.g., for $\epsilon = 0.01$, direct numerical simulations are in very good agreement with the analytical findings. Indeed, in Fig. 3.3, which depicts the evolution of an anti-dark lump, shown is the initial condition, at $t = 0$ [panel (a)], and a snapshot, at $t = 100$ [panel (b)], as found in the framework of the CH-NLS equation. It is observed that, up to this time, the lump soliton propagates undistorted and the radiation emitted is practically non observable. Furthermore, in the bottom panels of Fig. 3.3, shown is the result of a collision between two identical dark lumps – one traveling to the left and

one to the right. In panel (c), we depict the initial condition ($t = 0$), and in panel (d) the outcome of the collision (at $t = 100$), where the leftmost lump appears at the rightmost place, and vice versa. It is seen that, for such small-amplitudes, the two lump solitons remain unscathed after the collision while, in this case too, no radiation is observable. We note in passing that the validity of our analytical approximations was also checked in other cases (not shown here), e.g., for individual anti-dark line solitons and dark lump solitons, as well as for collisions between such structures, and – for sufficiently small amplitudes – a very good agreement with the numerical results was found as well.

Next, we consider lumps of larger amplitudes. Figures 3.4 and 3.5 depict the evolution and collisions of anti-dark and dark lump solitons, respectively. Regarding their evolution (top panels of Figs. 3.4 and 3.5), it is observed that although both structures remain localized, they spread and bend radially, emitting also radial radiation. Indeed, as seen in the more pronounced case of the dark lump of Fig. 3.5, the emitted radiation has the form of nearly concentric circles. The collision between anti-dark or dark lumps (bottom panels of Figs. 3.4 and 3.5, respectively) appears to be elastic; nevertheless, post collision dynamics again features the formation of (nearly) concentric segments of circular rings, which appear to be more pronounced in the case of dark lumps.

We have also performed simulations to study collisions between line and lump solitons. Pertinent results are depicted in Fig. 3.6 for solitons of both types, dark (top panels) and anti-dark (bottom panels). In this case too, nearly elastic collision occurs in both cases, with the deformation of the lumps along the radial direction persisting as in the previously studied cases. We note in passing that collisions between line dark solitons and anti-dark lumps (and vice versa) are not possible because solitons of the dark and the anti-dark type and of different dimensionality do not coexist for the same parameter values; such collisions may become possible only in the presence of higher-order effects that may facilitate the coexistence of such structures (see, e.g., [94] where third-order dispersion supports

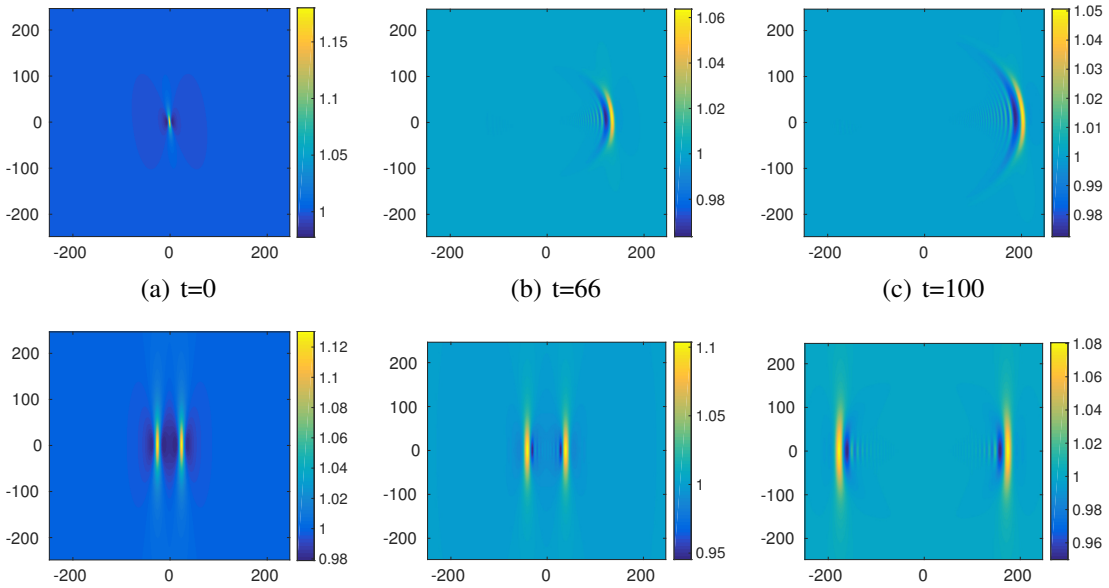

Figure 3.4: Large-amplitude anti-dark lump solitons. Top panels show the evolution of this waveform for $a = \frac{1}{2}$, $\epsilon = 0.01$, $\gamma = 1$, and $\beta = 3$; it is observed that this structure evolves into a bent shape. Bottom panels depict the collision between two identical anti-dark lumps, for $a = 0.6$, $\epsilon = 0.08$, $\gamma = 0$, and $\beta = \frac{1}{2}$; the collision appears to be almost elastic although radiation develops in each lump after it.

solitons of different types and different dimensionality, which can undergo quasi-elastic head-on collisions).

Lastly, we use generic Gaussian initial data on top of the background to investigate whether the resulting dynamics can share some qualitative features with the one corresponding to the approximate line and lump soliton solutions. To be exact, for the initial condition we place the Gaussian

$$u(x, y, 0) = 1 + A \exp\left[-\left(\frac{x}{\sigma_1 L_x}\right)^2 - \left(\frac{y}{\sigma_2 L_y}\right)^2 \right] \tag{3.35}$$

on top of the background, where $A = -0.2$, L_x, L_y are the bounds of the computational domain and σ_1, σ_2 control the length and width. We have fixed $L_x = L_y = 500$ and $\sigma_1 = 0.02$. Pertinent results are shown in Fig. 3.7, for a Gaussian very stretched in the

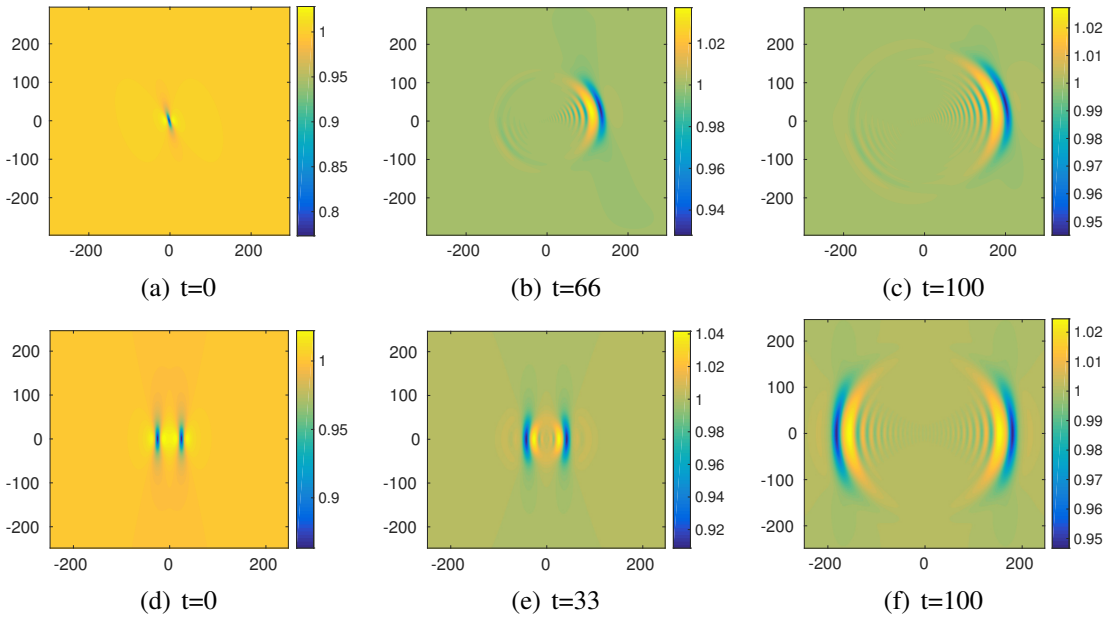

(a) t=0 (b) t=66 (c) t=100

(d) t=0 (e) t=33 (f) t=100

Figure 3.5: Similar to Fig. 3.4, but for large-amplitude dark lump solitons. The observed behavior is similar to that of the anti-dark lump case. For the top panels, the parameter values are $a = 1$, $\epsilon = 0.01$, $\gamma = 1$, and $\beta = 1.8$, while for the bottom panels $a = 1$, $\epsilon = 0.08$, $\gamma = 0$, and $\beta = \frac{1}{2}$.

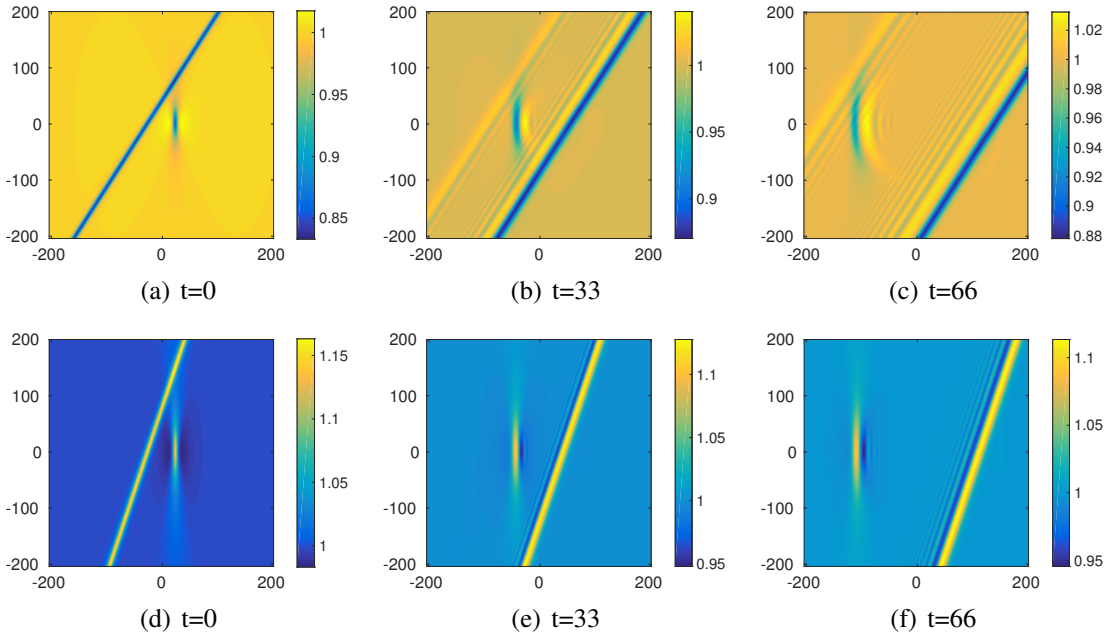

(a) t=0 (b) t=33 (c) t=66

(d) t=0 (e) t=33 (f) t=66

Figure 3.6: Top panels: collision between large-amplitude dark line and lump solitons; parameters used: $a = 1$, $\epsilon = 0.08$, $\gamma_{\text{Line}} = 1.5$, $\beta_{\text{Line}} = 1$, $\gamma_{\text{Lump}} = 0$, and $\beta_{\text{Lump}} = \frac{1}{2}$. Bottom panels: collisions between large-amplitude anti-dark line and lump solitons; parameters used: $a = 0.6$, $\epsilon = 0.08$, $\gamma_{\text{Line}} = 1.5$, $\beta_{\text{Line}} = 1$, $\gamma_{\text{Lump}} = 0$, and $\beta_{\text{Lump}} = \frac{1}{2}$.

vertical direction (top panels, $\sigma_2 = 0.8$), for a slightly stretched Gaussian (middle panels, $\sigma_2 = 0.07$), and for a completely symmetric Gaussian (bottom panels, $\sigma_2 = 0.02$).

It is observed that, in the first case, the extended Gaussian splits into two symmetric waveforms reminiscent of a pair of dark line solitons moving in opposite directions. Here, the initial stripe-like structure, is similar to a line dark soliton but without a phase jump [cf. Eq. (3.29)]. To attain the correct phase profile suggested by the energetically preferable approximate line dark soliton, and still preserve the phase structure at infinity, the initial Gaussian has to split to two oppositely moving stripes.

On the other hand, in the case where the initial condition has the form of a slightly extended Gaussian (cf. middle panels of Fig. 3.7), the form of the initial data is closer to that of a dark lump soliton (rather than that of a line soliton). In this case too, due to not having the proper phase structure –and decay at infinity which is now exponential rather than algebraic– the initial data reorganizes itself into a structure which is reminiscent to a superposition of two bent lumps. Here, one should observe the resemblance of this dynamics with the outcome of the collision between two dark lumps of Fig. 3.5. Finally, when the initial Gaussian is completely symmetric, the resulting structure evolves towards an almost perfect ring-like structure resembling an expanding ring soliton.

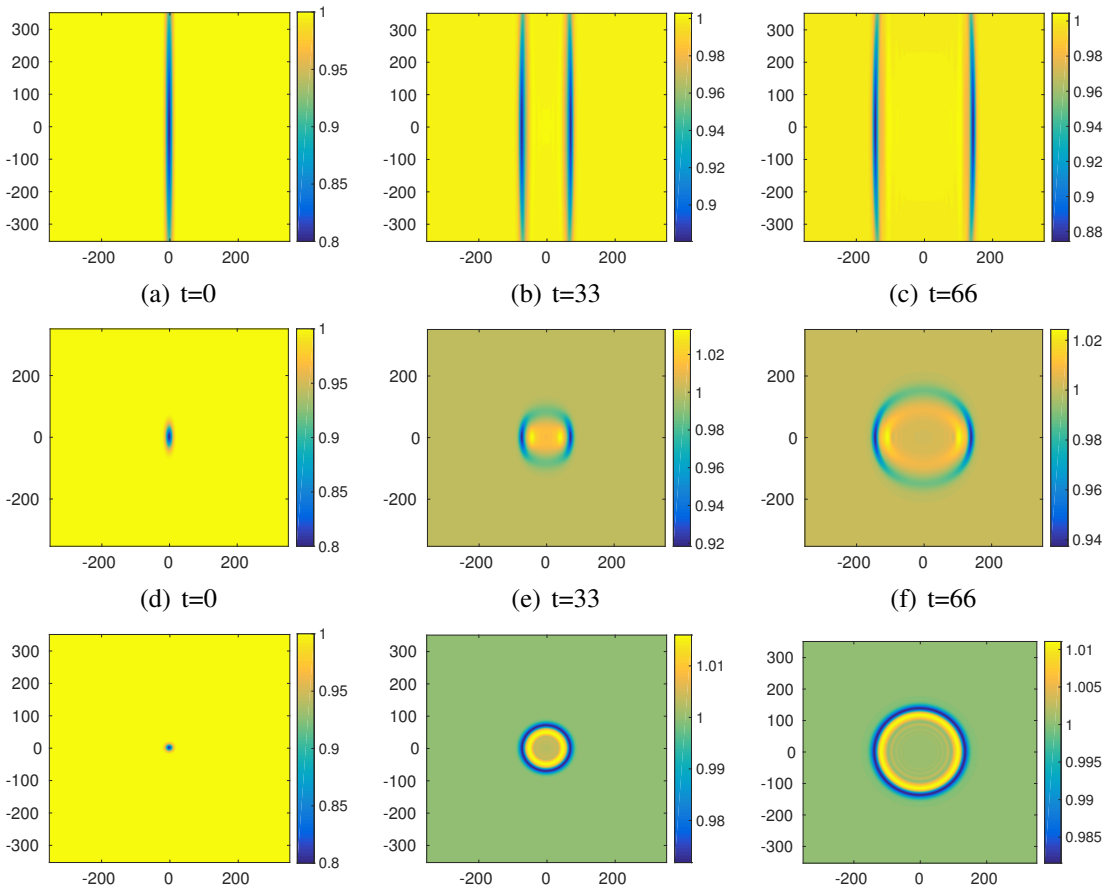

(a) t=0 (b) t=33 (c) t=66

(d) t=0 (e) t=33 (f) t=66

(g) t=0 (h) t=33 (i) t=66

Figure 3.7: Evolution of Gaussian-like pulses; the top panels depict the case of an extremely elongated (in the y-direction) such pulse, the middle panels show the case of a slightly elongated Gaussian, while the bottom panels depict the evolution of a completely symmetric such pulse. For detailed initial condition parameters, see the text.

CHAPTER 4

THE CAMASSA-HOLM DERIVATIVE NONLINEAR SCHRÖDINGER EQUATION

4.1 Model and Its stability

The CH-DNLS equation is given by

$$\hat{q}_t = iq_{xx} + 2((a^2|q_x|^2 - |q|^2)\hat{q})_x, \quad \hat{q} = q - a^2 q_{xx}, \quad a \in \mathbb{R}, \tag{4.1}$$

where $\hat{q}$ and q are complex functions with respect to variables x and t. When $a = 0$, this equation reduces to the DNLS equation. In terms of the complex filed q, the CH-DNLS equation can be read as

$$q_t - iq_{xx} + 2(|q|^2 q)_x - a^2 q_{xxt} - 2a^2(q|q_x|^2 - a^2|q_x|^2 q_{xx} + |q|^2 q_{xx})_x = 0. \tag{4.2}$$

It is obvious that the constant function $q = q_0$ solves Eq. (4.2). To study the linear stability of this constant solution, we perturb the CH-DNLS with the ansatz

$$\tilde{q} = q_0 + \epsilon p \tag{4.3}$$

where ϵ is a small parameter and $p(x,t)$ satisfies the following linearized (around the background q_0) equation

$$p_t - ip_{xx} - 2a^2 q_0^2 p_{xxx} - a^2 p_{xxt} + 2q_0^2(2p + p^*)_x = 0. \tag{4.4}$$

Looking for solutions of the form $p(x,t) = r(t)e^{i\kappa x} + s(t)e^{-i\kappa x}$, we can reduce the aforementioned linear PDE to the 2×2 system of ODE's $d\eta/dt = iM\eta$, where $\eta = [r, s^*]^T$ and

$$M = \frac{1}{1+a^2\kappa^2}\begin{pmatrix} -2\kappa^3 a^2 q_0^2 - 4\kappa q_0^2 - \kappa^2 & -2\kappa q_0^2 \\ -2\kappa q_0^2 & -2\kappa^3 a^2 q_0^2 - 4\kappa q_0^2 + \kappa^2 \end{pmatrix}. \tag{4.5}$$

The dynamics of $\eta(t)$ are therefore determined by the eigenvalues of this matrix, given by

$$\omega_{1,2} = \frac{(-2\kappa^2 a^2 q_0^2 - 4q_0^2 \pm \sqrt{4q_0^4 + \kappa^2})\kappa}{1+a^2\kappa^2}. \tag{4.6}$$

Given that the two roots are both real, the constant solution q_0 is always spectrally stable.

It's also worth noting that in the long-wavelength limit (i.e. as $\kappa \to 0$), the phase velocity ω/κ becomes

$$|c_1| = 2q_0^2, \quad \text{or} \quad |c_2| = 6q_0^2. \tag{4.7}$$

These correspond to the Alfvén (c_1) and magnetosonic (c_2) MHD velocities [21]. In the following, the MKdV equation can be derived from Eq. (4.1) by employing multiscale expansions around the velocity c_1, whereas the KdV equation can be derived by expanding around c_2.

4.2 Reductive derivation of MKdV equation from CH-DNLS equation

Let us introduce the well-known Madelung transformation (or amplitude-phase decomposition)

$$q = \rho \exp(i\phi), \quad \kappa(x,t) = \frac{\partial \phi}{\partial x}, \quad \omega(x,t) = -\frac{\partial \phi}{\partial t}, \tag{4.8}$$

where ρ and ϕ are real functions with respect to variables x and t. Substituting this into Eq. (4.2), the simplest nontrivial solution is the constant background q_0. To better underline the hydrodynamic origin of the soliton solutions presented below, we first derive a

real MKdV equation. We thus seek solutions of Eq. (4.2) in the form of the following asymptotic expansion

$$\rho = q_0 + \epsilon\rho_1(\xi,\tau) + \cdots, \quad \kappa = \epsilon\kappa_1(\xi,\tau) + \cdots, \tag{4.9}$$

where

$$\xi = \epsilon(x - ct), \quad \tau = \epsilon^3 t,$$

and $0 < \epsilon \ll 1$ is a formal small parameter.

Substituting Eqs. (4.8) and (4.9) into Eq.(4.2) and using the fact that

$$\frac{\partial\kappa}{\partial t} + \frac{\partial\omega}{\partial x} = 0,$$

we separate the resulting equation into real and imaginary parts to obtain, up to $O(\epsilon^4)$:

$$\begin{aligned} 0 = {} & \epsilon\big[0\big] + \epsilon^2\big[(6q_0^2 - c)\rho_{1\xi} + q_0\kappa_{1\xi}\big] + \epsilon^3\big[(-3a^2cq_0 + 2a^2q_0^3)\kappa_1\kappa_{1\xi} + (6q_0^2 - c)\rho_{2\xi} + \kappa_{1\xi}\rho_1 \\ & + 2\kappa_1\rho_{1\xi} + q_0\kappa_{2\xi} + 12q_0\rho_1\rho_{1\xi}\big] \\ & + O(\epsilon^4) \end{aligned} \tag{4.10}$$

$$\begin{aligned} 0 = {} & \epsilon\big[(2q_0^3 - cq_0)\kappa_{1\xi}\big] + \epsilon^2\big[(6q_0^2 - c)\kappa_{1\xi}\rho_1 + (6q_0^2 - c)\kappa_1\rho_{1\xi} + (2q_0^3 - cq_0)\kappa_{2\xi} + 2q_0\kappa_1\kappa_{1\xi}\big] \\ & + \epsilon^3\big[- 3a^2cq_0\kappa_1^2\kappa_{1\xi} + (a^2cq_0 - 2a^2q_0^3)\kappa_{1\xi\xi\xi} - c\kappa_{1\xi}\rho_2 - c\kappa_1\rho_{2\xi} + (2q_0\kappa_1 - c\rho_1)\kappa_{2\xi} \\ & + (2q_0\kappa_{1\xi} - c\rho_{1\xi})\kappa_2 + (2q_0^3 - cq_0)\kappa_{3\xi} + 6q_0\kappa_{1\xi}\rho_1^2 + 2\kappa_1\kappa_{1\xi}\rho_1 + 6q_0^2\kappa_{1\xi}\rho_2 + q_0\kappa_{1\tau} \\ & + 12q_0\kappa_1\rho_1\rho_{1\xi} + \kappa_1^2\rho_{1\xi} + 6q_0^2\kappa_1\rho_{2\xi} + 6q_0^2\kappa_{2\xi}\rho_1 + 6q_0^2\kappa_2\rho_{1\xi} - \rho_{1\xi\xi\xi}\big] \\ & + O(\epsilon^4). \end{aligned} \tag{4.11}$$

Notice that to $O(\epsilon)$ Eq. (4.11) is satisfied by

$$c = 2q_0^2, \tag{4.12}$$

as expected. Now, using this identity, Eqs. (4.10) and (4.11) to $O(\epsilon^2)$ are zero provided

$$\kappa_1 = -4q_0\rho_1. \tag{4.13}$$

Using the previous two equations, we see that Eq. (4.10) is satisfied at $O(\epsilon^3)$ provided

$$\kappa_2 = 32a^2q_0^4\rho_1^2 - 4q_0\rho_2 \tag{4.14}$$

Substituting Eqs. (4.12), (4.13), and (4.14) into Eq.(4.11), we see that it vanishes to $O(\epsilon^3)$ provided that ρ_1 satisfies the real MKdV equation

$$4q_0^2\rho_{1\tau} + \rho_{1\xi\xi\xi} + 24q_0^2\rho_1^2\rho_{1\xi} = 0. \tag{4.15}$$

Under the scaling transformation

$$\hat{\xi} = 2q_0\xi, \quad \hat{\tau} = 2q_0\tau, \tag{4.16}$$

Eq. (4.15) becomes a standard MKdV equation

$$\rho_{1\hat{\tau}} + \rho_{1\hat{\xi}\hat{\xi}\hat{\xi}} + 6\rho_1^2\rho_{1\hat{\xi}} = 0. \tag{4.17}$$

This equation is well-known to admit a soliton solution (see, e.g., [11, 95])

$$\rho_1 = b\,\mathrm{sech}[b(\hat{\xi} - \hat{\xi}_0) - b^3\hat{\tau}] \tag{4.18}$$

where arbitrary constants b and $\hat{\xi}_0$ determine the amplitude (and width and velocity) of the soliton. Returning to the original (x,t)-coordinates, we find the following approximate solution of the CH-DNLS equation, Eq.(4.2):

$$q \approx \Big[q_0 + \epsilon b\,\mathrm{sech}(\chi)\Big]\exp\Big[-2i\arctan(\sinh(\chi))\Big], \tag{4.19}$$

where

$$\chi = 2bq_0\epsilon(x - x_0) - (4bq_0^3\epsilon + 2b^3q_0\epsilon^3)t.$$

It's important to note that this perturbative solution describes two types of solitons: for $b > 0$, the soliton is anti-dark, corresponding to density humps on top of the constant background q_0, whereas for $b < 0$ the soliton is dark, corresponding to density dips on top of the constant background q_0.

It should also be noted that although κ has been found to $O(\epsilon)$ the phase itself is only given here to $O(1)$. The reason for this is that when returning to the x, t coordinates the ϵ's in the coordinate transformation cancel with the ϵ's in the expansion for the phase. This also occurs in the reduction of the DNLS equation to the MKdV equation.

4.3 Reductive Derivation of KdV Equation from CH-DNLS Equation

We now proceed to derive the KdV equation from Eq. (4.2) by using a multiscale expansion method around the velocity c_2. First, rewrite Eq. (4.2) as two real equations by using the ansatz

$$q = q_y + iq_z. \tag{4.20}$$

We then seek solutions in the form of the following asymptotic expansions:

$$\begin{aligned} q_y &= q_0 + \epsilon q_y^{(1)} + \epsilon^2 q_y^{(2)} + ... \\ q_z &= \epsilon^{3/2}(q_z^{(1)} + \epsilon q_z^{(2)} + ...) \\ \tau &= \epsilon^{3/2}t, \quad \xi = \sqrt{\epsilon}(x - ct) \end{aligned} \tag{4.21}$$

Substituting Eqs. (4.20)-(4.21) into Eq. (4.2), we obtain the following results:

$$
\begin{aligned}
0 &= \epsilon^{3/2}\big[(6q_0^2 - c)q_{y\xi}^{(1)}\big] \\
&\quad + \epsilon^{5/2}\big[q_{y\tau}^{(1)} + q_{z\xi\xi}^{(1)} + (ca^2 - 2a^2q_0^2)q_{y\xi\xi\xi}^{(1)} + 12q_0q_y^{(1)}q_{y\xi}^{(1)} + (6q_0^2 - c)q_{y\xi}^{(2)}\big] \\
&\quad + O(\epsilon^{7/2})
\end{aligned} \tag{4.22}
$$

$$
\begin{aligned}
0 &= \epsilon^{2}\big[(2q_0^2 - c)q_{z\xi}^{(1)} - q_{y\xi\xi}^{(1)}\big] \\
&\quad + O(\epsilon^{3})
\end{aligned} \tag{4.23}
$$

Eq. (4.22) to $O(\epsilon^{3/2})$ yields

$$
c = 6q_0^2. \tag{4.24}
$$

Similarly, Eq. (4.23) to $O(\epsilon^2)$ is satisfied by

$$
q_z^{(1)} = -\frac{1}{4q_0^2}\frac{\partial q_y^{(1)}}{\partial \xi}. \tag{4.25}
$$

Now, substituting Eqs. (4.24) and (4.25) into Eq. (4.22) at $O(\epsilon^{5/2})$ yields the following KdV equation for $q_y^{(1)}$

$$
\frac{\partial q_y^{(1)}}{\partial \tau} + 12q_0q_y^{(1)}\frac{\partial q_y^{(1)}}{\partial \xi} + (4a^2q_0^2 - \frac{1}{4q_0^2})\frac{\partial^3 q_y^{(1)}}{\partial \xi^3} = 0. \tag{4.26}
$$

To proceed further, and express the KdV equation (4.26) in its standard form, we introduce the straightforward rescaling:

$$
\tilde{\tau} = \frac{16a^2q_0^4 - 1}{4q_0^2}\tau, \quad q_y^{(1)} = -\frac{16a^2q_0^4 - 1}{8q_0^3}\tilde{q}_y^{(1)}. \tag{4.27}
$$

Then Eq. (4.26) is reduced to

$$
\frac{\partial \tilde{q}_y^{(1)}}{\partial \tilde{\tau}} - 6\tilde{q}_y^{(1)}\frac{\partial \tilde{q}_y^{(1)}}{\partial \xi} + \frac{\partial^3 \tilde{q}_y^{(1)}}{\partial \xi^3} = 0. \tag{4.28}
$$

The above equation possesses the commonly known (see, e.g., Ref. [11, 95]) soliton solution

$$\tilde{q}_y^{(1)} = -\frac{\lambda}{2}\,\mathrm{sech}^2[\frac{\sqrt{\lambda}}{2}(\xi - \lambda\tilde{\tau} + \xi_0)], \tag{4.29}$$

with arbitrary constants $\lambda > 0$ and ξ_0. Using this exact solution and returning to the original variables, we have that the perturbative approximation of Eq. (4.2) is given by

$$\begin{aligned} q &= q_y + iq_z, \\ q_y &\approx q_0 - \epsilon\frac{\lambda a_2}{2}\,\mathrm{sech}^2(\chi), \\ q_z &\approx -\epsilon^{3/2}\frac{\lambda^{3/2}a_2}{8q_0^2}\mathrm{sech}^2(\chi)\tanh(\chi), \end{aligned} \tag{4.30}$$

where parameters χ, a_1, and a_2 are defined as

$$\chi = \frac{\sqrt{\lambda\epsilon}}{2}[(x - x_0) - (6q_0^2 + a_1\lambda\epsilon)t], \tag{4.31}$$

$$a_1 = \frac{16a^2q_0^4 - 1}{4q_0^2}, \quad a_2 = -\frac{16a^2q_0^4 - 1}{8q_0^3}. \tag{4.32}$$

We see that this soliton can be either dark if $a_2 > 0$ or antidark if $a_2 < 0$. It is relevant to discuss here an interesting distinction between the MKdV and KdV reduction results. In the former, the potential dark or antidark nature of the solitonic structures depends on the choice of the parameter b controlling the (arbitrary) amplitude, width, and velocity of the wave. On the other hand, this type of freedom does *not* exist in the KdV reduction whereby the nature of the wave is controlled by the height of the background q_0 and the CH-deformation model parameter a.

4.4 Numerically Obtained Solutions

In this section we corroborate our analytical predictions by numerically integrating Eq. (4.1) using suitable initial and boundary conditions. Our aim is to confirm the existence of the previously identified asymptotic solutions and to explore these solutions at

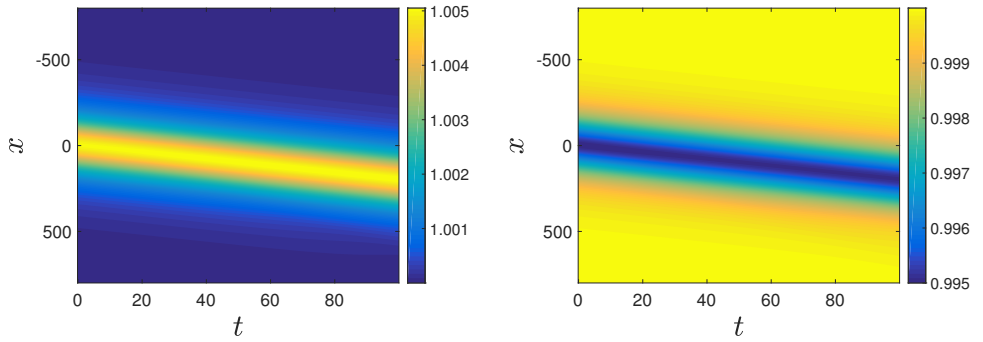

(a) Antidark MKdV Soliton

(b) Dark MKdV Soliton

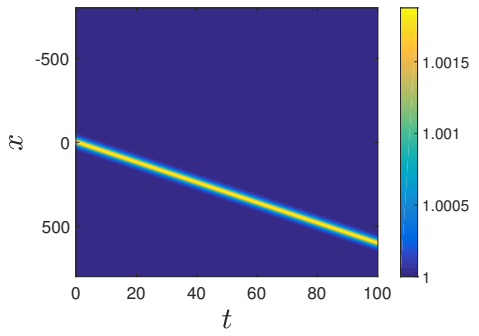

(c) Antidark KdV Soliton

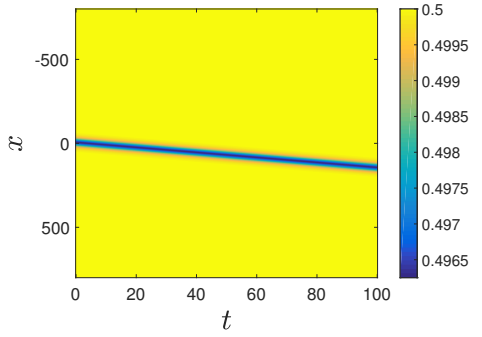

(d) Dark KdV Soliton

Figure 4.1: Small Amplitude Solitons. Note that the speed of the KdV and MKdV solitons are nearly identitical to what the asympototic expansion predicts. Parameter values used: (a) $\epsilon = 0.005$, $a = 0.5$, $b = -1$, $q_0 = 1$ (b) $\epsilon = 0.005$, $a = 0.5$, $b = 1$, $q_0 = 1$ (c) $\epsilon = 0.01$, $a = 0.5$, $\lambda = 1$, $q_0 = 1$ (d) $\epsilon = 0.01$, $a = 0.5$, $\lambda = 1$, $q_0 = 0.5$.

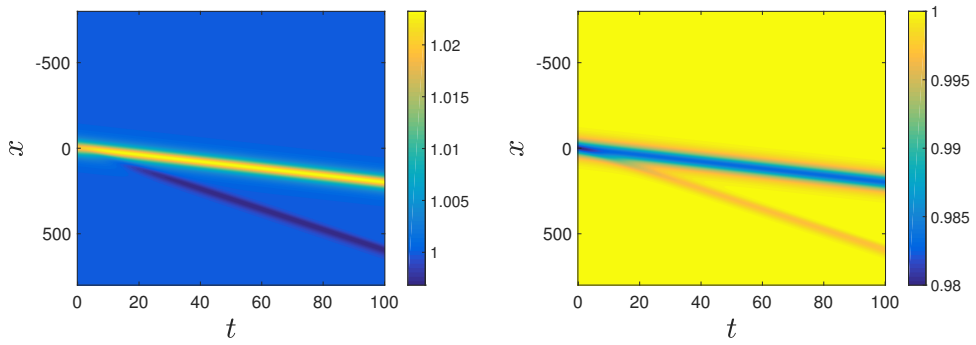

(a) Antidark MKdV Soliton

(b) Dark MKdV Soliton

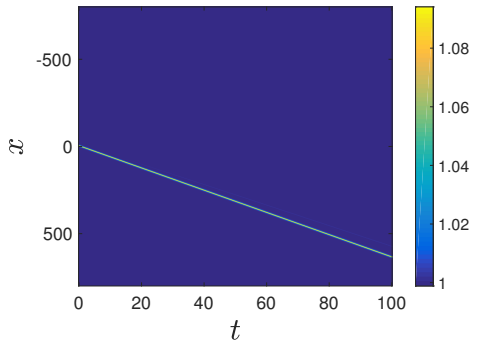

(c) Antidark KdV Soliton

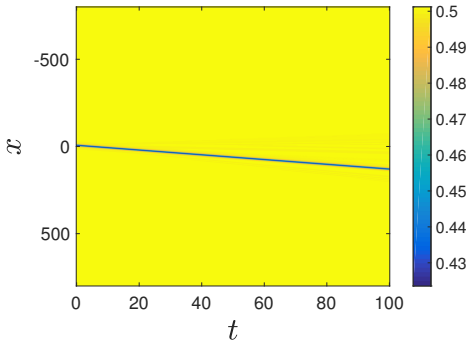

(d) Dark KdV Soliton

Figure 4.2: Large Amplitude Solitons. We see a similar qualitative behavior as in the small amplitude case, except now with some small radiation (as the solution initially "adapts"). Parameter values used: (a) $\epsilon = 0.02$, $a = 1$, $b = -1$, $q_0 = 1$ (b) $\epsilon = 0.02$, $a = 1$, $b = 1$, $q_0 = 1$ (c) $\epsilon = 0.5$, $a = 0.5$, $\lambda = 1$, $q_0 = 1$ (d) $\epsilon = 0.2$, $a = 0.5$, $\lambda = 1$, $q_0 = 0.5$.

large amplitude (i.e., in the regime where the asymptotic reduction leading to their identification should not be expected to be valid).

Fig. 4.1 corresponds to the case of small amplitudes while Figs. 4.2 and 4.3 correspond to large amplitudes. In order to be more precise, let us note that for the initial condition of the KdV soliton, we set t equal to zero in Eqs. (4.30). We then used the ansatz

$$q_i(x) := \Big(q(x,0) - q_0\Big) \exp\left[- \left(\frac{x}{L^*}\right)^{12}\right] + q_0 \tag{4.33}$$

as the initial condition, where $q(x,0)$ is as given in Eqs. (4.30). Here L^* is set to 0.8 times the length of the (spatial) computational domain. This ensures that the the initial condition q_i is, to numerical precision, equal to q_0 at the boundaries, allowing for the use of periodic boundary conditions. Further, L^* is chosen large enough so that the boundaries do not effect the interior dynamics during the time interval of the simulation. In a similar vein, for the MKdV solutions, we set t equal to zero in Eqs. (4.19), and then use the ansatz

$$q_i(x) := \Big(q(x,0) + q_0\Big) \exp\left[- \left(\frac{x}{L^*}\right)^{12}\right] - q_0 \tag{4.34}$$

as the initial condition. Due to the nature of the phase factor in Eq. (4.19), the MKdV solitons asymptote to $-q_0$ for large values of x, t; hence, the ansatz Eq. (4.34) makes sure the value at the boundaries is indeed $-q_0$.

For collisions between the solitons, as an initial condition we simply multiplied the two previously defined initial conditions (i.e. the two ansatz corresponding to Eqs. (4.33) and (4.34)); we've set the background $q_0 = 1$ for the KdV soliton and -1 one for the MKdV soliton, ensuring that they have the same value at far-field. We should mention, however, that we treat the ϵ's appearing in each ansatz as independent parameters; that is to say, we set ϵ appearing in the KdV soliton to some value ϵ_{KdV} and set ϵ appearing in the MKdV solitons to some other value ϵ_{MKdV}. Finally, because the dark and antidark MKdV solitons have approximately identical speed, we did not consider collisions between

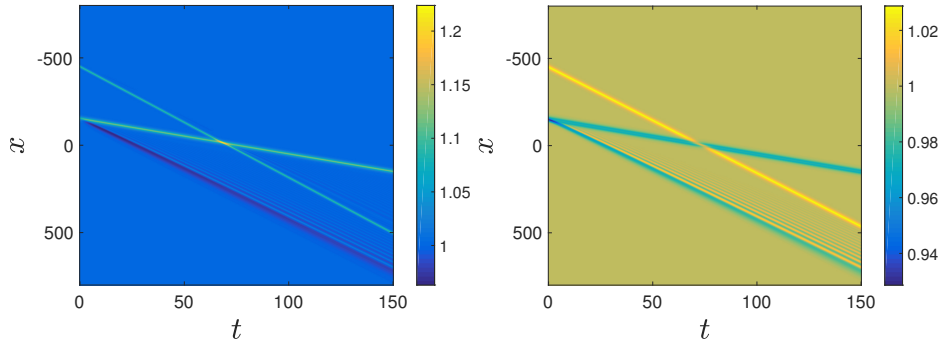

(a) Antidark KdV/Antidark MKdV Soliton (b) Antidark KdV/Dark MKdV Soliton

Figure 4.3: Large Amplitude Collisions. (a) $\epsilon_{\text{KdV}} = 0.1$, $\lambda = 1$, $\epsilon_{\text{MKdV}} = 0.07$, $b = -1$, $a = 1$, $q_0 = 1$ (b) $\epsilon_{\text{KdV}} = 0.03$, $\lambda = 1$, $\epsilon_{\text{MKdV}} = 0.07$, $b = 1$, $a = 1$, $q_0 = 1$. We can see that the antidark KdV-antidark MKdV, as well as the antidark KdV-dark MKdV collisions are nearly elastic for the considered parameters and initial conditions.

the two, as they might require an extremely long interval of time integration for such an overtaking collision. Collisions between dark and antidark KdV solitons are not included either because the two types of solitons are not predicted to exist for the same value of the deformation parameter a.

For the small amplitude time-integrations appearing in Fig. 4.1 we see that the numerics and the theory are in very good agreement. In particular, notice that the predicted speed of the KdV solitons $6q_0^2 = 6$, $6q_0^2 = 1.5$ in panels (c),(d) and that of the MKdV solitons $2q_0^2 = 2$ in panels (a), (b) are seen to be almost identical to that given by the simulation. Moreover, the coherent structures propagate essentially undistorted with these speeds, as predicted by the reductive perturbation theory.

Fig. 4.2 shows the results of the large amplitude initial conditions. As before, these are in good qualitative agreement with what the perturbation analysis suggests. It's worth pointing out that the ejected soliton appearing in Fig. 4.2 (a),(b) is seen to not only have a speed of approximately 6 but it is also a *dark* soliton, in contrast to our antidark KdV solitons which travel at the same speed.

Fig. 4.3 shows the results of colliding the antidark KdV and MKdV solitons. As can be seen, the solitons appear to collide nearly elastically, though radiation can clearly be seen

to be created at the collision point in Fig. 4.3. This is especially visible in the left panel illustrating the collision of an antidark soliton of the KdV with one of the MKdV. Although in this case too, the most substantial radiation arises from the "adjustment" of the initial condition.

CHAPTER 5

A TOOLKIT FOR STEADY STATES OF NONLINEAR WAVE EQUATIONS: CONTINUOUS TIME NESTEROV AND EXPONENTIAL TIME DIFFERENCING SCHEMES

5.1 Earlier Methods for Calculating Ground States

In this section we discuss two among the most widely used, previously developed methods, AITEM [96] and the Spectral Renormalization method [97], for identifying ground states of the steady state problem within the NLS equation.

5.1.1 AITEM

Eq. (1.2) can be recast in the variational form

$$\min_{\psi} \int |\nabla\psi|^2 + V(x)|\psi|^2 - \frac{\sigma}{2}|\psi|^4 \, dx \qquad \text{subject to} \qquad \int |\psi|^2 \, dx = P, \quad (5.1)$$

where the first integral is the field-theoretic energy $E(\psi)$ of the system and the second integral fixes the number of particles (in the atomic case) or the power –hence the symbol– in the optical case to be P [1].

[1] It is worth noting that while in the analysis below we explore the cubic nonlinearity for concreteness, our considerations are, in principle, expected to apply equally well to more general nonlinearities.

Using a Lagrange multiplier, we can directly incorporate the relevant constraint. The resulting gradient flow is then given by

$$\dot{\psi} = \nabla^2\psi - V(x)\psi + \sigma|\psi|^2\psi + \mu\psi. \tag{5.2}$$

In tradional variational problems, P is typically known and μ unknown i.e. the constraint is a given but the Lagrange multiplier must be identified. In this case, we can let $\mu = \mu(t)$ be a function of time such that $\mu(t)$ converges to the true value of the Lagrange multiplier as $t \to \infty$. One such choice of $\mu(t)$ was given by Yang and Lakoba [96] as

$$\mu(t) = -\frac{\langle L\psi, \psi\rangle}{\langle \psi, \psi\rangle} \tag{5.3}$$

where the inner products represent the standard L^2 inner product and $L\psi = \nabla^2\psi - V(x)\psi + \sigma|\psi|^2\psi$; if one thinks of μ as an eigenvalue then this is the standard Rayleigh quotient. Because $\psi = 0$ is always a solution of the NLS, one must still include the constraint $\int |\psi|^2 \, dx = P$ to ensure the evolution does not go to the trivial solution. If one applies, say, the standard Euler method to (5.2) and also adds a preconditioner M, then one gets the AITEM scheme:

$$\begin{aligned} M &= c - \nabla^2 \\ \mu_n &= -\frac{\langle M^{-1}L\psi_n, \psi_n\rangle}{\langle M^{-1}\psi_n, \psi_n\rangle} \\ \tilde{\psi}_{n+1} &= \psi_n + M^{-1}(L\psi_n + \mu_n\psi_n)\Delta t \\ \psi_{n+1} &= \tilde{\psi}_{n+1}\sqrt{\frac{P}{\langle \tilde{\psi}_{n+1}, \tilde{\psi}_{n+1}\rangle}}. \end{aligned} \tag{5.4}$$

The fourth equation ensures that the number of particles (the constraint $\int |\psi|^2 \, dx = P$) is satisfied after each iteration. We remark that the parameter c is a positive number which must be chosen a priori.

5.1.2 Spectral Renormalization

An alternative method applicable to the NLS for general nonlinearity N is the so-called spectral renormalization method [97], addressing problems of the form:

$$\nabla^2\psi - V(x)\psi + N(|\psi|^2)\psi + \mu\psi = 0$$

Unlike before, here we think of μ as a fixed constant. If we take the Fourier transform (denoted by $\mathcal{F}$) of this equation we obtain

$$-|\mathbf{k}|^2\hat{\psi} + \mathcal{F}[-V(x)\psi + N(|\psi|^2)\psi] + \mu\hat{\psi} = 0$$

and solving for $\hat{\psi}$ yields

$$\hat{\psi} = \frac{\mathcal{F}[-V(x)\psi + N(|\psi|^2)\psi]}{|\mathbf{k}|^2 - \mu}$$

Thinking of this as a fixed point iteration method

$$\hat{\psi}_{n+1} = \frac{\mathcal{F}[-V(x)\psi_n + N(|\psi_n|^2)\psi_n]}{|\mathbf{k}|^2 - \mu}$$

we might expect this to converge to a ground state. However numerical experiments have shown that it tends to converge to zero or diverge without bound.

To get around this problem, Ablowitz and Musslimani [97] suggested that one should include a renormalization factor λ, which is determined by the iteration procedure itself. Letting $\psi = \lambda\phi$, $\hat{\psi} = \lambda\hat{\phi}$, plugging these into the NLS equation, and repeating gives

$$\hat{\phi} = \frac{\mathcal{F}[-V(x)\phi + N(|\lambda\phi|^2)\phi]}{|\mathbf{k}|^2 - \mu}$$

If we now multiply the previous equation by $\hat{\phi}$ and integrate we get an algebraic condition on λ:

$$\langle\hat{\phi}, \hat{\phi}\rangle - \langle\hat{\phi}, \frac{\mathcal{F}[-V(x)\phi + N(|\lambda\phi|^2)\phi]}{|\mathbf{k}|^2 - \mu}\rangle = 0$$

Since λ is just a scalar, we see that it is determined by the above equation. We then have the scheme:

$$0 = \langle \hat{\phi}_n, \hat{\phi}_n \rangle - \langle \hat{\phi}_n, \frac{\mathcal{F}[-V(x)\phi_n + N(|\lambda_n \phi_n|^2)\phi_n]}{|\mathbf{k}|^2 - \mu} \rangle$$
$$\hat{\phi}_{n+1} = \frac{\mathcal{F}[-V(x)\phi_n + N(|\lambda_n \phi_n|^2)\phi_n]}{|\mathbf{k}|^2 - \mu}$$

One drawback of the scheme as written is that if μ is not negative then the iteration leads to division by zero. In [97], it was thus suggested that the term $r\psi$ be added and subtracted to the NLS equation; if one then repeats the argument, a scheme where division by zero does not occur can be devised. This scheme, the Spectral Renormalization method, is given by

$$0 = \langle \hat{\phi}_n, \hat{\phi}_n \rangle - \langle \hat{\phi}_n, \frac{(r+\mu)\hat{\phi}_n}{r + |\mathbf{k}|^2} + \frac{\mathcal{F}[-V(x)\phi_n + N(|\lambda_n \phi_n|^2)\phi_n]}{r + |\mathbf{k}|^2} \rangle$$
$$\hat{\phi}_{n+1} = \frac{(r+\mu)\hat{\phi}_n}{r + |\mathbf{k}|^2} + \frac{\mathcal{F}[-V(x)\phi_n + N(|\lambda_n \phi_n|^2)\phi_n]}{r + |\mathbf{k}|^2}. \tag{5.5}$$

where r is some positive parameter which must be chosen before the iteration begins.

Finally, we mention in passing that a generalization of this method [98], the so-called Time-Dependent Spectral Renormalization Method, has recently been developed to treat time-integration in dispersive PDE as a fixed point problem.

5.2 Proposed Twists

In this section we propose a number of modifications and extensions of AITEM and Spectral Renormalization.

5.2.1 Exponential Time Differencing

The first of these new methods is simply a different way of time-stepping the gradient flow equation. Namely, using the first-order exponential time differencing scheme [89, 90] instead of Euler's method.

More specifically, consider Eq. (5.2) again. By taking the Fourier transform of both sides we arrive at

$$\hat{\psi}_t = -|\mathbf{k}|^2\hat{\psi} + \mathcal{F}[-V(x)\psi + \sigma|\psi|^2\psi] + \mu\hat{\psi}$$

Applying the first order exponential time differencing scheme to this equation we get

$$\hat{\psi}_{n+1} = e^{-|\mathbf{k}|^2 h}\hat{\psi}_n + \frac{e^{-|\mathbf{k}|^2 h} - 1}{-|\mathbf{k}|^2}[\mathcal{F}[-V(x)\psi_n + \sigma|\psi_n|^2\psi_n] + \mu\hat{\psi}_n]$$

However, some care is needed in dealing with the term $\frac{e^{-|\mathbf{k}|^2 h}-1}{-|\mathbf{k}|^2}$ so that division by zero and catastrophic cancellation do not occur. We refer the reader to the insightful work of Kassam and Treffethen [90] in which they propose to use the Cauchy integral formula to calculate this expression and include a Matlab code for implementing this at the end.

Now, we have to impose the constraint $\int |\psi|^2 dx = P$. We proceed in a similar fashion as AITEM:

$$\begin{aligned}
\mu_n &= -\frac{\langle L\hat{\psi}_n, \hat{\psi}_n\rangle}{\langle \hat{\psi}_n, \hat{\psi}_n\rangle} \\
\tilde{\hat{\psi}}_{n+1} &= e^{-|\mathbf{k}|^2 h}\hat{\psi}_n + \frac{e^{-|\mathbf{k}|^2 h} - 1}{-|\mathbf{k}|^2}[\mathcal{F}[-V(x)\psi_n + \sigma|\psi_n|^2\psi_n] + \mu_n\hat{\psi}_n] \qquad (5.6) \\
\hat{\psi}_{n+1} &= \tilde{\hat{\psi}}_{n+1}\sqrt{\frac{P}{\langle \tilde{\hat{\psi}}_{n+1}, \tilde{\hat{\psi}}_{n+1}\rangle}}
\end{aligned}$$

where $L\hat{\psi} = -|\mathbf{k}|^2\hat{\psi} + \mathcal{F}[-V(x)\psi + \sigma|\psi|^2\psi]$ and $h = \Delta t$, the proposed effective time step. We will refer to this scheme as ETD for the remainder of the chapter. Our main motivation for proposing this scheme is that it does not need a preconditioner like that in AITEM; in some sense, Duhamel's formula itself –incorporating the integration of the

Laplacian term– is a preconditioner. We also expect that if the potential stiffness is due to the Laplacian term, then this method should perform quite well.

If the stiffness is instead concentrated in the term $V(x)\psi$ then we expect ETD and AITEM to do far more poorly. In such a case, we propose that $V(x)\psi$ should be considered the linear part and not $\nabla^2\psi$. Before proceeding, we remark that if one does exponential time differencing in physical space then it is difficult to compute the operator $e^{\nabla^2 h}$. Moreover, in Fourier space it is difficult to separate $\hat{\psi}$ in $\mathcal{F}[V(x)\psi]$ from the potential; what this implies computationally is that one must choose between letting the Laplacian *or* the potential to be included in the linear part.

Now, staying in physical space and performing exponential time differencing based on the potential gives

$$\begin{aligned} \mu_n &= -\frac{\langle L\psi_n, \psi_n\rangle}{\langle \psi_n, \psi_n\rangle} \\ \tilde{\psi}_{n+1} &= e^{-V(x)h}\psi_n + \frac{e^{-V(x)h}-1}{-V(x)}[\nabla^2\psi_n + \sigma|\psi_n|^2\psi_n + \mu_n\psi_n] \\ \psi_{n+1} &= \tilde{\psi}_{n+1}\sqrt{\frac{P}{\langle \tilde{\psi}_{n+1}, \tilde{\psi}_{n+1}\rangle}} \end{aligned} \tag{5.7}$$

where, again, the term $\frac{e^{-V(x)h}-1}{-V(x)}$ must be interpreted appropriately. We will refer to this scheme as ETDV.

5.2.2 Continuous Time Nesterov

Consider the variational problem of minimizing the function $F(x)$; here we are considering F to be a function and not a functional. To solve this problem, one method is of course to use gradient descent. However, if F is sufficiently "ill-behaved" we do not expect that gradient descent will converge easily. As an alternative, Su, Boyd, and Candes [50] were able to formulate a second order ODE which in some sense generalizes gradient descent:

$$\ddot{x} + \frac{3}{t}\dot{x} + \nabla F(x) = 0$$

As discussed in their paper, this ODE is actually a continuous version of Nesterov's (discrete) mirror descent [49]. Henceforth, we will refer to this scheme as continuous time Nesterov (CTN).

Two major differences occur between CTN and gradient descent. The first, and crucial one (since it will also enable the second as we will see), is that CTN is a second order ODE. Roughly speaking, this means that the acceleration vector, and NOT the velocity vector, points in the direction that the field is decreasing fastest (at least for large t). This is similar to a particle moving in the force field of a potential i.e. a related way of envisioning this ODE is to say that the particle has been given mass and has a time-dependent dissipation on which we now comment. The second major difference is the dissipation term $\frac{3}{t}\dot{x}$; thinking of a particle in a potential, we see that this term has the effect of damping the energy/momentum. However, this damping is tuned to be large at the initial time, when presumably the particle is far from the equilibrium while it decreases the closer that one (hopefully) gets to the relevant fixed point. This term is, thus, responsible for the actual convergence of the method to minima of F. With too little damping the method will only oscillate around the minima but with too much damping the method could be terribly inefficient.

In the work of [50], the authors suggest using a second-order center difference scheme for approximating the second derivative and a first order backward difference scheme for approximating the first derivative. Doing this and rearranging the dynamical evolution equation gives the scheme

$$x_{n+1} = (2 - \frac{3}{n})x_n - (\Delta t)^2 \nabla F(x_n) - (1 - \frac{3}{n})x_{n-1}$$

where we have let $t = n\Delta t$.

We remark in passing that, as was proven in [49], this scheme enjoys linear convergence, provided F is strongly convex.

5.2.3 Accelerated Continuous Time Nesterov

A principal contribution of the present work is to propose and illustrate the relevance of applying CTN not just to functions but to (field-theoretic) functionals; as far as we know, this application of CTN as a means of finding steady state solutions of a PDE has not been previously considered.

Returning to the variational problem (5.1), we see that CTN takes the form

$$\ddot{\psi} + \frac{3}{t}\dot{\psi} - (\nabla^2\psi - V(x)\psi + \sigma|\psi|^2\psi + \mu\psi) = 0$$

where we have included the Lagrange multiplier μ, and abused the overdot notation in this field-theoretic context to signify partial derivative with respect to t. Discretizing this as before, we arrive at

$$\psi_{n+1} = (2 - \frac{3}{n})\psi_n + (\Delta t)^2(\nabla^2\psi - V(x)\psi + \sigma|\psi|^2\psi + \mu\psi) - (1 - \frac{3}{n})\psi_{n-1}.$$

Since the dissipation term controls the convergence properties to a high degree, both in the work of [50] and in that of [99], much effort has been invested in trying to optimize it. In particular, it is proposed to reset time t at appropriate points in the evolution so that CTN is always sufficiently damped; again, when t is small there is a large amount of damping. Such a variant is the gradient restarting scheme, whereby time is reset to one when the angle between $-\nabla F(x)$ and $\dot{x}$ is greater than 90 degrees AND a prespecified amount of time t_{res} has elapsed:

$$\langle \nabla F(x), \dot{x} \rangle > 0$$
$$t \geq t_{res}.$$

If we include gradient restarting into the above descritization we get

$$\psi_{n+1} = (2 - \frac{3}{\tilde{n}})\psi_n + (\Delta t)^2(\nabla^2\psi_n - V(x)\psi_n + \sigma|\psi_n|^2\psi_n + \mu\psi_n) - (1 - \frac{3}{\tilde{n}})\psi_{n-1},$$

where $\tilde{n}$ starts at one and increases by one after each iteration; once the restart condition

$$\langle \nabla^2\psi_n - V(x)\psi_n + \sigma|\psi_n|^2\psi_n + \mu\psi_n \ \ , \ \ \psi_{n+1} - \psi_n\rangle > 0$$
$$n \geq n_{res} \tag{5.8}$$

is met, $\tilde{n}$ is reset to one and the process repeats.

If we include a preconditioner M and recall that we must normalize after each iteration, then the full method can be written as

$$\begin{aligned}
M &= c - \nabla^2 \\
\mu_n &= -\frac{\langle L\psi_n, \psi_n\rangle}{\langle \psi_n, \psi_n\rangle} \\
\tilde{\psi}_{n+1} &= (2 - \frac{3}{\tilde{n}})\psi_n + (\Delta t)^2 M^{-1}(\nabla^2\psi_n - V(x)\psi_n \\
&\quad + \sigma|\psi_n|^2\psi_n + \mu_n\psi_n) - (1 - \frac{3}{\tilde{n}})\psi_{n-1} \\
\psi_{n+1} &= \tilde{\psi}_{n+1}\sqrt{\frac{P}{\langle \tilde{\psi}_{n+1}, \tilde{\psi}_{n+1}\rangle}}
\end{aligned} \tag{5.9}$$

where, again, $\tilde{n}$ is chosen via gradient restarting. We shall refer to this scheme as Accelerated Continuous Time Nesterov (ACTN), in the fashion of AITEM.

We remark that the convergence rate of this method is unknown to us. While CTN was proven to converge linearly under strong convexity, no convergence proof is known to us of CTN with gradient restarting (though Su, Boyd, and Candes prove something similar). With the inclusion of the preconditioner and particle number normalization, it is not clear what convergence speed should be expected. To that end, the numerical experiments below suggest the ACTN will, generically, converge linearly.

Lastly, we note that if we fix μ in the NLS equation then AITEM, ACTN, and ETD can all be renormalized via a straightforward procedure that we present in the Section 5.4. We denote these as Renormalized AITEM (AITEMRe), Renormalized ACTN (ACTNRe),

and Renormalized ETD (ETDRe). We also mention that, in principle, this procedure can be done for more general constraints.

5.3 Computational Results

We now present the results of the realization of the proposed methods for fundamental as well as excited steady states of the one- and two-dimensional NLS equation with different types of trapping potentials. Each example has a comparison with AITEM and Spectral Renormalization to give a reference point.

5.3.1 Ground States in 1D

Unless otherwise mentioned, we take the spatial domain to be $[-12, 12]$. For all methods except ETDV, spatial descritization is done in Fourier space via the Discrete Fourier Transform (DFT) with 128 points. ETDV is discretized in physical space using finite differences with 128 points. The initial condition used for all examples is $\psi_0 = Ae^{-x^2}$, where A was chosen so that the power is five.

We also want to emphasize that we are computing AITEM, AITEMRe, ACTN, and ACTNRE in Fourier space. To be precise, we first take the DFT of the given equation (gradient descent or CTN) and then we apply the given iteration procedure to this equation. Doing it this way, the cost of one iteration of each of AITEM and ACTN involves only one FFT and one IFFT; it also makes the computation of M^{-1} very cheap. The renormalized methods will cost slightly more depending on the equation. For example, the scheme (5.12), see Section 5.4, will cost two FFT's and one IFFT per iteration.

Fig. 5.1 and 5.2 show the results of applying the methods to the cubic NLS equation

$$\nabla^2\psi - V(x)\psi + \sigma|\psi|^2\psi + \mu\psi = 0;$$

each example corresponds to a different $V(x)$ and σ. Notice that examples are shown both for the focusing case of $\sigma = 1$ and for the defocusing one of $\sigma = -1$. The diagrams on the

left constitute plots of the log of the L^2 norm of the difference between ψ_{n+1} and ψ_n versus the number of iterations. We stopped all runs once the *residual* error reached 10^{-10}. The diagrams on the right show the various parameter values we used for each method as well as the total number of iterations; if a method didn't reach the prescribed tolerance, then it is labeled "DNC" for did not converge. To be precise, we do not claim that the method can not converge but rather, for the various parameter values we tried, we were not able to observe convergence. We also want to emphasize that although we tried to choose the parameters so that all schemes perform at their "best", and although our results represent the principal trend for the parameter sets examined, we cannot guarantee that these comparisons will be valid for all possible parameter sets. Lastly, ETDV performs so poorly in some examples compared to the other methods that we do not always include it in the error diagrams; its total number of iterations can still be found in the relevant tables.

The general behavior shown in Fig. 5.1 is that the continuous Nesterov methods tend to outperform the others, although AITEMRe clearly converges much quicker than the other methods in Fig. 5.1(g). It's also clear that the continuous Nesterov methods tend to converge quickest in the quartic potentials; this isn't surprising as CTN was devised to outperform gradient descent in poorly conditioned problems. Regardless, even for the parabolic and periodic potentials where the iteration counts are much lower, ACTN and ACTNRe still seem to have an advantage.

ETD and ETDRe seem to perform as well as the AITEM and AITEMRe. Based only on these examples, it is not clear to us that there is a systematic advantage in using one method over the other. However, as we stated above, our interest in exponential time differencing is that it is an alternative way of performing the time-stepping.

Fig. 5.2, in particular, shows the possible value of schemes such as ETDV, as it is the only method which converges. Overall, once again, ETD methods simply offer an efficient, alternative method of performing the time integration step.

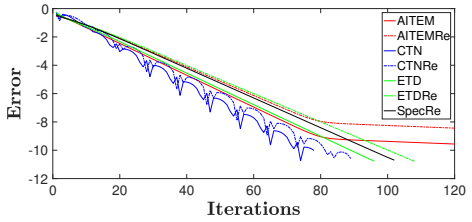

(a) $V(x) = 0.1x^2$, $\sigma = -1$

Scheme	Δt	c	$\tilde{n}$	r	Iterations
AITEM	.55	3	-	-	251
AITEMRe	.55	3	-	-	370
ACTN	.85	3	9	-	78
ACTNRe	.85	3	9	-	89
ETD	.16	-	-	-	96
ETDRe	.16	-	-	-	108
SpecRe	-	-	-	5.7	102
ETDV	.017	-	-	-	960

(b) $\mu = 1.1848$

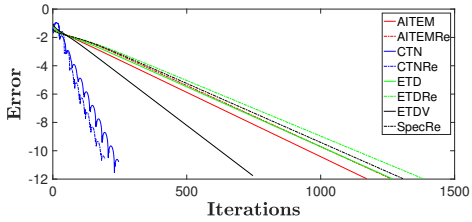

(c) $V(x) = 0.01x^4 + 0.02x^2$, $\sigma = -1$

Scheme	Δt	c	$\tilde{n}$	r	Iterations
AITEM	.052	4	-	-	1172
AITEMRe	.14	12	-	-	1260
ACTN	.3	5	23	-	246
ACTNRe	.35	6	20	-	194
ETD	.01	-	-	-	1270
ETDRe	.01	-	-	-	1385
SpecRe	-	-	-	94	1307
ETDV	.017	-	-	-	747

(d) $\mu = 1.0393$

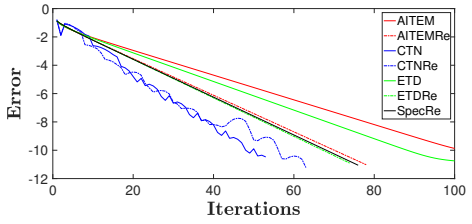

(e) $V(x) = 0.1x^2$, $\sigma = 1$

Scheme	Δt	c	$\tilde{n}$	r	Iterations
AITEM	.85	6	-	-	252
AITEMRe	.83	6	-	-	78
ACTN	.9	4	23	-	53
ACTNRe	.9	4	20	-	63
ETD	.13	-	-	-	112
ETDRe	.12	-	-	-	74
SpecRe	-	-	-	7.5	76
ETDV	.017	-	-	-	695

(f) $\mu = -1.5955$

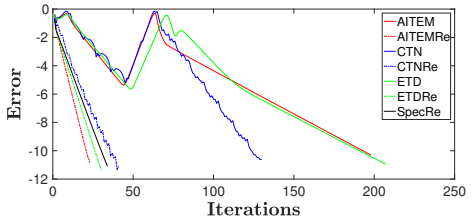

(g) $V(x) = \cos(x)$, $\sigma = 1$

Scheme	Δt	c	$\tilde{n}$	r	Iterations
AITEM	1.2	2	-	-	198
AITEMRe	1.4	3	-	-	23
ACTN	1.2	3	9	-	130
ACTNRe	1.1	4	4	-	41
ETD	.47	-	-	-	207
ETDRe	.4	-	-	-	30
SpecRe	-	-	-	2	34
ETDV	.016	-	-	-	3371

(h) $\mu = -2.6069$

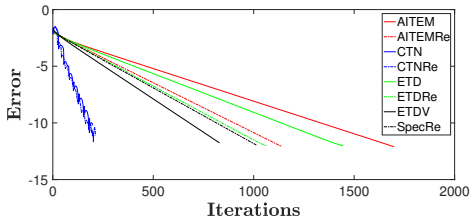

(i) $V(x) = 0.01x^4 + 0.02x^2$, $\sigma = 1$

Scheme	Δt	c	$\tilde{n}$	r	Iterations
AITEM	.08	7	-	-	1700
AITEMRe	.09	8	-	-	1140
ACTN	.3	5	26	-	199
ACTNRe	.32	5	20	-	212
ETD	.01	-	-	-	1445
ETDRe	.4	-	-	-	1062
SpecRe	-	-	-	96	1017
ETDV	.017	-	-	-	830

(j) $\mu = -1.5795$

Figure 5.1: Evolution of the error, defined as the L^2 norm of the difference between successive iterates, as a function of the iteration index for different potentials $V(x)$, when seeking the ground state of the 1D NLS equation. The right set of tables indicates the values of the parameters selected and the corresponding number of iterations needed to reach the prescribed tolerance of 10^{-10}.

There also does not appear to be any particular trend between the performance of a scheme and of its renormalized version; either one can outperform the other. That being said, Fig. 5.1(g) is particularly interesting. All of the renormalized methods converge to an unstable state centered at the origin –where the initial guess was also centered–. Nevertheless, the other methods converge to the stable, ground state, centered around $x = \pi$ i.e. around the minimum of the potential. Interestingly, notice how this "shift" takes place: while initially the method attempts to extremize by maintaining the waveform centered at the maximum, eventually, it cannot decrease the error below a certain threshold, being forced to seek a lower energy state by shifting the center of the coherent structure around $x = \pi$ (see the relevant trend after the 50th iteration), eventually decreasing the error in this new location below the desired tolerance.

The case reported in Fig. 5.2 bears some similarities to the above described scenario, as once again the state is initialized as located at the center, yet the double well nature of the potential does not favor such a localization at the maximum. Instead, the lowest energy state consists of a concentration of the atoms (or the optical power) in either the left or right well of the relevant potential. This symmetry-breaking is a feature well-known in the context of double-well potentials [15]. The ETDV attempts for a while to extremize the free energy via localization at the center. Eventually, being unsuccessful, it is led to shift the wave mass to one of the two sides converging to the state shown in panel (g) of Fig. 5.3. This figure contains the ground state identified in all the cases of Figs. 5.1-5.2, rendering transparent that in case (d) and (g), the localization happens around $x \neq 0$.

5.3.2 Ground States in 2D

In this section we focus on the 2D variant of the NLS equation, once again attempting to identify the ground state of the nonlinear elliptic problem. Fig. 5.4(a,b,c) is a defocusing NLS equation with quadratic potential. For the initial condition we use $\psi_0 = Ae^{-(x^2+y^2)}$, where A is chosen so that the resulting power is $P = 17$. Here, the ground single-hump

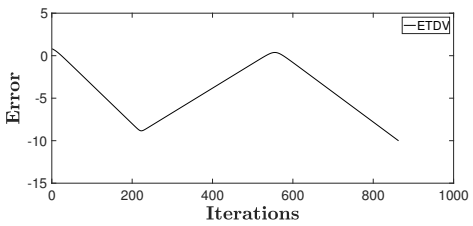

(a) $V = 10x^4 - 20x^2$, $\sigma = 1$

Scheme	Δt	c	$\tilde{n}$	r	Iterations
AITEM	-	-	-	-	DNC
AITEMRe	-	-	-	-	DNC
ACTN	-	-	-	-	DNC
ACTNRe	-	-	-	-	DNC
ETD	-	-	-	-	DNC
ETDRe	-	-	-	-	DNC
SpecRe	-	-	-	-	DNC
ETDV	.016	-	-	-	863

(b)

Figure 5.2: Similar to Fig. 5.1, but now for a double well potential. Only the ETDV is able to converge to the asymmetric ground state of this potential.

state (whose linear limit is proportional to the initial guess) is rapidly converged upon. Fig. 5.4(d,e,f) is a focusing NLS equation with periodic potential and we use a similar initial condition except A was chosen so that the chemical potential is $\mu = 3.7$. In this case, all the schemes converge in a comparable number of iterations to a gap soliton solution of the problem.

As in the 1D case, the same general trends tend to hold. The continuous Nesterov methods seem to outperform the others, the ITEM schemes and ETD schemes seem to not have significant differences in their performance, and again there does not seem to be definitive preferentiability manifested between renormalized methods and their standard version.

5.3.3 Excited States in 1D

Naturally, it is of substantial interest to go beyond the most fundamental states and seek excited states in the system. E.g. both in the atomic [15, 41–43] and in the optical problem [17], excited states such as dark solitons and multi-solitons in 1D and vortices and related structures (such as ring or planar dark solitons) in higher dimensions have been of particular interest.

In this section we combine ACTN with the so-called Squared Operator Method (SOM) [100] in order to capture such excited states. We quickly recap the basic idea: consider the gradient flow applied to some function F

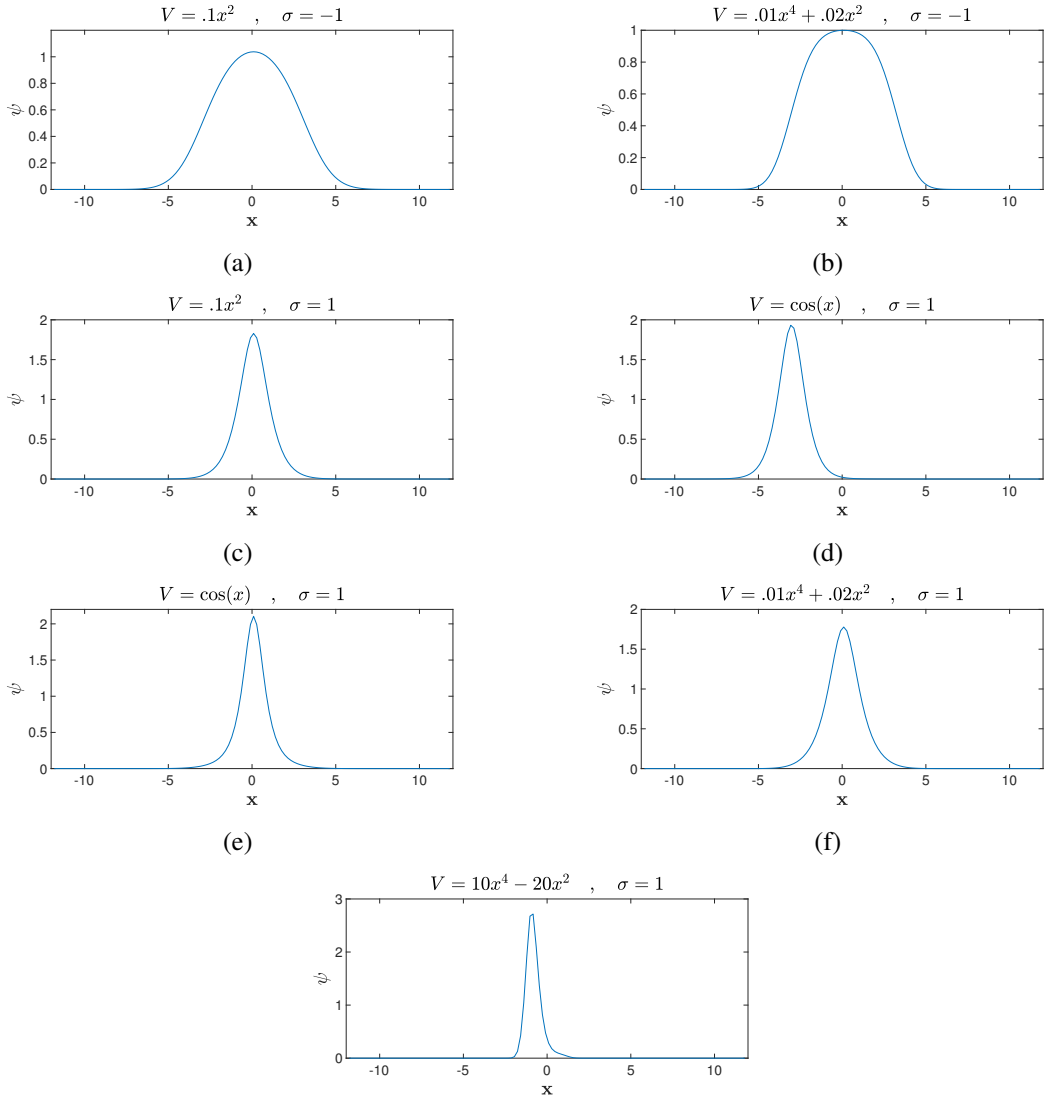

Figure 5.3: Corresponding steady states of the potentials analyzed in the previous two figures. Notice the $x \neq 0$ centering of cases (d) and (g).

$$\dot{u} = -F(u).$$

Naturally, this will only converge to local minima (in the case that F is the gradient of some function) or, more generally, to a steady state having only eigenvalues with negative real part (if F is not the gradient of some function). To extend this method to other steady states, one can instead consider the system

$$\dot{u} = -DF(u)F(u).$$

One quickly sees that this is just the derivative of $\frac{1}{2}|F(x)|^2$ (assuming DF is symmetric). Hence, the SOM converges to every steady state of F provided the initial condition is sufficiently close. Using CTN instead of the gradient flow, we get

$$\ddot{u} + \frac{3}{t}\dot{u} + DF(u)F(u) = 0.$$

It is this equation that we will study in what follows, and to which we will refer to as Squared (Operator) Continuous Time Nesterov (SCTN).

As an initial test, we seek families of stationary states of

$$\nabla^2\psi - 0.1x^2\psi - \psi^3 + \mu\psi = 0$$

i.e., tackling the defocusing problem with a parabolic trap, in the spirit of earlier works such as [101, 102]. We apply the ACTN method to the SCTN equation, resulting in the iteration

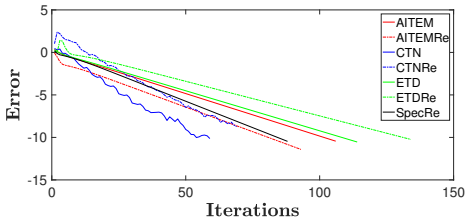

(a)

Scheme	Δt	c	$\tilde{n}$	r	Iterations
AITEM	1	3	-	-	106
AITEMRe	1.7	4	-	-	93
ACTN	1.1	2	5	-	59
ACTNRe	1.1	2	7	-	69
ETD	.3	-	-	-	114
ETDRe	.3	-	-	-	134
SpecRe	-	-	-	2.1	88

(b)

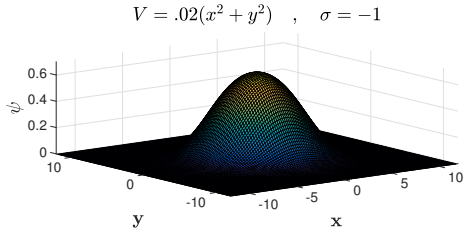

(c)

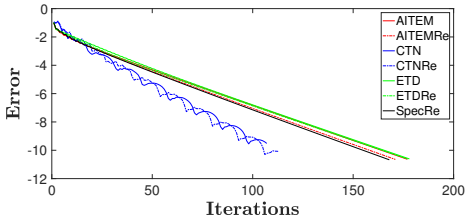

(d)

Scheme	Δt	c	$\tilde{n}$	r	Iterations
AITEM	1.1	3	-	-	177
AITEMRe	1.1	3	-	-	171
ACTN	1	2	5	-	107
ACTNRe	1	2	7	-	113
ETD	.31	-	-	-	178
ETDRe	.3	-	-	-	177
SpecRe	-	-	-	2.5	168

(e)

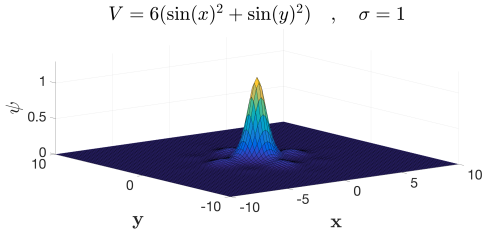

(f)

Figure 5.4: Two prototypical case examples in 2D. The top set of panels (a)-(c) displays the evolution of the error over the number of iterations, the parameters (and convergence iteration number) of the different methods, and the profile of the resulting solution for a parabolic trap in a defocusing 2D NLS with a Gaussian initial guess. Panels (d)-(f) report in similar format but now for a focusing 2D NLS with a periodic potential.

$$
\begin{aligned}
M &= (c-\nabla^2)^2 \\
\mu_n &= -\frac{\langle L\psi_n, \psi_n\rangle}{\langle \psi_n, \psi_n\rangle} \\
\tilde{\psi}_{n+1} &= (2-\frac{3}{\tilde{n}})\psi_n - (\Delta t)^2 M^{-1}(\nabla^2 - V(x) - 3\psi_n^2 + \mu_n)(\nabla^2\psi_n - V(x)\psi_n - \psi_n^3 + \mu_n\psi_n) \\
&\quad -(1-\frac{3}{\tilde{n}})\psi_{n-1} \qquad (5.10) \\
\psi_{n+1} &= \tilde{\psi}_{n+1}\sqrt{\frac{P}{\langle \tilde{\psi}_{n+1}, \tilde{\psi}_{n+1}\rangle}}
\end{aligned}
$$

which we will refer to as ASCTN.

Fig. 5.5(a) is the aforementioned bifurcation diagram (in a format similar to that of [102]), shown here with five branches. For each branch, we started the continuation near $P = 0$ and used a combination of Gaussians as our initial guess; knowledge of the corresponding linear Schrödinger equation's eigenfunctions would also work well, as is done in the next subsection. Once the method converges, we increase the value of P by $\Delta P = 0.3$ and then use the previous state as the new initial condition (in the spirit of parametric continuation). Fig. 5.5(b) shows the number of iterations necessary to go from one point on a branch to the next point on the branch (as a function of P); aside from branch 3, we see that it generally takes between 150 to 300 iterations to converge.

We also want to mention that we performed ASCTN in Fourier space as well (similar to ACTN). Because of this, the action of the jacobian is relatively cheap to calculate and so one doesn't need to store any large matrices. On the other hand, if one were doing finite differences/elements, one could instead use [103] the approximation

$$
\begin{aligned}
DF(u)F(u) &= \frac{d}{d\epsilon}\Big[F(u+\epsilon F(u)\Big]\Big|_{\epsilon=0} \\
&\approx \frac{F(u+\epsilon F(u)) - F(u)}{\epsilon}
\end{aligned}
$$

which again eliminates the need to form the Jacobian. This significantly decreases the cost of the relevant numerical computation.

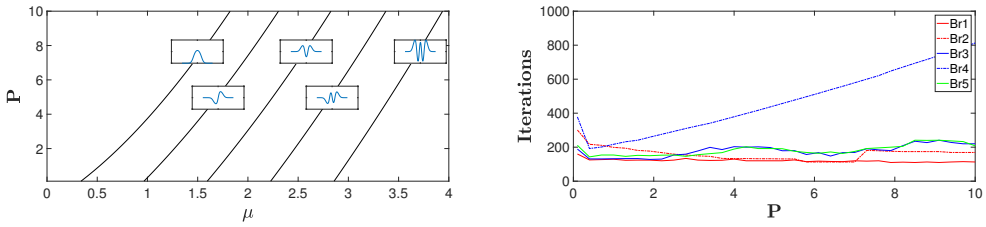

(a) (b)

Figure 5.5: Left panel: The bifurcation diagram of the first five excited states of the defocusing 1D NLS with parabolic trap. Right panel: Number of iterations needed to go from each point on the relevant branch to the next.

5.3.4 Excited States in 2D

Finally, we briefly wish to test the effectiveness of the ASCTN method in the 2D realm. Following the recent work of [104], we study the NLS equation

$$\frac{1}{2}\nabla^2\psi - 0.02(x^2+y^2)\psi - |\psi|^2\psi + \mu\psi = 0$$

In the limit as $P \to 0$, the nonlinearity becomes irrelevant and the stationary states bifurcate out of the linear limit. These linear eigenfunctions can be represented in the form [105]

$$|m,n\rangle := \psi_{m,n} = CH_m(\sqrt{0.2}x)H_m(\sqrt{0.2}y)e^{-0.1(x^2+y^2)}$$

where C is some constant, m, n are nonnegative integers, and H_m is the m-the Hermite polynomial. We note that the corresponding value of the linear eigenvalue μ of the corresponding states parametrized by the quantum numbers m and n is given by

$$\mu_{m,n} = 0.2(m+n+1).$$

Using these as an initial guess, we construct a partial bifurcation diagram starting at the μ values $0.2, 0.4, 0.6$. After ASCTN converged, we then increased P by $\Delta P = 0.5$. Fig. 5.6(a) shows the corresponding bifurcation diagram and Fig. 5.6(b) shows the iteration

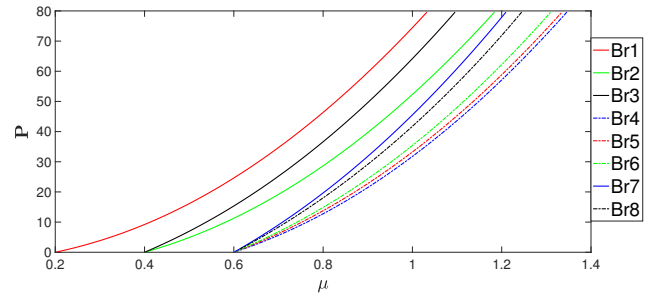

(a)

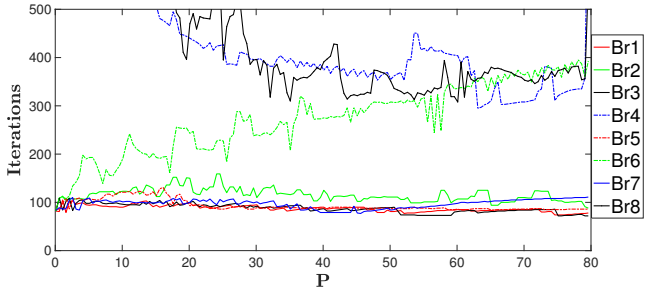

(b)

Figure 5.6: Panel (a) illustrates the different branches identified in the two-dimensional bifurcation diagram of the elliptic NLS problem with the parabolic trap. The bottom panel shows the number of iterations needed for the ASCTN scheme to converge from one solution (member of a branch) to the next (member of the branch).

count. There are eight branches in total. Fig. 5.7 shows plots of a selected point within each branch, as well as the relationship between the branch and the eigenstates of the associated linear limit; considerably more detail on the latter subject has been provided recently in [104], so we don't focus on the latter topic further here.

To go from one point on a branch to the next, Fig. 5.6(b) shows that it took around 100 iterations for five of the eight branches. Branches 2, 4, and 8 on the other hand consistently converged at a far higher iteration count. Branches 4 and 8 in particular took several thousand iterations to initially converge, but then settled down to around 350 for higher P values. It's not clear to us why some of these converged quickly while others converged slowly. The only thing worth mentioning is that some of these branch solutions become unstable (with respect to time in the time-dependent NLS) already for small values of μ and

progressively more so as μ increases. We do want to remark however that we did not try to adaptively choose the parameters; in fact, we used the same parameter values to continue all of the branches.

Returning to ASCTN itself, we need to mention two details. The first is that since some of these solutions are complex both the steady state equation and the Jacobian as written in Eq. (5.10) are not accurate (the 1D equations had only real solutions). Some care needs to be taken to find the derivative of the nonlinear term as it is not holomorphic i.e. $\frac{d}{d\psi}[|\psi^2|\psi]$ does not exist. Instead one could split the equation itself into real and imaginary parts and then try to apply the method to a vector equation. However, we found it easier to just calculate the (real) derivative of the nonlinear term and then plug it back into (5.10). Namely, letting $\psi = \psi_1 + i\psi_2$ and $H = H_1 + iH_2$, we have the directional derivative

$$d(|\psi|^2\psi)H = \Big[(2\psi_1^2 + |\psi|^2)H_1 + 2\psi_1\psi_2 H_2\Big] + i\Big[2\psi_1\psi_2 H_1 + (2\psi_2^2 + |\psi|^2)H_2\Big]$$

where instead of writing it as a two-component vector we identified it with a complex number.

The second is that gradient restarting only applies to real functions i.e. $\langle \nabla F(\psi), \dot{\psi} \rangle > 0$ only makes sense for real inputs. One way around this problem is to identify the given complex functions with real vector functions (under the natural identification) and then apply gradient restarting to the latter. However, recalling the identity $|u||v|\cos\theta = Re(\langle u, v \rangle)$ in a complex inner product space, we propose the equivalent restarting scheme

$$Re(\langle \nabla F(\psi), \dot{\psi} \rangle) > 0 \tag{5.11}$$

which works for complex functions and reduces to the former scheme when the functions are real.

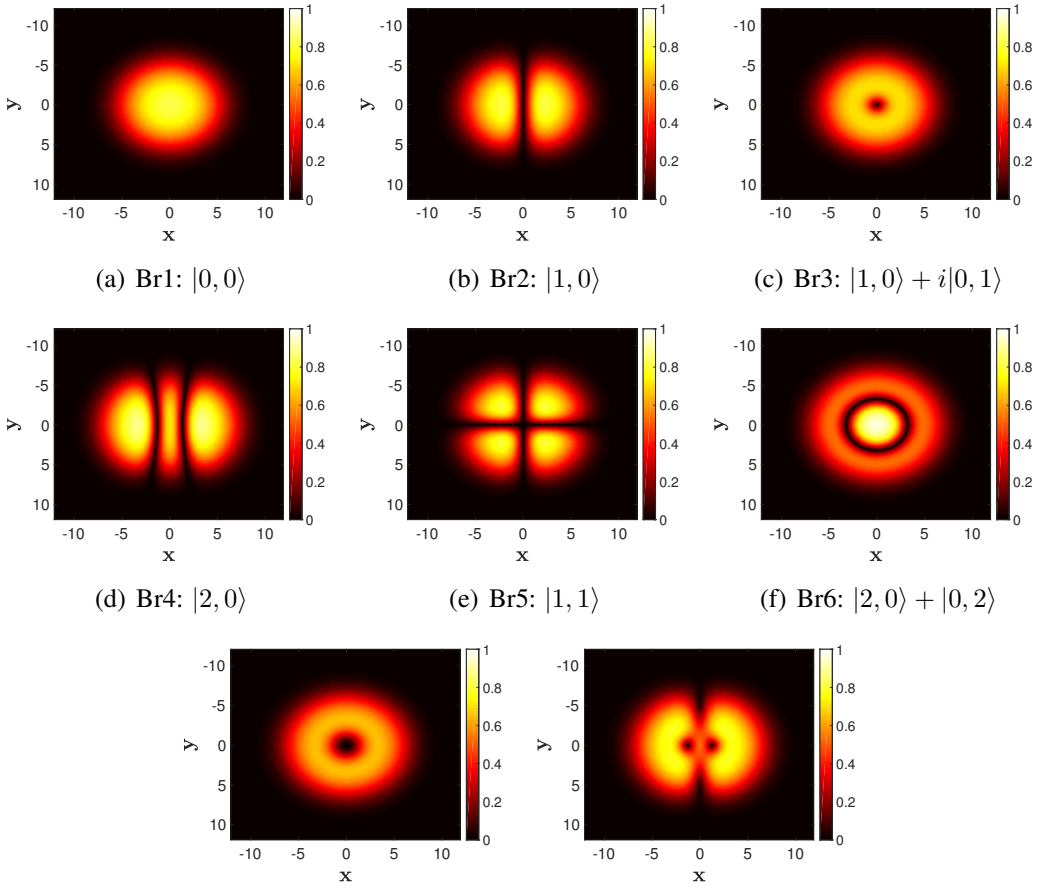

(a) Br1: $|0,0\rangle$ (b) Br2: $|1,0\rangle$ (c) Br3: $|1,0\rangle + i|0,1\rangle$

(d) Br4: $|2,0\rangle$ (e) Br5: $|1,1\rangle$ (f) Br6: $|2,0\rangle + |0,2\rangle$

(g) Br7: $|2,0\rangle - |0,2\rangle + 2i|1,1\rangle$ (h) Br8: $|2,0\rangle + i|1,1\rangle$

Figure 5.7: Typical examples of the different branches of solutions, not only the ground state one (Br1), but also excited ones such as the planar dark soliton (Br2), the single charge vortex (Br3) and so on that one can converge to using the SCTN method.

5.4 Implementation Details

5.4.1 Renormalized Methods

Inspired by Spectral Renormalization, we show in this section how to renormalize any iterative procedure. Suppose

$$x_{n+1} = F(x_n)$$

is some iteration method and

$$P = \int |x_n|^2$$

is a constraint. One way to "enforce" this constraint when P is unknown, is to introduce a renormalization constant λ by letting

$$x = \lambda w$$

If we assume x is the true fixed point, then plugging this into the iteration we get

$$\lambda w = F(\lambda w)$$

We then have that λ solves the algebraic equation

$$0 = \int w^*(\lambda w) - \int w^* F(\lambda w)$$

Now, define

$$g(\lambda_n, w_n) = \int w_n^*(\lambda_n w_n) - \int w_n^* F(\lambda_n w_n)$$

Then we perform the new iteration

$$0 = g(\lambda_n, w_n)$$

$$w_{n+1} = \frac{1}{\lambda_n} F(\lambda_n w_n)$$

where λ_n is found by solving the first equation.

For concreteness, we show AITEMRe applied to the NLS equation with cubic nonlinearity:

$$
\begin{aligned}
M &= c - \nabla^2 \\
\lambda_n^2 &= -\frac{\int \phi_n^*(\nabla^2\phi_n - V(x)\phi_n + \mu\phi_n)}{\int \phi_n^*(\sigma|\phi_n|^2\phi_n)} \\
\phi_{n+1} &= \phi_n - M^{-1}(\nabla^2\phi_n - V(x)\phi_n + \sigma|\lambda_n\phi_n|^2\phi_n + \mu\phi_n)\Delta t
\end{aligned} \tag{5.12}
$$

where we have used the relationship $\psi_n = \lambda_n\phi_n$.

5.4.2 Matlab Code

The following is a Matlab code for ACTN applied to the 2D NLS equation

$\nabla^2\psi - V(x)\psi + \sigma|\psi|^2\psi + \mu\psi = 0.$

```
%DEFINE VARIABLES AND PARAMETERS
L=12; m=2^7; sig=-1; dx=2*L/(m); x=(-L:dx:L-dx)'; [Xg,Yg]=ndgrid(x,x);
k=[0:m/2-1 -m/2:-1]'; k=(pi/L).*k; [xi, eta]= ndgrid(k,k);
Lap=-xi.^2-eta.^2; V= @(x,y) .02*(x.^2 + y.^2); Vx=V(Xg,Yg);
%INITIAL NORMALIZATION
XInt=@(x,y) exp(-x.^2 - y.^2); Xi=XInt(Xg,Yg); N=17;
Xi=Xi*(N/(sum(sum((conj(Xi).*Xi)))*dx^2))^(1/2);
%INITIALIZE ITERATE
X=Xi; X0hat=fftn(X); X1hat=X0hat; FXhat=fftn(-Vx.*X + sig*(abs(X).^2).*X
    );
%ITERATION PARAMETERS
dt=1; c=2; Restart=5;
ITER=1000; tol=10^-10;
jj=0; ii=0; i=0; e=1;

while e>tol && i < ITER
    i=i+1; ii=ii+1; jj=jj+1;
    %CALCULATE MU
    mu=-sum(sum(conj(Lap.*X1hat + FXhat).*(((1./(c-Lap)).*X1hat))))/...
        sum(sum(conj(X1hat).*(((1./(c-Lap)).*X1hat))));
    mu=real(mu);
    %ITERATION
    X2hat= (2-3/ii).*X1hat + dt^2*((1./(c-Lap))).*...
        (Lap.*X1hat + FXhat + mu*X1hat) - (1-3/ii)*X0hat;
```

```
24      X2=ifftn(X2hat);
25      %NORMALIZATION
26      amp=(N/(sum(sum((conj(X2).*X2)))*dx^2))^(1/2);
27      X2=X2*amp; X2hat=X2hat*amp;
28      %GRADIENT RESTART
29      if   sum(sum((Lap.*X1hat + FXhat + mu*X1hat).*...
30                conj(X2hat -X1hat)))> 0 && ii> Restart
31           ii=1;
32      end
33      %RESIDUAL ERROR
34      FXhat=fftn(-Vx.*X2 + sig*(abs(X2).^2).*X2);
35      e=sqrt((dx^2)/(m^2)*sum(sum((FXhat+mu*X2hat + Lap.*X2hat).*...
36       conj(FXhat+mu*X2hat + Lap.*X2hat))));
37      X0hat=X1hat; X1hat=X2hat;
38  end
39
40  surf(Xg,Yg,X2)
```

CHAPTER 6

EVALUATING THE ROBUSTNESS OF ROGUE WAVES UNDER PERTURBATIONS

6.1 Benchmarks & Results

Motivated partly by recent explorations at the interface of rogue waves and potentially collapsing dynamics [106] (involving power law nonlinearities) as well as by the relevance of perturbative terms (such as third order dispersion (TOD) [77] in optics), we take as our prototypical model example a two-parameter variation of the NLS:

$$i\frac{\partial\psi}{\partial t} + \frac{1}{2}\frac{\partial^2\psi}{\partial x^2} + |\psi|^{2p}\psi - i\epsilon\frac{\partial^3\psi}{\partial x^3} = 0. \tag{6.1}$$

Nevertheless, we should highlight that our computational analysis is by no means constrained to this particular choice. Indeed, it is expected to be of relevance to a wide range of previously treated variants of the NLS model.

A relevant point to recall is the modulational instability inherent in the background of the PS. As a result of this, finding rogue waves either through time-integration methods (which are not particularly well-suited anyway, given that for arbitrary variants of NLS, it is not clear what initial data to use to obtain a PS) or through fixed point iteration has been, in our experience, especially difficult. In that light, we have used a highly-efficient method, namely a variant of the Newton-conjugate gradient method of [107], originally designed for solitons on a zero background.

For the NLS equation, our benchmark studies show that the above Newton-CG method converges not only to a good approximation of the PS but also to other families of rogue

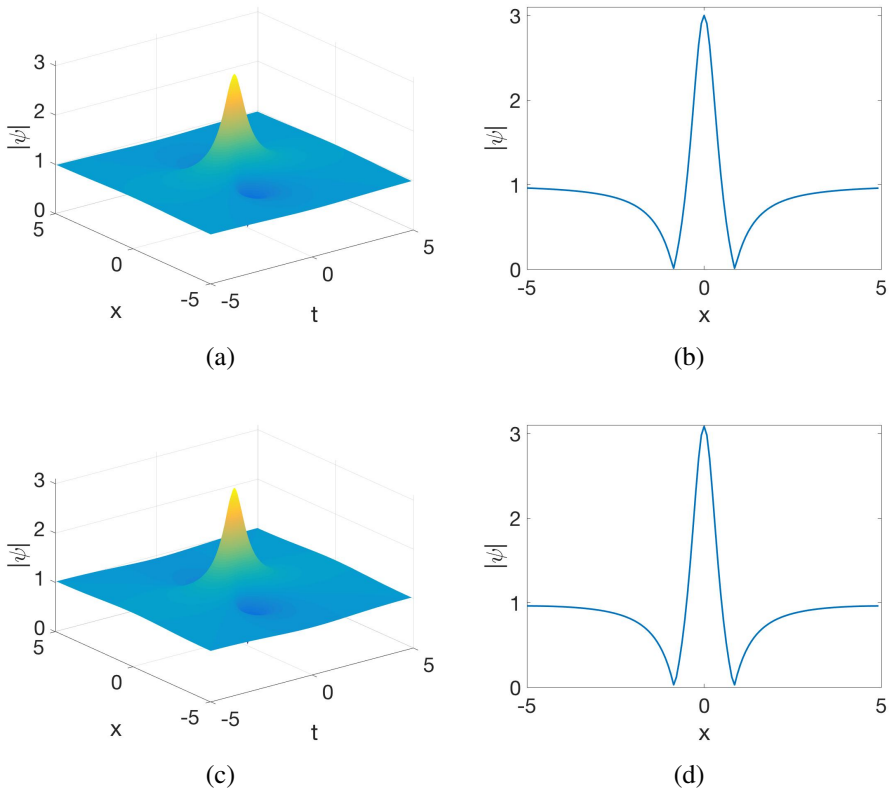

Figure 6.1: Comparison of the Peregrine soliton (a) with the numerical solution (c). Time slice at $t = 0$ of the exact solution (b) and numerical solution (d). Excellent agreement is seen between the two solutions.

waves. Fig. 6.1 shows the exact Peregrine soliton (a) compared to that obtained by the numerical method (c). Fig. 6.1(b) and Fig. 6.1(d) show the spatial cross section at time $t = 0$ for the analytical and numerical solutions, respectively. We see that despite the periodic boundary conditions the two solutions are nearly identical; in fact, the pointwise error is on the order of 10^{-2}.

As an additional case example for the convergence of the code, we considered the case of rogue waves atop a cnoidal (space-time periodic) background [108] instead of the usual constant background. Fig. 6.2(a) shows an exact, cnoidal rogue wave we obtained by using the procedure of [108]. On the other hand, Fig. 6.2(c) shows the solution obtained by the Newton-CG method. As before, Fig. 6.2(b), (d) show the cross section at time $t = 0$ of the

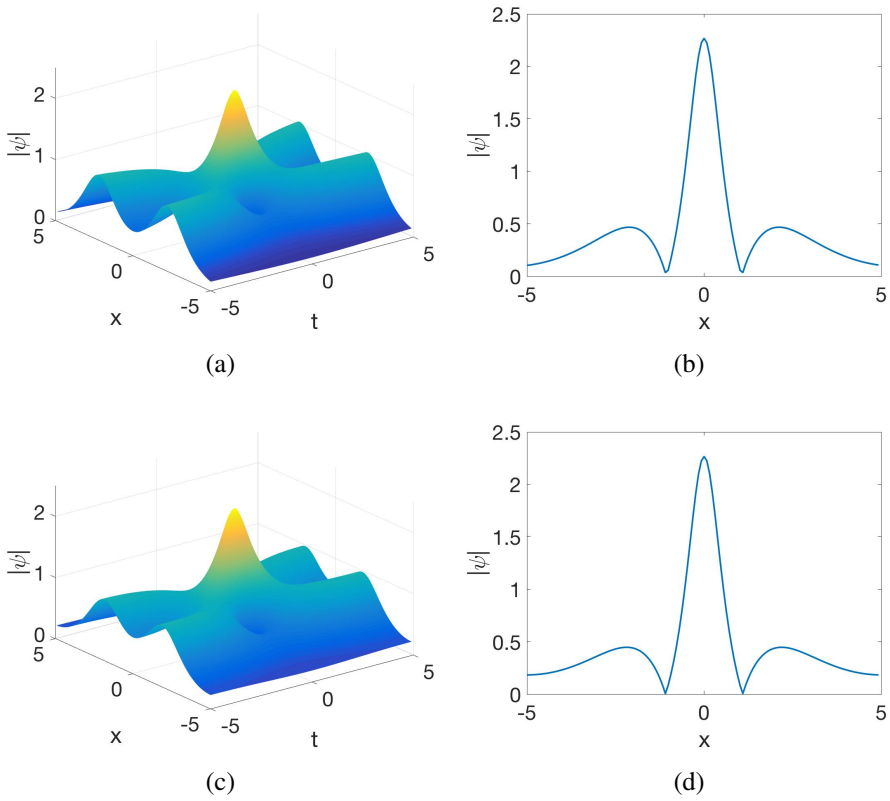

Figure 6.2: Comparison of an exact cnoidal rogue wave in (a) with the numerical solution (c). Slice at $t = 0$ of the exact solution (b) and numerical solution (d). Again, we see very good agreement between the two solutions.

exact and numerical solutions, respectively. Again, we see good agreement between the two solutions with only slight differences between the tails.

Next, we look for solutions outside of the integrable case scenario but for which some information is known. Specifically, in the presence of TOD within Eq. (6.1), the work of [77] gives a first-order perturbative solution (for $p = 1$) in the form

$$\psi = [\frac{4(1+2it)}{1+4x^2+4t^2} - 1 + \frac{i(f-ik)}{(1+4x^2+4t^2)^2}]e^{it} \tag{6.2}$$

where $f = 8x(24x^2+24t^2-6)\epsilon$ and $k = 192tx\epsilon$. When $\epsilon = 0$, this reduces to the standard Peregrine soliton but when $\epsilon \neq 0$ the result is a slightly rotated rogue wave. Fig. 6.3(c) shows the pertubative solution for $\epsilon = 0.02$ while Fig. 6.3(a) shows the $\epsilon = 0$ case for

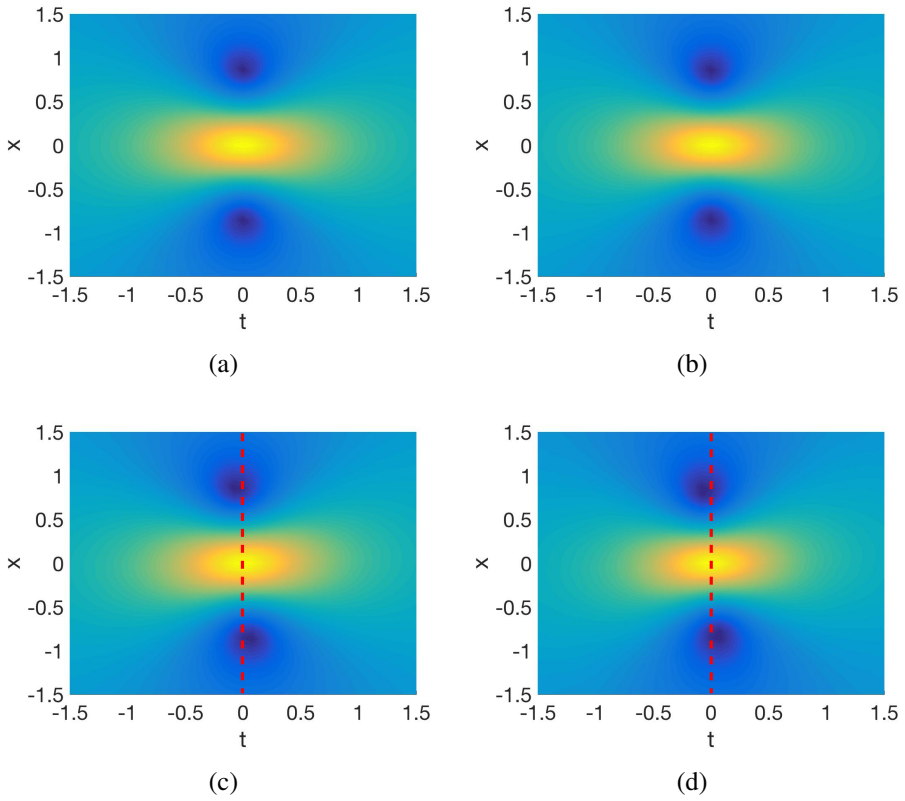

Figure 6.3: (a) Contour plot of the Peregrine soliton. (b) Corresponding solution obtained numerically. (c) Contour plot of the perturbative solution Eq. (6.2), while (d) is the corresponding numerical solution. Although it is weak, there is a discernible asymmetry in panels (c) and (d) (as compared with (a) and (b)) caused by the TOD term. Here we have set $\epsilon = 0.02$. We have also included the vertical red bar in (c) and (d) so as to highlight the slight rotation (in comparison to the $\epsilon = 0$ case where the peak and dips of the PS are are aligned).

comparison. Although it is faint, a slight rotation in the counter-clockwise direction can be seen when comparing the two. On the other hand, Figs. 6.3(b),(d) are the corresponding solutions that we obtained numerically. Again, good agreement is found between a predicted solution (both for $\epsilon = 0$ and for $\epsilon \neq 0$) and our numerical solution. Hence, we confirm that such PS structures are present in TOD perturbations of the original NLS model.

Armed with the understanding and expectations suggested by this example, we now move to a more interesting and unexplored case. In particular, instead of restraining considerations to the cubic nonlinearity, we examine general powers p, asking whether the

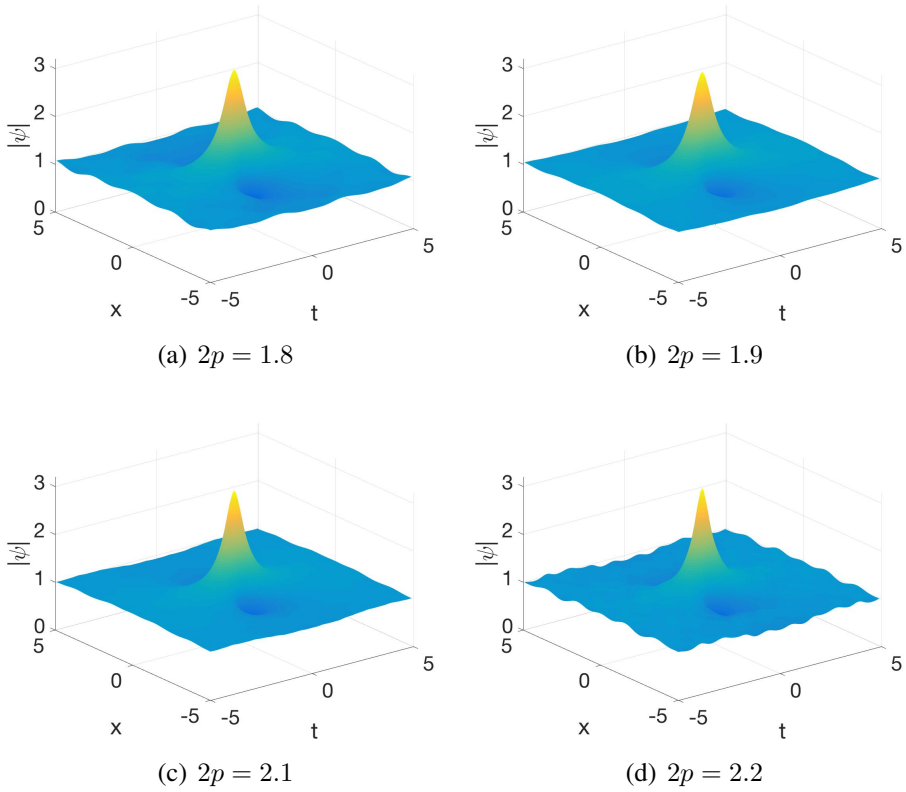

(a) $2p = 1.8$ (b) $2p = 1.9$

(c) $2p = 2.1$ (d) $2p = 2.2$

Figure 6.4: Family of solutions with $\epsilon = 0$ for different values of p around the integrable limit of $p = 1$. The profiles confirm the persistence of the rogue wave.

rogue wave patterns will persist. Fig. 6.4 shows several solutions obtained via the Newton-CG method. We initially converged to a solution at $(p, \epsilon) = (1, 0)$ using the PS as our initial iterate. By increasing/decreasing p and using the previously obtained solution as our new initial iterate, we obtained the other solutions via the Newton-CG method.

For small perturbations in p, in Fig. 6.4(b), (c), we see that the background remains approximately flat. As far as we know, this is the first systematic indication that rogue waves exist in the NLS (in a parametrically continuous way) past the integrable limit of the cubic nonlinearity; this is a result that is of particular importance in connection with the robust experimental observation of such events. However, for larger perturbations in p, as in Fig. 6.4(a), (d), we see that the background obtains seemingly periodic ripples. One can argue that this perturbation on top of the flat background may be introduced in order

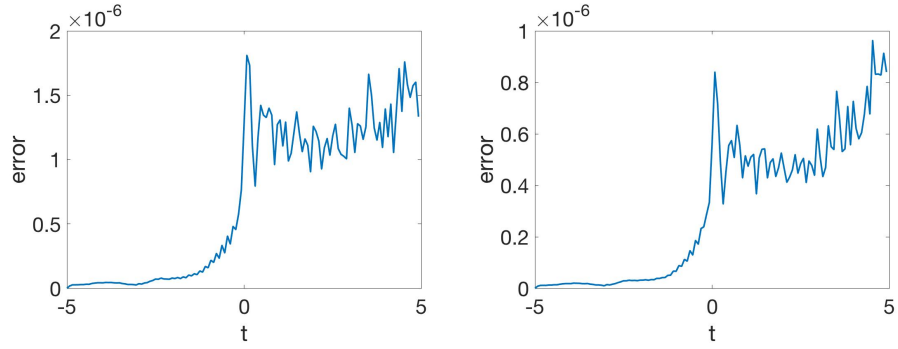

(a) $2p = 1.8$ (b) $2p = 1.9$

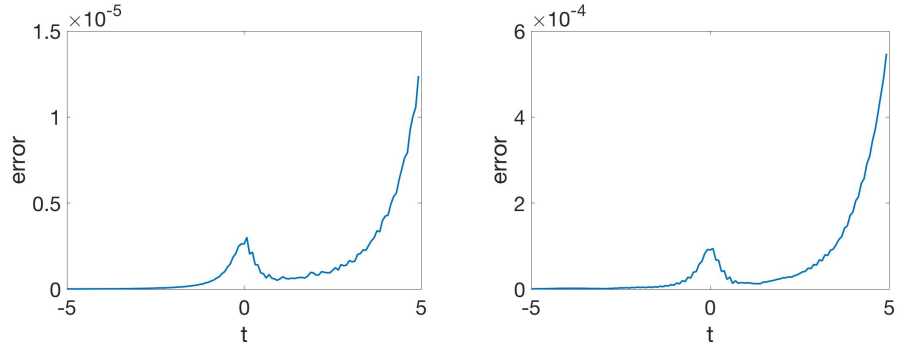

(c) $2p = 2.1$ (d) $2p = 2.2$

Figure 6.5: Direct numerical simulation results confirming that evolution through the ETDRK4 method yields excellent agreement with the Newton-CG findings. The error is measured via the L^∞ norm (in space) of the difference at each point in time between the time-evolved (ETDRK4) and the Newton-CG solution. Here $\epsilon = 0$.

to ensure periodicity within the given computational domain (see also Fig. 6.7(d)). Irrespective of these non-uniformities in the background, the presence of a wave that appears out of nowhere and disappears without a trace is eminently transparent in these *converged* solutions.

It is crucial to note here that to ensure that these are proper solutions of the original PDE of Eq. (6.1), we have performed direct numerical simulations with the ETDRK4 time-stepping algorithm [89, 90]. Fig. 6.5 shows the corresponding results. The general trend in all diagrams is that the solutions agree until slightly after the peak of the rogue wave begins to decay. This is consistent with the occurrence and growth of the modulation instability of the background, further confirming the existence of these objects.

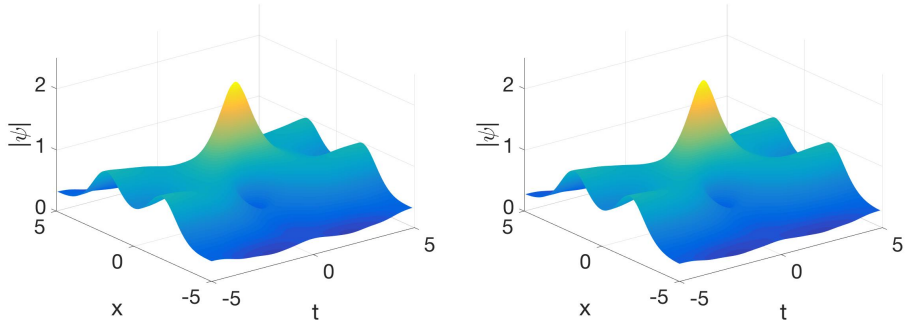

(a) $2p = 1.8$ (b) $2p = 1.9$

(c) $2p = 2.1$ (d) $2p = 2.2$

Figure 6.6: Same as Fig. 6.4 but now for the family of rogue waves on top of the cnoidal background with $\epsilon = 0$.

To confirm the generality of the findings, we have also examined the waveforms on top of the cnoidal background in Fig. 6.6. These have also been identified through our Newton-CG technique for different values of p. It is interesting to note that in this case the system converges to a state without a small periodic perturbation to the background. Furthermore, we were able to perform the continuation in this case from $p = 0$ all the way to $p = 2$. Additionally, the solutions obtained via the ETDRK4 integrator agree with the solutions obtained by the Newton-CG far better than those obtained on the flat background. A posteriori, it can be argued that this is to be expected considering these solutions more naturally conform to the imposed periodic boundary conditions.

Lastly, Fig. 6.7 serves to make the case that the solutions of interest exist not only along the axes of our two-dimensional (p, ϵ)-plane, but also for nonzero values of both parameters, i.e., under combinations of different perturbations. Here, we have verified the convergence of the Newton-CG iterative approach to a profile bearing a rogue wave for different values of p, and $\epsilon = 0.02$.

6.2 Implementation Details

6.2.1 Methods

To obtain the results in this chapter, our primary tool was the Newton conjugate gradient method, suitably adapted from the earlier work [107]. The method approximates a solution of a partial differential equation (PDE) by expanding it into complex exponentials and then solving the resulting system for the amplitudes (i.e., a pseudo-spectral Galerkin method). Finding a solution is accomplished with Newton's method except that the linear system is solved iteratively via the conjugate gradient method. Two major benefits of this method is that it is spectrally accurate in both space and time, and it is relatively straightforward to code (see the following section).

However, due to the choice of basis functions, the method implicitly assumes periodic boundary conditions. In that light, we attempt to use a domain that is sufficiently large

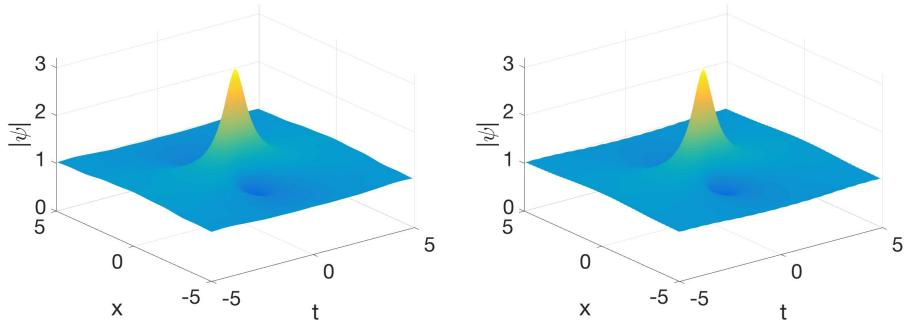

(a) $2p = 1.8$ (b) $2p = 1.9$

(c) $2p = 2$ (d) $2p = 2.1$

Figure 6.7: Persistence of rogue waves for both $p \neq 1$ and $\epsilon \neq 0$ through the family of solutions with $\epsilon = 0.02$.

for the rogue wave structures to approach their equilibrium state, yet small enough to avoid issues with either the size of the computation or the instability of the background. Thus, the computations reported herein have been performed in a space-time domain $[-5,5]\times[-5,5]$. Lastly, we terminated the Newton-CG iterations once the L^∞ error in the residual drops below 10^{-8}.

To confirm dynamically the results of the Newton-CG iteration, we also used time-integration techniques. Specifically, we used the fourth order in time, spectral in space, time integrator ETDRK4 [89, 90]. For the initial condition in the integrator, we used the $t = -5$ time slice (of the relavant solution) obtained from the Newton-CG method. We then integrated this out to $t = 5$. As mentioned above, this choice of time domain allows for the comparison of the two solutions *before* the modulational instability starts playing a crucial role in the dynamics.

6.2.2 Newton-CG code for the NLS Peregrine Soliton

The following is an example of the code we used to obtain the rogue waves appearing in this chapter. It is a suitable adaptation to the present setting of the code of [107].

```
%Newton-CG for finding Rogue Waves in NLS with TOD (see epsn below)
% iu_t + (1/2)u_xx - i\epsilon u_xxx + |u|^{2p} u - u =0

clear
%GRID SET UP
Lt=10; Lx=10;
Nt=2^7; Nx=2^7;
t=-Lt/2:Lt/Nt:Lt/2-Lt/Nt; x=-Lx/2:Lx/Nx:Lx/2-Lx/Nx;
kt=[0:Nt/2-1 -Nt/2:-1]*2*pi/Lt; kx=[0:Nx/2-1 -Nx/2:-1]*2*pi/Lx;
[T,X]=meshgrid(t,x); [KT,KX]=meshgrid(kt,kx);

errormax=1e-8;
errorCG=1e-2;


%LINEAR DERIVATIVES AND PRECONDITIONER
c=5;
p=1; epsn=0;
K2=KT+(1/2)*KX.^2 + epsn*KX.^3;
fftM=c+K2.^2;

```

```
%INITIAL CONDITION
PP=@(t,x) 1- 4*(1+2i.*t)./(1+4*x.^2 + 4*t.^2);
U=PP(T,X);


%NEWTON-CG LOOP
ncg=0;
ITER=20000;
flag=1;
while flag==1  && ncg <= ITER

  %Error and Stop Condition
  L0U=ifft2(-K2.*fft2(U))+ (abs(U).^(2*p)).*U - U;
   err=max(max(abs(L0U)))

  if err < errormax
     flag=0;
  end


  %CG-Iteration
  dN= @(D) (p+1).*(abs(U).^(2*p)).*D +...
                          (p).*(U.^2).*(abs(U).^(2*p-2)).*conj(D);

  L1= @(D) ifft2(-K2.*fft2(D))-D + dN(D);
  L1A= @(D) ifft2(-K2.*fft2(D))-D + dN(D);


  R=-L1A(L0U);
  DU=0*U;
  MinvR=ifft2(fft2(R)./fftM);
  R2new=sum(sum(conj(R).*MinvR));
  R20=R2new;
  P=MinvR;
  while(abs(R2new) > abs(R20)*errorCG^2 && flag==1)
     L1P=L1(P); LP=L1A(L1P);
     a=R2new/sum(sum(real(conj(P).*LP)));
     DU=DU+a*P;
     R=R-a*LP; MinvR=ifft2(fft2(R)./fftM);
     R2old=R2new;
     R2new=sum(sum(real(conj(R).*MinvR)));
     b=R2new/R2old;
     P=MinvR+b*P;
     ncg=ncg+1;
  end

  %Newton Iteration
  U=U+DU;
end

%PLOT
figure; surf(t,x,abs(U))
shading interp, lighting phong
xlabel('t'); ylabel('x'); zlabel('abs(U)');
```

CHAPTER 7

ROGUE WAVES AS SELF-SIMILAR SOLUTIONS ON A BACKGROUND: A DIRECT CALCULATION

7.1 Self-Similar Calculation for the NLS case

Let us start with the prototypical NLS model of the form:

$$iu_t = -\frac{1}{2}u_{xx} - |u|^2 u + u, \tag{7.1}$$

whereby we have already set the background at unity without loss of generality. Now let us recall that the Peregrine waveform emerges against the backdrop of a constant background $u = 1 + w$. Then, the equation for the new variable $w(x,t)$ reads:

$$iw_t = -\frac{1}{2}w_{xx} - |w|^2 w - (w + w^\star) - (2|w|^2 + w^2). \tag{7.2}$$

The star here denotes complex conjugation. We now follow the so-called MN-dynamics self-similar framework which has been detailed in a number of different publications [109–111] (and is also tantamount to methods generally applied for obtaining self-similar solutions; see, e.g., [112]). More specifically, we use $w(x,t) = A(t)F(\frac{x}{L(t)}, t)$. This leads to the equation:

$$\begin{aligned} i \quad & \left(A_t F + AF_t - A\xi F_\xi \frac{L_t}{L}\right) = -\frac{1}{2}\frac{A}{L^2}F_{\xi\xi} - |A|^2 A|F|^2 F \\ - \quad & (AF + A^\star F^\star) - (2|A|^2|F|^2 + A^2F^2). \end{aligned} \tag{7.3}$$

In the above equation, $\xi = x/L(t)$. We will now seek self-similar solutions, by making two important assumptions. First, we will assume that the solutions are *stationary in the*

self-similar frame. This is not a restricting assumption: it simply demands that we have self-similar solutions as such. The second assumption is that we will assume F to be a real profile. A priori, this is not mandated, nevertheless an understanding of the inner workings of the method suggests that it would not be possible to scale terms like the ones of the second line of Eq. (7.3) barring such a restriction. Effectively, we assign all the complex phase dependence in $A(t)$. Using on the basis of the above $F_t = 0$ and also decomposing $A(t) = Re^{i\theta}$, we obtain the following terms:

$$\begin{aligned} i \quad & \left(\frac{R_t}{R}F - \xi F_\xi \frac{L_t}{L}\right) - \theta_t F = -\frac{1}{2L^2}F_{\xi\xi} - R^2F^3 \\ - \quad & (1 + e^{-2i\theta})F - F^2R(2e^{-i\theta} + e^{i\theta}). \end{aligned} \tag{7.4}$$

Expressing the last two parentheses as a function of R and θ (and F) and splitting real and imaginary parts, we inherit the real part equation:

$$-\theta_t F = -\frac{1}{2L^2}F_{\xi\xi} - R^2F^3 - 2\cos^2(\theta)F - 3R\cos(\theta)F^2. \tag{7.5}$$

For self-similarity to work here in the corresponding self-similar frame, we need the time dependent terms to cancel and independently the time-independent terms to do the same. This leads to the choice

$$R^2 = \frac{1}{L^2} = 2R\cos(\theta), \quad 2\cos^2(\theta) = \theta_t. \tag{7.6}$$

The latter, in turn, yields $\tan(\theta) = 2(C + t)$, where C shifting the origin of time can be set to 0 without loss of generality. Then $\cos^2(\theta) = 1/(1 + 4t^2)$ leading to

$$L = \frac{1}{R} = \frac{\sqrt{1 + 4t^2}}{2} \Rightarrow A = \frac{2}{1 - 2it}. \tag{7.7}$$

Having found the temporal prefactor, the resulting real equation for the wave profile now reads:

$$-\frac{1}{2}F_{\xi\xi} - F^3 - \frac{3}{2}F^2 = 0. \tag{7.8}$$

Using the above Eqs. (7.6)-(7.7) to simplify the imaginary part of the Eq. (7.4) canceling from all the terms a factor of $\sin(2\theta)$, we retrieve a first-order equation for the same profile, namely:

$$\xi F_\xi = -2F - F^2. \tag{7.9}$$

We can solve this first order ODE to obtain the solution

$$F(\xi) = -\frac{2}{1 + D\xi^2}; \tag{7.10}$$

now a direct substitution of this waveform in Eq. (7.8) yields straightforwardly that the solution is valid only for $D = 1$, hence we obtain $F = -2/(1 + \xi^2)$. We now reconstruct our solution:

$$u = 1 + W = 1 + \frac{2}{1 - 2it}\left(-\frac{2}{1 + \xi^2}\right) = 1 - 4\frac{1 + 2it}{1 + 4x^2 + 4t^2}, \tag{7.11}$$

which naturally retrieves the well-known Peregrine structure [72]. It is important to make some remarks here:

- The expressions of Eq. (7.11) bring forth the self-similar nature of the Peregrine, which, in our view, seems to have been overlooked in the literature. Factoring out the time dependence as a complex factor ($\propto 1/(1-2it)$), one is left with an effective Lorentzian self-similar waveform which is at the heart of the self-similarity-based calculation of the structure as a steady state solution of the relevant formulation.

- Nevertheless, there are some nontrivial differences of this calculation from other similar calculations, e.g., in the above mentioned references such as [109–111]. Here, when separating, for instance, the real part of the solution, there are both time-dependent and time-independent terms and these need to be balanced out between them separately (the former on their own, and the latter on their own). Perhaps even more importantly, the real and imaginary parts yield 2 distinct differential equations that have a particular solution in common that needs to be singled out upon a suitable selection of a compatibility constant.

Nevertheless, the above procedure can be utilized whenever it may be believed (e.g., motivated from numerical or physical experiments) that extreme waves may exist in a certain system. The methodology only hinges on identifying such a self-similar solution on top of a background and in no way utilizes the integrable structure of the model. In a sense, it is an analogous calculation (for rogue waves) to the reduction of the NLS, when looking for its standing waves, to a Duffing oscillator whose homoclinic or heteroclinic connections correspond to the bright or dark solitons respectively. To the best of our knowledge such as an ODE-reduction-based calculation has not previously appeared in the context of rogue waves. To illustrate that this viewpoint for the consideration of rogue wave patterns can be used in other (admittedly related) examples beyond "just NLS", we consider now a series of generalizing cases, including the Hirota model in 1+1 dimensions and the Davey-Stewartson and Zakharov models in higher (i.e., 2+1) dimensional settings. The Hirota model incorporates effects such as the third order dispersion and the time-delay correction to the cubic nonlinearity, as discussed, e.g., in [113]. The Davey-Stewartson model is a relevant one for the examination of the evolution of a wave-packet in a (2+1)-dimensional setting for water of finite depth [10]; here, we consider the setting of large surface tension in the form of the so-called DSI model. Finally, the Zakharov equation was derived in [114] as a prototypical integrable model in (2+1)-dimensions.

7.2 Going Beyond NLS: Other Models

7.2.1 Hirota Equation

The Hirota equation:

$$iu_t + \frac{1}{2}u_{xx} + |u|^2u - \alpha i u_{xxx} - 6\alpha i|u|^2u_x = 0, \tag{7.12}$$

where α is an arbitrary constant, has a rogue wave solution of the form [115]

$$u(x,t) = e^{it}\left(1 - \frac{4(1+2it)}{1+4(x+6\alpha t)^2+4t^2}\right) \tag{7.13}$$

Again, by factoring out $1+4t^2$ from the bottom, we may write

$$u(x,t) = e^{it}\left(1 + \frac{2(1+2it)}{1+4t^2}\cdot\frac{-2}{1+\xi^2}\right). \tag{7.14}$$

where

$$\xi = \frac{2(x+6\alpha t)}{\sqrt{1+4t^2}}.$$

We then see that the rogue wave of the Hirota equation is, in a very natural way, a self-similar, Peregrine-like structure in a co-traveling reference frame where the coherent structure travels with speed 6α. Hence, it can be retrieved by a similar calculation as the one above.

7.2.2 Davey-Stewartson I

The $(2+1)$-dimensional Davey-Stewartson I (DSI) equation

$$iu_t = u_{xx} + u_{yy} + |u|^2u - 2Qu \tag{7.15}$$

$$Q_{xx} - Q_{yy} = (|u|^2)_{xx}, \tag{7.16}$$

has a rogue wave solution [116] of the form:

$$u(x,y,t) = \sqrt{2}\left(1 - \frac{4(1-2i\omega t)}{1+(k_1x+k_2y)^2+4\omega^2t^2}\right) \tag{7.17}$$

$$Q(x,y,t) = 1 - 4k_1^2\frac{1-(k_1x+k_2y)^2+4\omega^2t^2}{(1+(k_1x+k_2y)^2+4\omega^2t^2)^2}, \tag{7.18}$$

where $k_1 = p - \frac{1}{p}$, $k_2 = p + \frac{1}{p}$, $\omega = p^2 + \frac{1}{p^2}$, and p is an arbitrary constant. We note here that this is a line rogue wave, resembling the Peregrine structure extended along a line in the xy-plane. We can write this in the self-similar form

$$u(x,y,t) = \sqrt{2}\left(1 + \frac{2(1-2i\omega t)}{1+4\omega^2t^2}\cdot\frac{-2}{1+\xi^2}\right) \tag{7.19}$$

$$Q(x,y,t) = 1 + \frac{4k_1^2}{1+4\omega^2t^2}\cdot\frac{\xi^2-1}{(\xi^2+1)^2} \tag{7.20}$$

where

$$\xi = \frac{k_1x+k_2y}{\sqrt{1+4\omega^2t^2}}.$$

Hence, in this case too, the structure can be thought of as being stationary in a suitable self-similar frame of reference.

7.2.3 Zakharov Equation

The (2+1)-dimensional Zakharov equation assumes the form [114]:

$$iu_t = u_{xy} + Qu \tag{7.21}$$

$$Q_y = 2(|u|^2)_x. \tag{7.22}$$

This model also admits line-type rogue waves [117], which we will simply give in self-similar form:

$$u(x,y,t) = 1 + \frac{2(1+4it)}{1+16t^2} \cdot \frac{-2}{1+\xi^2} \tag{7.23}$$

$$Q(x,y,t) = \frac{16}{1+16t^2} \cdot \frac{\xi^2 - 1}{(\xi^2+1)^2} \tag{7.24}$$

where

$$\xi = \frac{2(x-y)}{\sqrt{1+16t^2}}.$$

Lastly, we remark that a change in the time scale will change the $\sqrt{1+16t^2}$ to $\sqrt{1+4t^2}$, as in the other examples. This is due to a rescaling of time imposed effectively by the prefactor within Eq. (7.22).

CHAPTER 8

CONCLUSIONS

8.1 The Camassa-Holm Nonlinear Schrödinger Equation in One Space Dimension

Using asymptotic methods on the defocusing CH-NLS equation, we have derived an effective Boussinesq-type equation (to describe bi-directional waves) and from there a pair of KdV models characterizing propagation in each of the one-dimensional directions. This has permitted us to systematically construct approximate one-dimensional coherent structures in an explicit way of both dark and anti-dark form, identifying their respective domains of existence.

We have then used systematic numerical simulations to illustrate that these structures indeed persist in the full, original CH-NLS model. Not only have we explored individual such structures, but we have also considered pairs of them and observed them to emerge practically unscathed as a result of their collisions in the regime of (small) amplitudes considered.

These results offer a first glimpse into the possibilities of the defocusing nonlinear realm for the case of the CH-NLS model. Nevertheless, numerous open questions still remain in this context. The technique used here only allows us to construct small-amplitude structures. Yet, the question of whether "deep" dark solitons (including black ones) exist and whether they are dynamically robust would require a different type of approach in order to be addressed. Additionally, whether such structures may be identified in closed analytical form is of interest in its own right. Questions including the potential collapse features,

the existence and stability of vortices, among many others await further investigation and would be intriguing to explore in their own right.

8.2 The Camassa-Holm Nonlinear Schrödinger Equation in Two Space Dimensions

In this work, we have studied the defocusing Camassa-Holm–Nonlinear Schrödinger (CH-NLS) equation. We have shown that this model possesses a stable continuous-wave (cw) solution, on top of which small-amplitude soliton solutions can be supported. Our analytical approach was based on asymptotic multiscale expansion methods, which allowed us to reduce the CH-NLS model to a Kadomtsev-Petviashvili (KP) equation. Both versions, namely the KP-I and KP-II, were found to be possible, depending on the sign of a characteristic parameter.

The reduction to the KP model allowed us to construct approximate soliton solutions, both line solitons and lumps, and either of the dark or of the anti-dark type, of the original CH-NLS model. Domains of existence of all these structures, as well as their dynamics by means of direct numerical simulations, were investigated. We found that line and lump solitons do persist in the original model, but as their amplitude is increased, they undergo deformations, i.e., bending and a radial expansion, which may form other, ring-shaped, structures. We also studied head-on collisions between line solitons, between lumps, as well as between line solitons and lumps, and found that they are almost elastic (although less so as the amplitude of the structures increases). In our simulations, we have also used generic Gaussian initial data, the dynamics of which were found to follow qualitative features of the approximate soliton solutions' dynamics.

There are many interesting topics for future studies. First of all, it would be interesting to study the transverse dynamics of large-amplitude dark solitons and investigate their instability, and the concomitant generation of vortices (similarly to the traditional 2D defocusing NLS model [87, 88]). The study of other quasi-2D or purely 2D structures, such as

the ring dark or anti-dark solitons (which were already identified in our simulations) and vortices, respectively, constitute still other themes of particular interest, as also highlighted by select ones among our numerical computations (e.g., the case of the radially symmetric Gaussian initial condition). Relevant studies are in progress and pertinent results will be reported in future publications.

8.3 The Camassa-Holm Derivative Nonlinear Schrödinger Equation

Given the wide applicability of DNLS equations in plasma physics and magnetohydrodynamics and the relevance of CH-type deformations in contexts associated with water waves, the CH-DNLS equation is an interesting model to study. The relevant partial differential equation was reduced to the MKdV and KdV equations by employing two different multiscale expansion methods. The reduction to the MKdV and KdV equations allowed us to construct approximate solitary wave solutions of the original CH-DNLS equation by using the explicitly known soliton solutions of the former.

We then used direct numerical simulation to demonstrate the relevance of these solitary waves in the original CH-DNLS equation. Their dynamical evolution and their interactions were also analyzed and discussed. We found that for the small amplitude initial conditions(see Fig. 4.1), the numerics and the theory are in very good agreement. For larger amplitudes, the derived solutions persist and can undergo nearly elastic head-on collisions, although some radiation can clearly be discerned both at their initialization as well as during their collisions.

Numerous open questions still remain in this context. Whether one can find exact solutions of the CH-DNLS model is of interest in its own right. The dynamics of the DNLS equation (in higher dimensions or different powers of the nonlinearity) is intriguing in connection to collapse type features that have been of considerable recent interest [118]. Examining how these features are modified in the CH-DNLS case would be relevant to consider.

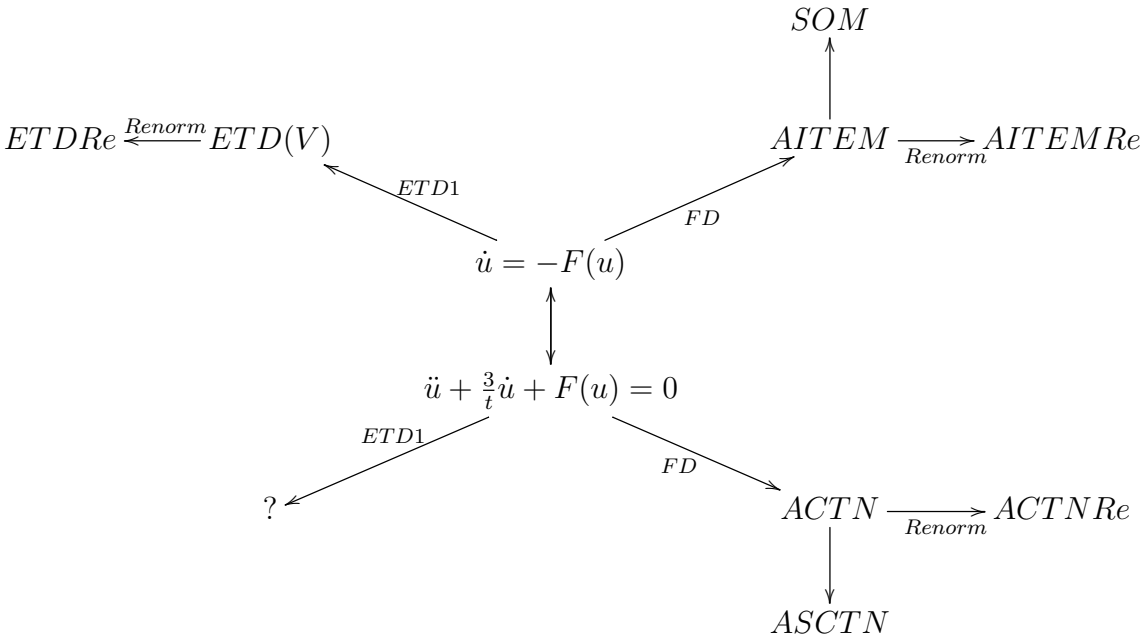

Figure 8.1: Schematic showing the relationships of the various methods appearing in Chapter 5. Here FD denotes the finite difference discretization of time used to obtain the specific schemes AITEM and ACTN. Finally, the question mark represents a possible (not obtained here) scheme in which the time discretization of CTN is done via exponential time-differencing methods.

8.4 A Toolkit For Steady States of Nonlinear Wave Equations: Continuous Time Nesterov and Exponential Time Differencing Schemes

We have developed a collection of twists on current methods for computing both ground and excited, and in principle both stable and unstable, stationary states of nonlinear wave equations. The following diagram summarizes the techniques used in Chapter 5 when attempting to solve $F(u) = 0$ as the stationary problem originating from a nonlinear wave equation; the linear part of F is implicitly assumed in what follows to bear a negative Laplacian, as it typically does for Schrödinger type operators.

Exponential time differencing methods, given their desirable stability properties, are a cheap and efficient alternative to finite-difference approaches. Traditionally, the Laplacian has been considered as the linear part in the associated Duhamel formula; however, we

have shown that there may be advantages in considering the term bearing the potential as the linear part instead. The future possibility of an explicit preconditioner for ETD methods may also be of interest.

Given a constrained optimization problem and an associated iterative procedure, we have outlined how to apply renormalization so that the constraint will be accounted for, at least in principle. It is certainly worthwhile to explore further how well these methods compare with other constrained optimization techniques, as well as proofs of convergence and convergence rates. In particular, in the examples above we saw that the renormalized methods were able to converge to unstable stationary states; a natural question is to what extent can renormalized methods be engineered to converge to (potentially even arbitrary) unstable states.

Our chief interest in this contribution, however, was to introduce and explore the continuous time Nesterov method as applied to PDEs, especially focusing on the elliptic, nonlinear, rich examples stemming from the steady state problem of the nonlinear Schrödinger equation. For finding ground states, the examples considered imply that accelerated continuous time Nesterov schemes generically converge linearly and are quite competitive with other linearly converging methods; one possible future direction of work could be devoted to establishing the linear nature of the convergence under certain conditions. We have also shown that a squared operator variant of such a method will converge to excited states and the examples also imply it has a linear convergence rate; the proof of such a feature is once again an open problem. Developing an exponential time differencing scheme which is compatible with Nesterov type (continuous time) iterations might provide an especially efficient way of seeking such standing waves.

On the other hand, comparing these classes of methods with Newton type methods, or quasi-Newton ones, involving Jacobian evaluations, but also accounting for sparsity features etc., and doing so for both one- and multi-dimensional problems would naturally be of substantial interest. Eventually, extending such techniques beyond steady states to

periodic orbits and limit cycles would also constitute an important step of wide appeal to a broad and diverse array of problems.

8.5 Evaluating the Robustness of Rogue Waves Under Perturbations

We have examined the question of whether rogue wave structures can persist under different types of perturbations in the realm of NLS equations. We have adapted a computational approach based on a Newton-conjugate gradient method to identify the Peregrine soliton solutions, both on top of a homogeneous background and on top of a cnoidal-wave background. We have verified that such solutions can be identified both for the case of a power law nonlinearity (beyond the cubic integrable limit) and for a model with third-order dispersion, as well as in a model that combines both of the above integrability-breaking perturbations.

These findings pave a new avenue of understanding of such extreme wave events. They enable us to seek them *beyond* the narrow confines of integrability in a systematic way that does not need the Lax pair formulation and analytical or perturbative solutions. At the same time, they suggest numerous questions for further investigations. Starting with the computations performed, they enhance (e.g. through the ETDRK4 results confirming the solutions identified) the belief that all of these solutions are rather unstable due to their unstable background. Hence, the necessity of a framework in which these solutions are understood as metastable and/or are present without a homogeneous background is progressively becoming more dire, so as to justify, among other things, their undisputed emergence in experiments and in realistic physical settings. Perhaps such a framework is that of the gradient catastrophe of [119], yet this is still a topic worthwhile of further study.

In a different vein, the numerical method used here employs periodic boundary conditions. As a result the solutions obtained are, effectively, periodic in space and time. It would certainly be desirable to deploy a method that either involves the well-known asymptotics (in space and time) of the Peregrine soliton, or one that accounts (in some way reminiscent

of transparent boundary conditions) for the algebraic decay of the wave structure. This is an interesting direction for further numerical developments. Such studies are presently under consideration and will be reported in future publications.

8.6 Rogue Waves as Self-Similar Solutions on a Background: A Direct Calculation

We have argued that while the IST and related techniques (including e.g. the Darboux transformation etc.) provide valuable tools for identifying such solutions in the realm of integrable models, this methodology is limited in comparison to more realistic models that bear non-integrable perturbations and for which experimental or numerical observations suggest that the structures may persist. A perturbative framework either analytically [77, 79, 120] or numerically [121] may be useful in such scenarios. Nevertheless, we argue that a potentially valuable complementary perspective is that of looking at rogue wave patterns as self-similar solutions that are associated with a (potentially complex) time-dependent prefactor and a self-similar (e.g. in the NLS case, Lorentzian) profile, arising against the backdrop of a constant, non-vanishing background. Seeking these solutions through a self-similar type of methodology, as was done for some prototypical case examples herein, enables a way to tackle such solutions that is not bound by the limitations of integrable models and can instead be applied to a wider range of systems.

That being said, in the present proof of principle exposition we have only retrieved case examples where the existence of such waveforms was already identified by integrable structure means, in order to illustrate the ability of the method to capture such waveforms. However, it would be of particular interest to attempt a similar search in model examples where rogue structures are expected to exist, yet the absence of integrability does not allow for their identification. This is one of the key challenges of the method towards future work. A related challenge lies in the potential for consideration of stability features in the self-similar frame. This was done, e.g., in [110], but also, importantly, in a series of

works of [122, 123]; see also [124]. These efforts have not only identified the spectra of self-similar waveforms (which are steady in the self-similar frame); they have importantly made a substantial effort to "reinterpret" the spectra of the latter setting into the original frame. An important example of this class is that certain symmetries (such as, e.g., the potential shift of the collapse time in non-autonomous systems) may amount to eigendirections appearing as unstable, which, yet, are not so due to the existence of the corresponding symmetry (in the original frame). This is yet to be done for the Peregrine soliton of the NLS and related waveforms. We have attempted this and have been hindered by technical complications having to do with the nature of the emerging terms in Eq. (7.3). This is the same complication that we encountered previously in that some of the terms are autonomous and some are not. The potential existence of a systematic way to bypass this complication would pave a systematic way for identifying (and subsequently reinterpreting in the spirit of [122,123]) the spectra of extreme wave events, a feature crucial for formulating a more precise notion of their stability. Up to now the latter has been explored in either a somewhat empirical (and often mathematically not suitably substantiated) way or in the form of a limiting procedure of, e.g., periodic states; see the relevant discussion of [125]. Nevertheless, such a direct approach as proposed here would be fundamentally superior to the current state of the art, in our view, and hence constitutes a particularly worthwhile topic for future study.

BIBLIOGRAPHY

[1] R. Camassa and D. D. Holm, Phys. Rev. Lett. **71**, 1661 (1993).

[2] A. Constantin and D. Lannes, Arch. Ration. Mech. Anal. **192**, 165 (2009).

[3] R. S. Johnson, J. Fluid Mech. **455**, 63 (2002).

[4] A. Boutet de Monvel, A. Kostenko, D. Shepelsky and G. Teschl, SIAM J. Math. Anal. **41**, 1559 (2009).

[5] A. Constantin, V. Gerdjikov and R. I. Ivanov, Inverse Problems **22**, 2197 (2006).

[6] R. Beals, D. Sattinger and J. Szmigielski, Adv. Math. **140**, 190 (1998).

[7] A. Constantin and W. Strauss, Phys. Lett. A **270**, 140 (2000).

[8] H. H. Dai, Acta. Math. **127**, 193 (1998).

[9] M. J. Ablowitz and P. A. Clarkson, *Solitons, Nonlinear Evolution Equations and Inverse Scattering* (Cambridge University Press, Cambridge, 1991).

[10] M. J. Ablowitz, B. Prinari, and A. D. Trubatch, *Discrete and Continuous Nonlinear Schrödinger Systems* (Cambridge University Press, Cambridge, 2004).

[11] M. J. Ablowitz, *Nonlinear Dispersive Waves: Asymptotic Analysis and Solitons* (Cambridge University Press, Cambridge, 2011).

[12] C. Sulem and P.L. Sulem, *The Nonlinear Schrödinger Equation* (Springer-Verlag, New York, 1999).

[13] J. Bourgain, *Global Solutions of Nonlinear Schrödinger Equations* (American Mathematical Society, Providence, 1999).

[14] P. G. Kevrekidis, D. J. Frantzeskakis, and R. Carretero-González, *Emergent Nonlinear Phenomena in Bose-Einstein Condensates: Theory and Experiment* (Springer, Heidelberg, 2008).

[15] P. G. Kevrekidis, D. J. Frantzeskakis, and R. Carretero-González, *The Defocusing Nonlinear Schrödinger Equation: from Dark Solitons and Vortices to Vortex Rings* (SIAM, Philadelphia, 2015).

[16] A. Hasegawa, *Solitons in Optical Communications* (Clarendon Press, Oxford, 1995).

[17] Yu. S. Kivshar and G. P. Agrawal, *Optical Solitons: from Fibers to Photonic Crystals* (Academic Press, San Diego, 2003).

[18] E. Infeld and G. Rowlands, *Nonlinear Waves, Solitons and Chaos* (Cambridge University Press, Cambridge, 1990).

[19] R. S. Johnson, *A Modern Introduction to the Mathematical Theory of Water Waves* (Cambridge University Press, Cambridge, 1997).

[20] C. Kharif, E. Pelinovsky, and A. Slunyaev, *Rogue Waves in the Ocean* (Springer, New York, 2009).

[21] E. Mjølhus, Phys. Scr. **40**, 227 (1989).

[22] E. Mjølhus, J. Plasma Phys. **16**, 321 (1976).

[23] M. S. Ruderman, J. Plasma Phys. **67**, 271 (2002).

[24] S. W. Xu, J. S. He, L. H. Wang, J. Phys. A: Math. Theor. **44**, 305203 (2011).

[25] Y. S. Zhang, L. J. Guo, S. W. Xu, Z. W. Wu, J. S. He, Comm. Nonlin. Sci. Numer. Simul. **19**, 1706 (2014).

[26] A. Arnaudon, J Nonlinear Sci. **26**, 1133 (2016).

[27] A. Arnaudon, J. Phys. A: Math. Theor. **49**, 125202 (2016).

[28] P. L. Dong, Z. W. Wu and J. S. He, Rom. J. Phys. **62**, 62 (2017).

[29] A. Jeffrey and T. Kawahara, *Asymptotic Methods in Nonlinear Wave Theory* (Pitman, Boston, 1982).

[30] V. E. Zakharov and E. A. Kuznetsov, Physica D **18**, 455 (1986).

[31] Yu. S. Kivshar and B. Luther-Davies, Phys. Rep. **298**, 81 (1998).

[32] D. J. Frantzeskakis, J. Phys. A: Math. Theor. **43**, 213001 (2010).

[33] Yu. S. Kivshar, Phys. Rev. A **42**, 1757 (1990).

[34] Yu. S. Kivshar, Opt. Lett. **16**, 892 (1991).

[35] Yu. S. Kivshar and V. V. Afanasjev, Phys. Rev. A **44**, R1446(R) (1991).

[36] Yu. S. Kivshar, D. Anderson and M. Lisak, Phys. Scr. **47**, 679 (1993).

[37] D. J. Frantzeskakis, J. Phys. A: Math. Gen. **29**, 3631 (1996).

[38] T. P. Horikis and D. J. Frantzeskakis, Opt. Lett. **41**, 583 (2016).

[39] T. P. Horikis and D. J. Frantzeskakis, J. Phys. A: Math. Theor. **49**, 205202 (2016).

[40] T. P. Horikis and D. J. Frantzeskakis, Phys. Rev. Lett. **118**, 243903 (2017).

[41] F. Dalfovo, S. Giorgini, L. P. Pitaveskii, S. Stringari, Rev. Mod. Phys. **71**, 463 (1999) .

[42] L. P. Pitaevskii and S. Stringari, *Bose-Einstein Condensation*, Oxford University Press (Oxford, 2003).

[43] C. J. Pethick and H. Smith, *Bose-Einstein condensation in dilute gases*, Cambridge University Press (Cambridge, 2002).

[44] M. J. Ablowitz and H. Segur, *Solitons and the Inverse Scattering Transform*, SIAM (Philadelphia, 1981).

[45] V. E. Zakharov, Collapse and Self-focusing of Langmuir Waves, Handbook of Plasma Physics, Elsevier (1984).

[46] V. E. Zakharov, Sov. Phys. JETP **35**, 908 (1972).

[47] T. B. Benjamin and J. E. Feir, J. Fluid Mech. **27**, 417 (1967).

[48] J. Yang, *Nonlinear Waves in Integrable and Nonintegrable Systems*, SIAM (Philadelphia, 2010).

[49] Y. Nesterov, Soviet Mathematics Doklady **27**, 367 (1983).

[50] W. Su, S. Boyd, E. J. Candes, Journal of Machine Learning Research **153**, 1 (2016).

[51] A. Wibisono, A. Wilson, M. Jordan, Proceedings of the National Academy of Sciences **133**, E7351 (2016).

[52] D. R. Solli, C. Ropers, P. Koonath, and B. Jalali, Nature **450**, 1054 (2007).

[53] B. Kibler *et al.*, Nature Phys. **6**, 790 (2010).

[54] B. Kibler *et al.*, Sci. Rep. **2**, 463 (2012).

[55] J. M. Dudley, F. Dias, M. Erkintalo, and G. Genty, Nat. Photon. **8**, 755 (2014).

[56] B. Frisquet *et al.*, Sci. Rep. **6**, 20785 (2016).

[57] C. Lecaplain, Ph. Grelu, J. M. Soto-Crespo, and N. Akhmediev, Phys. Rev. Lett. **108**, 233901 (2012)

[58] A. Chabchoub, N. P. Hoffmann, and N. Akhmediev, Phys. Rev. Lett. **106**, 204502 (2011).

[59] A. Chabchoub, N. Hoffmann, M. Onorato, and N. Akhmediev, Phys. Rev. X **2**, 011015 (2012).

[60] A. Chabchoub and M. Fink, Phys. Rev. Lett. **112**, 124101 (2014).

[61] H. Bailung, S. K. Sharma, and Y. Nakamura, Phys. Rev. Lett. **107**, 255005 (2011).

[62] A. N. Ganshin, V. B. Efimov, G. V. Kolmakov, L. P. Mezhov-Deglin, and P. V. E. McClintock, Phys. Rev. Lett. **101**, 065303 (2008).

[63] M. Shats, H. Punzmann, and H. Xia, Phys. Rev. Lett. **104**, 104503 (2010).

[64] E. Pelinovsky and C. Kharif (eds.), *Extreme Ocean Waves* (Springer, NY, 2008).

[65] C. Kharif, E. Pelinovsky, and A. Slunyaev, *Rogue Waves in the Ocean* (Springer, NY, 2009).

[66] A. R. Osborne, *Nonlinear Ocean Waves and the Inverse Scattering Transform* (Academic Press, Amsterdam, 2010).

[67] M. Onorato, S. Residori, and F. Baronio, *Rogue and Shock Waves in Nonlinear Dispersive Media*, Springer-Verlag (Heidelberg, 2016).

[68] Z. Yan, J. Phys. Conf. Ser. **400**, 012084 (2012).

[69] P. T. S. DeVore, D. R. Solli, D. Borlaug, C. Ropers, and B. Jalali, J. Opt. **15**, 0640031 (2013).

[70] M. Onorato, S. Residori, U. Bortolozzo, A. Montinad, and F. T. Arecchi, Phys. Rep. **528**, 47 (2013).

[71] S. Chen, F. Baronio, J. M. Soto-Crespo, P. Grelu and D. Mihalache, J. Phys. A Math. Theor. **50**, 463001 (2017).

[72] D. H. Peregrine, J. Austral. Math. Soc. B **25**, 16 (1983).

[73] E. A. Kuznetsov, Sov. Phys.-Dokl. **22**, 507 (1977).

[74] Ya. C. Ma, Stud. Appl. Math. **60**, 43 (1979).

[75] N. N. Akhmediev, V. M. Eleonskii, and N. E. Kulagin, Theor. Math. Phys. **72**, 809 (1987).

[76] K. B. Dysthe and K. Trulsen, Phys. Scr. **T82**, 48 (1999).

[77] A. Ankiewicz, N. Devine, N. Ahkmediev, Physics Letters A **373**, 3997 (2009).

[78] J. Garnier, and K. Kalimeris, J. Phys. A **45**, 035202 (2012).

[79] A. Calini and C. M. Schober, pp. 31–51 in Ref. [64].

[80] C. B. Ward and P. G. Kevrekidis, arXiv:1902.05494.

[81] N. Akhmediev, A. Ankiewicz, M. Taki, Phys. Lett. A **373**, 675 (2009).

[82] D. Mihalache and N. C. Panoiu, J. Phys. A: Math. Gen. **26**, 2679 (1993).

[83] D. Mihalache, F. Lederer, D. M. Baboiu, Phys. Rev. A **47**, 3285 (1993).

[84] D. J. Benney and J. C. Luke, J. Math. Phys. (N.Y.) **43**, 309 (1964).

[85] V. I. Karpman, *Non-linear Waves in Dispersive Media* (Pergamon Press, Oxford, 1975).

[86] M. Remoissenet, *Waves Called Solitons* (Springer, Berlin, 1999).

[87] D. E. Pelinovsky, Yu. A. Stepanyants, and Yu. S. Kivshar, Phys. Rev. E **51**, 5016 (1995).

[88] Yu. S. Kivshar and D. E. Pelinovsky, Phys. Rep. **331**, 117 (2000).

[89] S. Cox and P. Matthews, J. Comput. Phys. **176**, 430 (2002).

[90] A. Kassam and L. Trefethen, SIAM J. Sci. Comput. **26**, 1214 (2005).

[91] I. K. Mylonas, C. B. Ward, P. G. Kevrekidis, V. M Rothos, D. J. Frantzeskakis, Phys. Lett. A **381**, 3965 (2017).

[92] T. P. Horikis and D. J. Frantzeskakis, J. Phys. A: Math. Theor. **49**, 205202 (2016).

[93] T. P. Horikis and D. J. Frantzeskakis, Phys. Rev. Lett. **118**, 243903 (2017).

[94] H.E. Nistazakis, D. J. Frantzeskakis, and B. A. Malomed, Phys. Rev. E **64**, 026604 (2001).

[95] P. G. Drazin, *Solitons*, Cambridge University Press (Cambridge, 1983).

[96] J. Yang and T. I. Lakoba, Studies in Applied Mathematics **120**, 265 (2008).

[97] M. Ablowitz, Z. H. Musslimani, Optical Society of America **30**, 2140 (2005).

[98] J. T. Cole, Z. H. Musslimani, Physica D **358**, 15 (2017).

[99] B. O'Donoghue and E. J. Candes, Found. Comput. Math. **15**, 715 (2003).

[100] J. Yang and T. Lakoba, Stud. Appl. Math. **118**, 153 (2007).

[101] Y. S. Kivshar, T. J. Alexander, S. K. Turitsyn, Physics Letters A **278**, 225 (2001).

[102] G. L. Alfimov and D. A. Zezyulin, Nonlinearity **20** 2075 (2007).

[103] C. T. Kelley, *Solving Nonlinear Equation with Newton's Method* (SIAM, Philadelphia, 2003)

[104] E. G. Charalampidis, P. G. Kevrekidis, and P. E. Farrel, Comm. Nonlin. Sci. Num. Simul. **54**, 482 (2018).

[105] L. Landau and I. M. Lifshitz, *Quantum Mechanics* (Nauka, Moscow, 1989)

[106] E. G. Charalampidis, J. Cuevas-Maraver, D. J. Frantzeskakis, P. G. Kevrekidis, arXiv:1609.01798.

[107] J. Yang, Journal of Computational Physics **228**, 7007 (2009).

[108] K. J. Kedziora, A. Ankiewics, N. Akhmediev, Eur. Phys. J. Special Topics **223**, 43 (2014).

[109] D. G. Aronson, S. I. Betelu, I. G. Kevrekidis, arXiv:nlin/0111055.

[110] C. I. Siettos, I. G. Kevrekidis, P. G. Kevrekidis, Nonlinearity **16**, 497 (2003).

[111] P. G. Kevrekidis, C. I. Siettos, Y. G. Kevrekidis, Nature Comms. **8**, 1562 (2017).

[112] G. I. Barenblatt, *Scaling, self-similarity and intermediate asymptotics*, Cambridge University Press (Cambridge, 1996).

[113] Y. V. Sedletsky, J. Exp. Theor. Phys. **97**, 180 (2003).

[114] V. E. Zakharov, Solitons in Topics Curr. Phys., Vol. 17, R. K. Bullough and P. J. Caudrey (Eds.) Springer-Verlag (Berlin 1980).

[115] A. Ankiewicz, J. M. Soto-Crespo, and N. Akhmediev, Physical Review E **81**, 046602 (2010).

[116] Y. Ohta and J. K. Yang, Physical Review E **86**, 036604 (2012).

[117] J. Rao, L. Wang, W. Liu, and J. He, Theoretical and Mathematical Physics **193**, 1783 (2017)

[118] See, e.g., Y. Cher, G. Simpson, C. Sulem, SIAM J. Appl. Dyn. Sys. **16**, 514 (2017).

[119] M. Bertola and A. Tovbis, Comm. Pure Appl. Math. **66**, 678 (2013).

[120] A. Calini and C. M. Schober, Phys. Lett. A **298**, 335 (2002).

[121] C. B. Ward, P. G. Kevrekidis, N. Whitaker, arXiv:1712.03292.

[122] A. J. Bernoff and T. P. Witelski, Appl. Math. Lett. **15**, 599 (2002).

[123] A. J. Bernoff and T. P. Witelski, J. Eng. Math **66**, 11 (2010).

[124] S. Ray and R. C. Viesca, J. Geophys. Res.: Solid Earth **122**, 8214 (2017).

[125] J. Cuevas-Maraver, P. G. Kevrekidis, D. J. Frantzeskakis, N. I. Karachalios, M. Haragus, G. James Phys. Rev. E **96**, 012202 (2017)